

Transient Dipole-Interactions on Sub-Cycle Timescales

Lorenz Bruno Drescher

Berlin, 2019

im Fachbereich Physik der Freien Universität Berlin
eingereichte Dissertation
zur Erlangung des akademischen Grades
doctor rerum naturalium
(Dr. rer. nat.)

Erstgutachter: Prof. Dr. Marc Vrakking
Zweitgutachter: Prof. Dr. Thomas Pfeifer
Drittgutachter: Prof. Dr. Reinhard Dörner

Tag der Disputation: 30.04.2020

At the Doors of Babylon
You are my Zion
Pacing Tiger
The Keeper's Cage

An Invisible Light

Scissor Sisters



Abstract

Investigating the motion of electrons in atoms, molecules and solids on attosecond timescales is of widespread current research interest. In recent years, attosecond transient absorption spectroscopy (ATAS), has emerged as a versatile tool to study these dynamics. In ATAS the modification of absorption of an attosecond pulse in the extreme ultraviolet (XUV) wavelength region by a phase-locked infrared pulse (IR) is explored, revealing the dynamics of electronic coherences and light-induced couplings on attosecond timescales. To resolve the light-induced coupling of molecular valence and Rydberg states on the timescales of the cycle of the IR laser lightfield, an ATAS study on iodomethane is presented in the first part of this thesis. For the first time, ATAS is extended from atoms and homo-nuclear molecules to a polyatomic molecule, as well as to core-to-valence and core-to-Rydberg transitions in the XUV to soft X-ray spectral regimes that allow a site-specific insight into the molecular light-induced dynamics. The impact of symmetry on the observable coupling pathways in ATAS is unraveled and the possibility to obtain additional information from polar and chiral molecules in future experiments is discussed.

In the second part of this thesis, XUV refractive optics are developed using a dense gas jet. Refractive optics have so far been absent in the XUV region, due to a lack of materials with suitable properties. An XUV prism is introduced as the first demonstration of XUV refractive optics, based on the utilization of an inhomogeneous, dense gas jet. In a second application of XUV refractive optics, an XUV gas lens is constructed: A dense gas jet matching the XUV beam diameter is used to focus an XUV beam similar to the way conventional cylindrical lenses focus beams. Exploring the behavior of refractive indices in the XUV spectral domain a novel phase-matching concept is introduced that allows to efficiently modify and control the spectral bandwidth of an XUV source. The concept is experimentally demonstrated by means of XUV bandwidth compression in a krypton gas jet.

The results of the work reported in this thesis show how the complex transient dipole spectrum of atoms and molecules can be experimentally observed and theoretically understood from a transient absorption or refraction measurement and used to unravel dynamics on the attosecond timescale. The developed tools allow for a more versatile application of XUV spectroscopy in the future.

Kurzfassung

Die Bewegungen von Elektronen in Atomen, Molekülen und Festkörpern auf der Attosekundenzeitskala ist Gegenstand aktueller Forschung. In den vergangenen Jahren hat sich die Methode der *Attosecond Transient Absorption Spectroscopy* (ATAS) etabliert um diese Dynamiken zu ergründen. Dabei wird die Änderung der Absorption von Licht im extrem ultravioletten Spektralbereich (XUV) durch einen phasenkontrollierten Infrarotlaserpuls untersucht. Dieser erlaubt Rückschlüsse auf die Dynamiken von elektronischen Kohärenzen und lichtinduzierten Kopplungen mit Attosekundenauflösung. Im ersten Teil dieser Dissertation wird eine ATAS-Studie vorgestellt, in der die lichtinduzierte Kopplung von molekularer Valenz- und Rydbergzuständen auf der Zeitskala des Zyklus des IR-Feldes untersucht wurde. Zum ersten Mal wurde ATAS, das davor auf Atome und homonukleare Moleküle angewendet wurde, auf ein mehratomiges Molekül angewandt. Die Kern-zu-Valenz- und Kern-zu-Rydberg-Übergänge im XUV- und weichem Röntgenlichtbereich erlauben hierbei Einblick in die elementspezifische lichtinduzierte Dynamik. Die Rolle von Symmetrien auf die beobachtbaren Kopplungspfade in ATAS werden genauer betrachtet und die Möglichkeit in zukünftigen Experimenten erweiterte Informationen über polare und chirale Moleküle zu erhalten wird erörtert.

Im zweiten Teil werden Brechungsoptiken im XUV-Bereich mittels eines dichten Gasjets präsentiert. Solche Optiken waren im XUV-Bereich bisher nicht verfügbar, da keine geeigneten Materialien bekannt waren. Ein XUV-Prisma wird als eine erste Anwendung von Brechungsoptiken im XUV-Bereich vorgestellt, basierend auf einem inhomogenen Gasjet. Als zweite Anwendung wird eine XUV-Gaslinse präsentiert: Ein dichter Gasjet, von ähnlichem Ausmaß wie der XUV-Strahldurchmesser, wird benutzt um diesen XUV-Strahl zylindrisch zu fokussieren. Die weitere Studie des Verhaltens der Brechungsindizes im XUV-Bereich ermöglicht die effiziente Umwandlung und Kontrolle der spektralen Bandbreite einer XUV-Quelle durch ein neues Konzept der Phasenanpassung. Dieses Konzept wird experimentell durch XUV-Bandbreitenkompression in einem Krypton Gasjet demonstriert.

Die Ergebnisse der Studien, die in dieser Dissertation präsentiert werden, zeigen, wie das komplexwertige transiente Dipolspektrum von Atomen und Molekülen in transienter Absorptionsspektroskopie und Refraktometrie experimentell beobachtet und mittels der Theorie verstanden werden kann um Dynamiken auf der Attosekundenkala zu enthüllen. Die entwickelten Werkzeuge erlauben eine flexiblere Anwendung von XUV Spektroskopie in der Zukunft.

Contents

1	Introduction	1
2	Theoretical Description of the Time-Dependent Dipole	11
2.1	Numerical Solution of the Three-Level System	12
2.2	Features of Atom-like Attosecond Transient Absorption Spectroscopy	15
3	Experimental Setup	21
3.1	Overview	21
3.2	Upgrade to the Pulse-Compression-Scheme	25
4	State-Resolved Probing of Attosecond Timescale Molecular Dipoles	29
4.1	Experimental Observation	30
4.2	Numerical Simulation Using <i>Ab-Initio</i> Results	34
4.3	Analysis Using Singular Value Decomposition	37
4.4	Conclusion	42
5	Extreme-ultraviolet Refractive Optics	45
5.1	Gas Phase XUV Prism	46
5.2	XUV Refractive Lens	50
5.3	Conclusion and Outlook	56
6	XUV Spectral Compression by Four-Wave-Mixing	61
6.1	Four-Wave Mixing and Phase-Matching at Double-Resonances	62
6.2	Experimental Demonstration of Bandwidth Compression . . .	64
6.3	Perturbative Treatment of Third-Order Response	67
6.4	Coupled Time-Dependent Schrödinger and Maxwell Wave Equation Propagation	71
6.5	Conclusion	74
7	The Time-Dependent Dipole of Non-Centrosymmetric Molecules	77
7.1	Discussion of Non-Centrosymmetric Attosecond Transient Absorption Spectroscopy	78
7.2	Analytical Solution with Adiabatic Basis	79

Contents

7.3	Observability of Non-Centrosymmetric Features	88
8	Summary	95
A	Numerical Solution With Finite-Basis and Full Dimensionality	97
B	Spectral Solutions of the Adiabatic Approximation	99
B.1	Centrosymmetric Terms	100
B.2	Non-Centrosymmetric Terms	101
B.3	Delay-Dependent Interference with XUV-Field	102
C	Delay-Dependent Solution of the Light-Induced Phase	105
	List of Publications	109
	Bibliography	111
	Acknowledgments	127

1 Chapter 1

Introduction

The study of motion and dynamics is a connecting topic through many fields of modern science. Following the pre-Socratic idea *panta rhei*, everything flows, modern physics is concerned with motion and dynamics on vastly different scales: From the dynamics of space-time itself, the inexplicable rotational speed of galaxies, the complex interplay of the earth's climate system and human networks, down to the folding of proteins and efficient transport of elementary charges. It is in these small quantum systems where we encounter the shortest timescales: While human perception takes place on the low millisecond scale and the clocking speed of electronics reaches its limits on the high picosecond scale ($1 \text{ ps} = 10^{-12} \text{ s}$), the movement of atoms in molecules, i.e. chemical reactions, can occur on timescales as fast as a few femtoseconds ($1 \text{ fs} = 10^{-15} \text{ s}$) and the motion of electrons occurs on the attosecond timescale ($1 \text{ as} = 10^{-18} \text{ s}$).

Many of these *ultrafast* processes influence our everyday live. Prominently among them, photosynthesis [1] and vision [2] are biomolecular processes that are thought to crucially depend on an ultrafast reaction to the external stimulus of visible light. The quest to temporally resolve the steps involved in such a photochemical reaction seemed to remain a purely theoretical effort less than a century ago, limited by the reaction speed of mechanical and electronic devices needed to record these dynamics. However, the development of short, pulsed laser sources has rapidly expanded the timescales that can be experimentally resolved by using these short laser pulses as strobe lights in *pump-probe* experiments. In this type of experiment, one laser pulse is used to start (*pump*) a dynamic at a defined time by exciting a coherent superposition of states (i.e. a wavepacket) and a second laser pulse is used to sample (*probe*) the evolution of the dynamic after a given delayed time. In the 1980s, development of femtosecond laser pulses allowed to temporally resolve the intermediate steps of molecular motion and photochemical reactions, which led to the creation of the field of femtochemistry [3]. At the end of the 20th century, the further development of intense, ultrashort laser pulses opened the door to study strong-field effects in atoms and molecules, i.e. effects arising from the interaction with a laser field that is comparable in strength to the atomic binding potential. These advances led to the discovery of high harmonic generation (HHG), which made the attosecond timescale experimentally accessible.

1 Introduction

In HHG, the oscillating intense electric field of a short laser pulse (in the infrared to UV spectral region) can tunnel-ionize atoms near the time in the cycle of the maximum electric field, accelerate the freed electrons and drive them back to recollide with their parent ion after the direction of the electric field has reversed. The recombination of the electrons with their parent ions leads to the emission of light. The wavelength of the emitted light, which typically lies in the extreme ultra-violet (XUV) to soft X-ray region, thereby depends on the ionization potential of the atom and the kinetic energy of the returning photoelectron, which can be described by a semi-classical trajectory. This simplified description of the HHG process called *three step model*, introduced by Kulander and Schafer [4], as well as Corkum [5] and Lewenstein [6], can cover many observed phenomena of HHG well¹. While the process is repeated every half-cycle of the driving field, the time between ionization and recombination is well-defined by the trajectories. In 2001, it could be experimentally proven by Paul *et al.* [8] that HHG leads to a train of coherent light pulses on the attosecond timescale. In spectral representation such an attosecond pulse train (APT) corresponds to an evenly spaced comb of emission peaks at the harmonics of the driving field². Compression of the driving pulse close to the single-cycle limit or a sub-cycle modulation of the driving pulse can limit the HHG-process to only a single half-cycle of the driving field, which leads to the generation of an isolated attosecond pulse (IAP) with a continuous spectrum. This was first demonstrated within the same year by Hentschel *et al.* [9]. Using attosecond pulses in combination with a time-delayed near-infrared (NIR) field, M. Drescher *et al.* [10] could then measure the few femtosecond decay time of Auger states of krypton in real-time. These experimental breakthroughs [11] have been lauded as “the beginning of the age of atto[second]physics” [12].

What scientific questions do we seek to answer on these ultrafast timescales? A. Zewail, who was awarded the Nobel prize in Chemistry in 1999 for his efforts in the field of femtochemistry, quotes in his Nobel lecture [3] J. Baggott for formulating three question that capture what “[...] the entire history of chemical reaction dynamics and kinetics has been about” [13]:

How does the energy put into a reactant molecule redistribute among the different degrees of freedom, and how fast does this happen?
What are the speeds of the chemical changes connecting individual quantum states in the reactants and products? What are the

¹A further introduction into HHG for attosecond physics can be found in Ref. [7].

²In the case of a centrosymmetric medium (e.g. atoms), because of inversion symmetry only the odd harmonics of the driving field are emitted.

detailed nuclear motions that chart the reaction through its transition states, and how rapid are these motions?

While these questions of femtochemistry can be associated with the (semi-classical) characteristic timescale of the movement of nuclei (~ 100 fs [3]), we can associate attosecond physics with the (semi-classical) characteristic timescale of the movement of the electron by expressing the time an electron would take to complete one revolution around the Bohr radius (152 as) [7 Eq. 1.13 (p.11)], i.e. the radius of the smallest electron orbit in hydrogen atoms. The focus of attosecond physics is therefore to study the dynamic properties of the electronic degrees of freedom in atoms, molecules, clusters and nanoparticles as well as solids. As such, we might try to also formulate three key questions of molecular attosecond physics as they pertain to the electronic dynamics of molecules on the attosecond timescale.

For a first question, we can natively translate from Baggott and the domain of nuclear motion to the electronic degrees of freedom: **How is the energy put in a molecule redistributed among the electronic degrees of freedom and how fast does this happen?** Radiationless energy redistribution processes, such as intermolecular vibrational redistribution, have been shown to play an important role in many photochemical processes [3]. The increased temporal resolution of attosecond pulses can be used to follow these processes in greater detail than before, allowing for example to follow the redistribution of population early during a photoinduced fragmentation process [14] or through an conical intersection [15]. In these processes, the population of excited states is redistributed because the electronic degrees of freedom couple to the nuclear degrees of freedom [16]. This offers to ask a second question. When we study the nature of the pathways connecting “reactants and products” of a photochemical reaction, we want to know if also a purely electronic dynamic can determine the outcome of such a reaction and if it can be controlled: **What is the role of the electronic excitation for a photochemical process?** For example, it was shown, by Sansone and co-workers [17], that the outcome of a photodissociation reaction of H_2^+ , initiated by an attosecond pulse, can be controlled by an electronic excitation by a time-delayed NIR pulse, by observing a delay-dependent localization of the positive charge on the dissociated fragments. Theoretical calculations have predicted, that a purely electronic dynamic of an excited wavepacket can lead to a transport of charge (charge migration) that is faster than a process involving nuclear motion would be. This has sparked interest and opened speculation whether such a fast and therefore efficient process could be involved in the mentioned biomolecular light-driven processes. However, whether these processes can have any considerable effect on chemical reactions [16] and if they

1 Introduction

can exist for longer timescales or quickly dephase due to nuclear-motion [18, 19] remain open and debated research questions.

Third, if we are to study the “detailed electronic motion”, to adapt Baggott’s third question to the attosecond domain, quantum theory requires us to study the expectation value of the position of charge in the molecules over time. This is the time-dependent dipole. Attosecond time-resolution enables us to not only follow this “electronic motion” as the molecules follows the photoexcitation, but intriguingly allows to study the reaction of the molecule to the photoexcitation itself at a time-scale below the cycle of the optical field (sub-cycle). We will therefore ask: **What is the dynamic of the time-dependent dipole following the photoexcitation?** In this thesis, the focus will be to advance the understanding of the time-dependent dipole following photoexcitation, as a basis to aid addressing the first and second question in the future. More specifically, we will study, how the interaction of attosecond pulses from HHG with molecules leads to modifications of these pulses and how information about the electronic dynamics in the molecules can be inferred from it.

Ideally, attosecond *pump-probe* experiments would be designed to include two attosecond pulses to resolve dynamics on the attosecond timescale. However, the limited available flux of attosecond pulse sources (due to the very low efficiency of HHG) makes the observation of a two attosecond pulse interaction unlikely and the realization of such an experiment remains difficult. Hence, attosecond experiments using HHG pulses are often carried out combining the attosecond pulse from HHG with a time-delayed copy of the driving pulse, where the dependence of an observable on the sub-cycle structure of the field can be used to reconstruct the dynamics on attosecond timescales. One of the techniques to reconstruct the attosecond timescale dynamics from such sub-cycle dependent experiments is called attosecond transient absorption spectroscopy (ATAS). It will be the focus of the first part of this thesis.

In ATAS, the absorption of a spectrally broad XUV pulse of attosecond duration in atoms, molecules or solids is modified by a time-delayed laser pulse (most commonly in the NIR spectral region) and the evolution of the excited states is inferred from the observed signal. This might appear as a non-causal configuration as the “absorbed” XUV pulse arrives before the modifying NIR pulse, but the causality becomes clear if we examine a classical description of the interaction of matter with an electromagnetic wave: As an electromagnetic wave passes through a material, charged particles are accelerated by the changing electric field and are displaced from their equilibrium position which induces an oscillation. As the polarized medium continues to oscillate after the interaction with the light, it itself generates an electromagnetic wave: the induced oscillating dipole [20–24]. The characteristic response of the induced

dipole given by the specific environment of the system under study, be it free or bound, localized or collective, its topology and symmetry, uncovers a plethora of information that is the basis for optical spectroscopy methods. Often this information is obtained from the frequency response of a material, which in the linear response limit is described by the complex refractive index. Resonant phenomena in the excitation lead to characteristic frequency-dependent shapes in the phase of the induced dipole, leading e.g. to extinction of light in the interference between the transmitted light and the induced dipole at a detector, i.e. absorption.

It is this induced oscillating dipole which can be modified in ATAS by the time-delayed NIR pulse during the induction decay³. The modification thereby gives rise to energy- and delay-dependent characteristic spectroscopic features that allow to reconstruct the time-dependent dipole. We will explore the theoretical description of the interaction of the induced dipole oscillation with the XUV field in more detail in Chapter 2, where we will also introduce a quantum mechanical description of the time-dependent dipole in a two-color field (i.e. XUV and NIR) and discuss the characteristic features of ATAS. We will also present an experimental apparatus to perform ATAS using broad XUV pulses of attosecond duration from HHG in Chapter 3.

To date, ATAS has been applied to atoms and homo-nuclear molecules. For example, the effect of the excitation of laser-dressed atoms⁴ and their dependence on the sub-cycle NIR electric field on the XUV absorbance has been studied [25–27]. Chini *et al.* [28] have investigated, how the absorption by resonances in atoms is affected by an energy shift due to the oscillating NIR field (AC Stark effect). Ott and co-workers [29] have used this energy shift to formulate a light-induced phase to manipulate the shape of absorption resonances. The understanding of the behavior of ATAS signals has led to the reconstruction of the evolution of electronic wavepackets and the motion of electrons in neutral atoms [30] and ions [31]. ATAS has furthermore been used to trace the dynamic of a purely electronic dynamic in atoms in the form of autoionization resonances. Kaldun *et al.* [32] have studied the time-dependent formation of a Fano-resonance, which forms due to two interfering photoionization pathways,

³This also explains why XUV absorption spectroscopy allows high temporal and spectral resolution without violating an uncertainty relation: Since the absorbance signal is measured over long time after the interaction with a short XUV pulse and spectrally dispersed, the energy resolution is only limited by the spectrometer and the natural linewidths of the excited states, while the temporal resolution is limited by the pulse duration

⁴These are excitations into virtual states of the atom that are possible due to the interaction of the atom with the laser field. The NIR laser field “dresses” the atom to have excited states that involve the absorption or emission of multiple NIR photons.

1 Introduction

one being a direct photoionization and the other being an excitation of a highly excited neutral state that subsequently decays by ejection of an electron. By purposely dephasing the induced dipole oscillation with a strong time-delayed NIR pulse they could show that the characteristic Fano absorption lineshape forms only after sufficiently long time has passed, so that the neutral state has decayed. In homo-nuclear molecules, autoionization resonances have also been studied [33], as well as electronic and vibronic light-induced couplings [34, 35]. However, to take further steps to answer the questions that we have proposed, ATAS needs to be extended towards more complex, polyatomic molecules.

One challenge that arises in the transition of spectroscopy from being applied to atoms to being applied to molecules is the increased density of states in the molecular valence, which can make interpretation of experimental data difficult. Furthermore, the delocalization of the electron orbitals over multiple bonded atoms often found in molecules can make it difficult to discern the exact pathways of a molecular dynamic. This problem can for example be seen in recent studies of charge migration [36, 37], which require heavy theoretical calculations to assign an observed dynamic to its physical origin.

An interesting opportunity to address these problems is given by the high photon energy of attosecond pulses generated by HHG. Approaching high XUV to soft X-ray frequencies, these pulses allow to excite bound-to-bound transitions involving core-level electrons. These core-level electrons are highly localized at their parent atom in the initial state, but can be in a delocalized valence orbit in the final-state (core-to-valence transition), where they are sensitive to the molecular valence dynamic. The resonant energy of these transitions is specific to the element the electron is initially localized to, giving a spectroscopic local view into the molecular dynamic.

Core-level transient absorption spectroscopy using attosecond pulses from HHG has been successfully applied to study the population dynamics in photochemical molecular processes (a recent review is given in Ref. [38]). In a previous work, we could for example show that the delayed appearance of an XUV absorption signal in the UV-induced photodissociation of iodobenzene can be attributed to the excitation of an (pre-dissociated) intermediate state that has low localization on the iodine atom [39, 40].

To extend ATAS to polyatomic molecules in combination with core-level spectroscopy, we will present an experimental ATAS study of a prototypical polyatomic molecule, iodomethane (CH_3I), in Chapter 4. ATAS in the region of iodine 4d excitations is presented, a spectral region, where core-to-valence and core-to-Rydberg transitions co-exist. The work demonstrates, how the strength of the dipole-couplings between excited states can be revealed by ATAS, using as an example the substantially different response of valence and Rydberg states

(due to their state-specific polarizability). The presented study is the first example of an electronic attosecond dynamic in a polyatomic molecule that has been observed with the site-specificity of a core-to-valence transition. We furthermore introduce Singular value decomposition (SVD) as a method to advance the analysis of ATAS, by decomposing the temporal- and spectral-components of the dominant spectral features.

As will be shown in Chapter 2, the absorption signal arises from the interaction of the attosecond pulse with the imaginary part of the complex-valued dipole spectrum, which leads to extinction of light. The interaction with the real part represents a phase-shift in the propagation of the pulse and describes refraction. Refraction is the focus of the second part of this thesis.

Refraction of light is omnipresent in nature, where it forms the basis for the functionality of the human eye and the observation of a rainbow. Many technical devices rely on refraction in the visible, infrared and ultraviolet spectral regions. For example, eyeglasses and contact lenses are used to correct refractive errors in the eye. Certain scientific breakthroughs can be associated with the invention or improvement of refractive optical elements, such as Galileo's telescope, Newton's prism or van Leeuwenhoek's microscope. In the context of laser physics, refractive lenses are extensively used to focus or (de-)magnify laser beams. Dispersion and deflection of light by optical prisms is often used to compress or stretch ultrashort laser pulses. However, in the XUV to soft X-ray range, refractive elements have so far been missing, due to the (typically) large absorption and low refractive index of radiation by materials typically used for optics (e.g. glasses). Therefore optical elements in the XUV region so far have relied on reflective or diffractive elements to e.g. focus XUV beams.

A novel method is introduced in Chapter 5 that enables the use of refractive optics in the XUV spectral region. A gas-phase prism, where interaction of XUV light with an inhomogeneous, dense gas jet leads to the deflection of XUV light proportional to the refractive index, is demonstrated as a first realization of refractive optics for XUV radiation. A second application of the gas jet XUV refractive optics principle is demonstrated with a gas-phase lens for the XUV region. The gas-phase prism also enables to measure the XUV refractive index, intriguingly in a simultaneous measurement of both transient absorption and transient refraction, which allows to reconstruct the complex dipole spectrum and therefore the time-dependent dipole.

Since the duration of laser pulses is linked to their spectral width through the Fourier transformation, attosecond physics relies on spectrally broad XUV pulses. However, many other applications of XUV radiation have different

1 Introduction

requirements on the XUV bandwidth. As an example, a high-intensity spectrally narrow XUV pulse would be advantageous for coherent diffractive imaging (CDI) experiments studying the structure of solid targets [41], as the increased spatial resolution would make it possible to resolve smaller structures. On the opposing side, an ultrashort pulse duration and therefore broad bandwidth XUV pulse is important for CDI experiments studying the structure of isolated biomolecules and nanotargets in a single laser shot before destruction takes place [42]. XUV sources, however, often have characteristic spectral bandwidths. For example, narrow bandwidths are obtained from soft X-ray lasers [43] and seeded free-electron lasers (FEL) [44], and broad bandwidths are obtained as in the discussed case of HHG driven by few-cycle laser pulses [11]. These characteristic properties of a given XUV source can impose limitations to applications that make use of the XUV radiation [45], and flexibility in changing the bandwidth would be desirable.

Non-linear optical effects are often employed in the NIR to ultraviolet regions to compress or broaden laser bandwidths (see e.g. Chapter 3). However, so far these techniques have not been translated to the XUV region. A concept for bandwidth control of XUV radiation is introduced in Chapter 6 based on four wave mixing (FWM) of XUV pulses in the presence of NIR pulses. Efficient compression of broadband XUV radiation into a narrow bandwidth is thereby achieved by exploiting the steep gradient of the frequency-dependent refractive index between two closely spaced resonances, while the nearly flat dispersion in an incident spectral region allows for a broadband phase-matching. This concept is demonstrated experimentally using Kr gas as a medium, where a stark increase of spectral intensity is observed in a narrow region between the Kr ($^2P_{3/2}$)4d and ($^2P_{3/2}$)6s resonances after interaction of broad XUV and NIR pulses with a dense gas jet. While bandwidth narrowing will be demonstrated here, the reversal of the process could allow a spectral broadening and a pulse compression. These novel tools, together with gas-phase prism and lenses, might allow to improve experimental conditions for attosecond physics in future experiments.

As will be shown in Chapter 2 and Chapter 4, ATAS allows to gain information about the light-induced coupling, i.e. the transition dipole moment and the (NIR) electric field. However, due to symmetry reasons, only the square of the transition dipole matrix elements contributes to the observable signals in ATAS of centrosymmetric systems. Since parity is conserved in centrosymmetric systems, both the XUV and NIR pulse can only couple states of different parities. Therefore, as we will describe it in Chapter 2, the NIR pulse can only induce coupling between states that are accessible via a dipole transition from

the ground state (“bright state”) and states that are not (“dark states”). While parity conservation is an important guiding principle for recognizing the transitions that can occur in atoms, this is no longer the case in systems where the parity cannot be defined, i.e. systems that lack centrosymmetry, such as polar or chiral molecules. These systems will be the focus in the last part of this thesis.

In these systems, two states can be coupled by both an odd or an even number of photons. In other words, excitation pathways in which the XUV pulse can coherently excite two states that can then be coupled via one or more NIR photons need to be considered. The effect of these pathways in non-centrosymmetric systems will be discussed in Chapter 7. To further understand the origin of these signals, in Section 7.2 we will develop an analytical solution of the three-state model based on an adiabatic basis that separates the fast dynamics of the excitation by the XUV pulse from the slower dynamics of the NIR induced coupling. The appearance of the characteristic features can then be understood in terms of an adiabatic mixing of states by the NIR pulse at different times. We will see that the coherent excitation of two states that can be coupled via one photon lead to a new spectroscopic signal that depends linearly on the transition dipole moment and the coupling electric field. This dependence of the novel pathways of non-centrosymmetric systems gives the opportunity to obtain information in ATAS on parameters that are not available in centrosymmetric systems such as (degree of) orientation, the reconstruction of the NIR pulse and the linear transition dipole moment.

Chapter 2

2 Theoretical Description of the Time-Dependent Dipole

To gain a good understanding on how the interaction of an XUV and IR two-color field with the sampled media leads to the observed attosecond transient absorption spectra and how they reflect the dynamics of the medium, in this chapter we will discuss the physical origin of the signal in terms of the time-dependent dipole.

To begin, let us review the propagation of an electric field through the medium. As described in Chapter 1, the electric field $\boldsymbol{\epsilon}(t)$ induces a polarization response $\mathbf{P}(t)$ in the medium, which we will describe by the time-dependent dipole $\mathbf{d}(t)$:

$$\mathbf{P}(t) = \rho \mathbf{d}(t), \quad (2.1)$$

where ρ is the density of the medium. The propagation of the electric field, i.e. the changes to the field as it traverses the medium, can be described fully by the Maxwell wave equation (MWE). We will use a simpler form of the MWE in the spectral domain using the slowly evolving wave approximation [46] and a frame moving with the speed of light along the direction z [47]:

$$\nabla_{\perp}^2 \boldsymbol{\epsilon}(\omega) + \frac{2i\omega}{c} \frac{\partial \boldsymbol{\epsilon}(\omega)}{\partial z} = -\frac{\omega^2}{\epsilon_0 c^2} \mathbf{P}(\omega). \quad (2.2)$$

which can be further approximated for the expected low influence of beam transversal effects ($\nabla_{\perp}^2 \boldsymbol{\epsilon}(\omega) \ll 1$) as a plane-wave propagation:

$$i \frac{\partial \boldsymbol{\epsilon}(\omega)}{\partial z} = -\frac{\omega}{2\epsilon_0 c} \rho \mathbf{d}(\omega). \quad (2.3)$$

As can be seen, the electric field is modified by the spectral dipole as it propagates through the medium. However, let us assume for now that these changes

This chapter is in parts based on an article currently in preparation. The author of this thesis performed the numerical calculations, wrote the first draft and coordinated communication. Thanks to M. Vrakking and J. Mikosch for contributing to the manuscript.

2 Theoretical Description of the Time-Dependent Dipole

are small, such that $\frac{d(\omega)}{\epsilon(\omega)}$ is approximately constant over the length of the interaction L . Then Eq. 2.3 can be expanded:

$$i \frac{\partial \epsilon(\omega)}{\partial z} = -\frac{\omega}{2\epsilon_0 c} \rho \frac{d(\omega)}{\epsilon(\omega)} \epsilon(\omega) \quad (2.4)$$

and directly integrated, leading to:

$$\begin{aligned} \epsilon(\omega, z = L) &= \epsilon(\omega, z = 0) \exp \left[\frac{i\omega\rho}{2\epsilon_0 c} \frac{d(\omega)}{\epsilon(\omega)} L \right] \\ &= \epsilon(\omega, z = 0) e^{-\alpha(\omega)L} e^{i\Delta n(\omega)\frac{\omega}{c}L}. \end{aligned} \quad (2.5)$$

As expressed, the effect of the spectral dipole $d(\omega)$ to the electric field can be separated in two parts: $\alpha(\omega) = -\frac{\omega\rho}{2\epsilon_0 c} \text{Im} \frac{d(\omega)}{\epsilon(\omega)}$ describes a spectral attenuation of the field and is the absorption coefficient, while $\Delta n(\omega) = n(\omega) - 1 = \frac{\rho}{2\epsilon_0} \text{Re} \left(\frac{d(\omega)}{\epsilon(\omega)} \right)$ describes a spectral phase and is the change of refractive index.

This approximation and integration can be made if the medium is *optically thin* and is called the Beer-Lambert law. It allows to make the connection to the experimentally observable signal by taking the absolute square of Eq. 2.5, and comparing the spectral intensity of the electric field before and after interaction as the absorbance $A(\omega)$:

$$A(\omega) = \log \frac{|\epsilon_L(\omega)|^2}{|\epsilon_0(\omega)|^2} = \frac{\rho\omega L}{\epsilon_0 c} \text{Im} \frac{d(\omega)}{\epsilon(\omega)}. \quad (2.6)$$

Evidently, the observable signal in ATAS depends on the (spectral form of the) time-dependent dipole. Hence, in the first part of this chapter, we will discuss how the time-dependent dipole can be calculated for a semi-classical atom-like three-level system using the time-dependent Schrödinger equation (TDSE) in the interaction picture. This simple, one-dimensional model allows to discuss and specify characteristic features of ATAS, as they are found throughout literature.

2.1 Numerical Solution of the Three-Level System

The three-level system we want to consider is described by the Hamiltonian [48]:

$$\hat{H} = \begin{bmatrix} E_0 & d_{01}\epsilon_{XUV}(t) & d_{02}\epsilon_{XUV}(t) \\ d_{01}\epsilon_{XUV}(t) & E_1 & d_{12}\epsilon_{IR}(t) \\ d_{02}\epsilon_{XUV}(t) & d_{12}\epsilon_{IR}(t) & E_2 \end{bmatrix}, \quad (2.7)$$

2.1 Numerical Solution of the Three-Level System

where E_n are the field-free energies of the three levels, namely one ground-state level and two excited state levels, d_{nm} the transition dipole moments between the levels and $\varepsilon_{XUV}(t)$, $\varepsilon_{IR}(t)$ the time- and delay-dependent XUV and IR electric field¹. The atomic unit system is used throughout this chapter, i.e. $\hbar = m_e = q_e = 1$. For centrosymmetric systems, symmetry arguments require, that one of the transition dipole moments must be zero ($d_{01}d_{02}d_{12} = 0$), a rule which is often referred to as the Laporte rule [49]: Since parity is conserved in centrosymmetric systems, such as free atoms, the excitation of a particular excited state by both an even number of photons (e.g. the combination of an XUV photon and an IR photon) and an odd number of photons (e.g. an XUV photon only) is not possible. The differentiation is often made between states that are coupled to the ground state via a dipole transition (*bright states*) and those that have no dipole-allowed transition from the ground state, so called *dark states*.

We solve the time-dependent Schrödinger equation (TDSE) within the three-level basis set:

$$i\frac{\partial}{\partial t}|\Psi(t)\rangle = \hat{H}|\Psi(t)\rangle = \sum_{n=0}^2 c_n(t)e^{-iE_n t}|\Phi_n\rangle. \quad (2.8)$$

Note that the presence of the phase-term $e^{-iE_n t}$ in this equation implies that $c_n(t)$ describes a slow variation of the amplitude of a given state due to coupling to other states. In the absence of such couplings, $c_n(t)$ is a constant. To obtain the state-dependent amplitudes $c_n(t)$, we numerically solve the system of ordinary differential equations obtained from the TDSE:

$$i\frac{\partial}{\partial t} \begin{pmatrix} c_0 \\ c_1 \\ c_2 \end{pmatrix} = \begin{bmatrix} 0 & d_{01}\varepsilon_{XUV}(t)e^{-iE_1 t} & d_{02}\varepsilon_{XUV}(t)e^{-iE_2 t} \\ d_{10}\varepsilon_{XUV}(t)e^{iE_1 t} & 0 & d_{12}\varepsilon_{IR}(t)e^{i(E_1-E_2)t} \\ d_{20}\varepsilon_{XUV}(t)e^{iE_2 t} & d_{21}\varepsilon_{IR}(t)e^{i(E_2-E_1)t} & 0 \end{bmatrix} \begin{pmatrix} c_0 \\ c_1 \\ c_2 \end{pmatrix}, \quad (2.9)$$

for a given XUV-IR time-delay by forward integrating in time using a Runge-Kutta-Dormand-Prince method of 5th order with adaptive step-size control. Note that $d_{nm} = d_{mn}^*$. We will assume a real-valued transition dipole moment for the rest of the discussion.

Knowing the full time-evolution of the system, the time-dependent dipole moment can be calculated:

$$d(t) = \langle \Psi(t)|d|\Psi(t)\rangle = \sum_{n,m} c_n^*(t)c_m(t)d_{nm}e^{i(E_n-E_m)t} \quad (2.10)$$

¹Note that we have written the transition dipole moments and electric fields as scalar quantities, which is a valid approximation for atoms and co-polarized electric fields. An extension of this model to the three-dimensional representation of the transition dipole moments and electric fields can be found in Appendix A

2 Theoretical Description of the Time-Dependent Dipole

The spectral representation of the time-dependent dipole can be calculated by the Fourier transform [50]:

$$d(\omega) = \frac{1}{2\pi} \int_{-\infty}^{\infty} d(t)e^{i\omega t} dt = \mathcal{F}[d(t)](\omega). \quad (2.11)$$

Noting that $d(t)$ is a real quantity, the spectral representation through the Fourier transformation is Hermitian, i.e. $d(-\omega) = d^*(\omega)$, meaning that the full spectral information is contained at either positive or negative frequencies. The spectral response, i.e. the absorption or emission probability per unit frequency of a single atom or molecule, is obtained after Fourier transformation of the temporal evolution of the dipole moment and the electric field as the imaginary part of their product [23]:

$$S(\omega, \tau) = \text{Im} \left[\frac{d(\omega)}{\varepsilon_{XUV}(\omega)} \right], \omega > 0. \quad (2.12)$$

This spectral response is related to the macroscopic observable absorbance, as described in Eq. 2.6. As the static XUV absorption is not of interest in the context presented here, the change of absorbance $\Delta A(\omega, \tau)$ is used, i.e. the difference between the delay-dependent two-color absorbance and the static XUV-only absorbance. A positive value at a given frequency and delay thereby indicates an increased absorption due to the IR field, while a negative value indicates a decreased absorption or emission.

For the discussion here, we choose the parameters for our system similar to the He 2p ($E_1 = 21.22$ eV) and 2s ($E_2 = 20.62$ eV) excited states (conventionally, $E_0 = 0$), as ATAS is often applied to this system in the literature [23, 26, 28, 47, 51, 52]. As such, the coupling between the excited states $d_{12} = 2.75$ a.u. and the coupling matrix element $d_{01} = 0.33$ a.u.[53]. Being a centrosymmetric system, d_{02} is zero in Helium. To account for the finite resolution of the spectrometer and the decay of the excited states an imaginary term is added to the excited states energies. For the qualitative discussion of the characteristic features, we have set this imaginary term corresponding to a lifetime of 20 fs. This lifetime is much shorter than what would be expected for the He excited states under typical experimental conditions, it however allows to sufficiently cover all characteristic features in a single plot and emphasize the delay-dependent sub-cycle behavior of our model system [23]. The laser pulses used can be described as Gaussian envelope pulses:

$$\varepsilon(t, \tau) = \sqrt{I_0} e^{-\frac{t-\tau}{T}} \cos[\omega(t - \tau) - \phi], \quad (2.13)$$

where $T = \text{FWHM}/2 \sqrt{\ln 2}$ defines the temporal width of the pulse envelope by the full-width at half-maximum (FWHM), I_0 is the pulse intensity, ω the central

2.2 Features of Atom-like Attosecond Transient Absorption Spectroscopy

Table 2.1: Laser Parameters for Numerical Simulation

Parameter	IR-Pulse	XUV-Pulse
Central Frequency	1.55 eV	20.0 eV
Pulse Duration (FWHM)	7.0 fs	40 as
Peak Field Intensity	10^{12} W/cm ²	10^9 W/cm ²

frequency and τ the time-delay. Here, the IR pulse is centered at $t = 0$ and the delay of the XUV pulse is moved in time. The parameters for the two pulses are listed in Table 2.1. The density was set to $\rho = 10^{16}$ cm⁻³ and the interaction length $l = 0.3$ cm, similar to the experimental conditions in Chapter 4. The carrier-to-envelope phase ϕ was zero unless stated otherwise. The IR intensity has been chosen such that the ATAS signal can be observed with a sufficiently strong probability, but strong-field ionization does not need to be considered. The XUV intensity on the other hand is chosen to be within a linear regime, but has been chosen to be stronger than in a typical ATAS experiment to aid the stability of the numerical solution.

2.2 Features of Atom-like Attosecond Transient Absorption Spectroscopy

In Fig. 2.1 $\Delta A(\omega, \tau)$ calculated as described in the previous section is shown. Centered at 21.22 eV a perturbation of the induction decay (PID) is observed, manifested by absorption and emission features that are hyperbolically converging towards the resonant energy at large negative times. During overlap of the XUV and IR field, a sub-cycle dependent modification of the line-shape is observed. These effects can be described by the light-induced phase (LIP). To explain this, we will look at a modeled expression of the spectral lineshape. We will derive this expression from quantum mechanics later in Chapter 7.2. For now, let us assume that the time-dependent state-coefficient c_1 in Eq. 2.10 in the absence of an IR field follows a step-like excitation by the XUV pulse and a subsequent exponential decay. We will write this as:

$$c_1(t, \tau = 0) \propto |d_{01}|^2 \vartheta(t) e^{-\frac{\Gamma}{2}t}, \quad (2.14)$$

where we have approximated the XUV excitation at $t = 0$ with the Heaviside function $\vartheta(t)$ and Γ is the discussed lifetime width of the excitation. Inserting into Eq. 2.10, approximating the ground-state population as constant ($c_0 = 1$)

2 Theoretical Description of the Time-Dependent Dipole

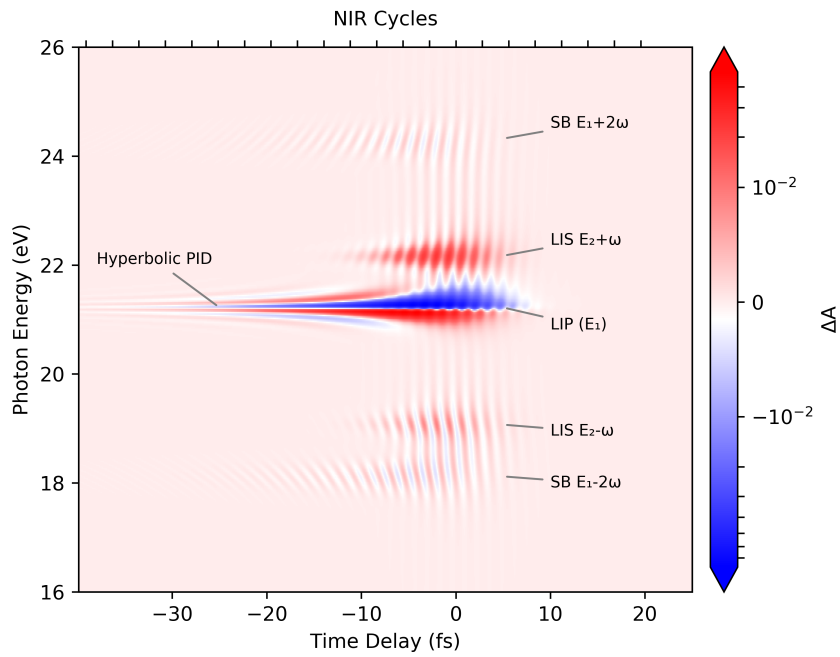


Figure 2.1: Attosecond Transient Absorption Spectrogram of the Centrosymmetric Problem calculated using a numerical solution of the Helium-like three-level TDSE. The spectral features are oscillating at even-multiples of the IR field periodicity. Positive time delays indicate an arrival of the IR pulse before the XUV pulse.

2.2 Features of Atom-like Attosecond Transient Absorption Spectroscopy

and transforming to the spectral-domain, the spectral dipole can be written as:

$$d(\omega) \propto \int_{-\infty}^{\infty} \left(|d_{01}|^2 \vartheta(t) e^{-\frac{\Gamma}{2}t} e^{iE_1 t} + \text{c.c.} \right) e^{i\omega t} dt. \quad (2.15)$$

The solution to the Fourier integral is the Breit-Wigner distribution [50]:

$$\begin{aligned} d(\omega) &\propto \frac{|d_{01}|^2}{\frac{\Gamma}{2} + i(\omega - E_1)} + \text{c.c.} \\ &= |d_{01}|^2 \left(\frac{\frac{\Gamma}{2}}{\frac{\Gamma^2}{4} + (\omega - E_1)^2} + \frac{i(\omega - E_1)}{\frac{\Gamma^2}{4} + (\omega - E_1)^2} \right), \omega > 0. \end{aligned} \quad (2.16)$$

We see: The spectral dipole is composed of a Fano-like (dispersive) and Lorentzian (symmetric) distribution in the real and imaginary part, respectively. Since the absorbance is proportional to the imaginary part of the spectral dipole, the Lorentzian distribution is the natural lineshape of a such described absorption resonance.

One effect of the IR pulse is that it can lead to a shift in energy, by coupling the E_1 state to the E_2 state [23]. If this energy shift was constant during the decay of the induced dipole, the resonant absorption feature would shift in frequency accordingly, due to the properties of the Fourier transformation [50]. Since the light-induced coupling depends on the transient and oscillating field intensity of the IR pulse (see Eq. 2.7), this is generally not the case. However, we can describe these transient shifts in energy as a phase φ accumulated during the decay, as suggested by Ott *et al.* [29]. We can rewrite the spectral-dipole as:

$$d(\omega) \propto \int_{-\infty}^{\infty} \left(|d_{01}|^2 \vartheta(t) e^{-i\frac{\Gamma}{2}t} e^{iE_1 t + \varphi} + \text{c.c.} \right) e^{i\omega t} dt. \quad (2.17)$$

which leads to:

$$d(\omega) \propto \frac{e^{i\varphi} |d_{01}|^2}{\frac{\Gamma}{2} + i(\omega - E_1)} + \text{c.c.}, \quad (2.18)$$

and in the imaginary part to:

$$\text{Im } d(\omega) \propto \sin \varphi \frac{\frac{\Gamma}{2}}{\frac{\Gamma^2}{4} + (\omega - E_1)^2} + \cos \varphi \frac{(\omega - E_1)}{\frac{\Gamma^2}{4} + (\omega - E_1)^2}, \omega > 0. \quad (2.19)$$

Ott *et al.* have approximated the energy shift and LIP by a ponderomotive shift [29], while Chini *et al.* [28] have approximated it with the AC Stark shift:

$$\Delta E(t, \tau) \approx \varepsilon_{\text{IR}}(t, \tau)^2 \alpha_n = \varepsilon_{\text{IR}}(t, \tau)^2 \sum_{n \neq m} \frac{E_{nm} |d_{nm}|^2}{E_{nm}^2 - \omega_{\text{IR}}^2}, \quad (2.20)$$

2 Theoretical Description of the Time-Dependent Dipole

where α_n is the state-dependent polarizability. This approximation is appropriate for a strong, non-resonant coupling between bound states, see discussion by Wu *et al.* [23]. The LIP leads to a mixing of the (field-free) Lorentzian lineshape with the dispersive Fano-like. In both approximations this mixing depends on the square of the IR electric field. Hence, a decreased absorbance during time overlap above the E_1 resonance energy and an increased absorbance below the resonance is observed. Since the IR can only affect the population excited by the XUV, a sub-cycle dependence of the LIP features is observed at temporal overlap, since only the part of the IR arriving after the XUV pulse can induce the phase:

$$\varphi(\tau) = \int_{-\infty}^{\infty} \vartheta(t - \tau) \Delta E(t, \tau) dt, \quad (2.21)$$

The square-dependence on the field leads to a 2ω -oscillation in delay. At longer delays, the accumulated light-induced phase is constant, but a fast oscillating phase due to the delay between the XUV and IR pulses leads to hyperbolic absorption and emission features [23].

Towards higher photon energies we find further characteristic features of ATAS. A band of features are found (SB $E_1 + 2\omega$ in Fig. 2.1), that are oscillating with delay time and that show an increasing *slant* with increasing (negative) delay. This sideband is offset by twice the IR photon energy from the E_1 resonance, and a similar feature can be found at twice the IR photon energy below the E_1 resonance energy (SB $E_1 - 2\omega$ in Fig.2.1). These sidebands have been previously identified to originate from an excitation of two-photon dressed states [54]. The amplitude of the oscillating structure depends on the square of the IR electric field at overlap with the XUV pulse [52] and their slant originates from optical interferences of the induced polarization with the XUV field [51].

Similarly, overlap of the IR field with the XUV pulse allows the population of the one-photon dressed states $E_2 \pm \omega$. The E_2 state has no direct transition strength from the ground state in the field-free atom (given that it is a dark state). Hence, these features describe a two-photon XUV \pm IR excitation of the E_2 state, with XUV absorption into a virtual state at $E_2 \pm \omega$ accompanied by a IR photon absorption/emission. Since no spectral features appear at the energies $E_2 \pm \omega$ in the absence of the IR, they have been referred to as light-induced structures (LIS) [23].

The ubiquity of 2ω -oscillations in the observed spectral features indicates the dominant role of processes involving two IR photons. This argument can be extended by doing a power-law analysis. Varying the strength of the IR field, a square-law scaling of the modulation amplitude of the sideband features is observed. Since the same behavior is observed for varying the coupling dipole

2.2 Features of Atom-like Attosecond Transient Absorption Spectroscopy

matrix element d_{12} , one can conclude that the amplitude of the observed side-band signal is dependent on the square of the off-diagonal matrix element of the Hamiltonian in Eq. 2.7.

Chapter 3

3 Experimental Setup

We have introduced the theoretical prerequisites for ATAS in the previous chapter, but what does it take to measure ATAS experimentally? Following our theoretical description, we can sum up the requirements as following: An XUV pulse that covers the spectral region of interest and is sufficiently short in time (e.g. less than the half-cycle of the IR pulse), an (N)IR pulse that is phase-locked to the XUV pulse (i.e. the delay between XUV and IR pulse is controllable to less than the half-cycle of the IR pulse) and a spectrometer that is capable to resolve and record the XUV spectrum. In this chapter, we will introduce an experimental system that fulfills these requirements and with which most of the experiments described in this thesis have been performed. This system, the kHz Attosecond Beamline at the Max-Born-Institute, had been previously commissioned for, among other things, experiments using HHG in combination with NIR pulses to study the role of the AC Stark effect in the ionization of small molecules [55], the relaxation of highly excited states in aromatic hydrocarbons [14, 56] and in combination with UV pulses to study the XUV transient absorption of iodomethane and iodobenzene photodissociation [39, 40]. As such, it has been previously described in detail [14, 40, 55–61], most recently in the thesis of Dr. M. Galbraith [62]. A small overview of the optical system is given in this chapter first, and then recent improvements to the setup, namely an upgrade to the pulse compression system, are discussed.

3.1 Overview

The setup can be divided in four parts: First, a laser system generates NIR pulses with pulse durations in the low femtosecond range (20 fs to 30 fs) and pulse energies in the millijoule regime. Second, these pulses are further compressed in time to few-cycle pulse duration (< 7 fs) using non-linear effects and dispersion management. Third, XUV attosecond pulses are generated by HHG and combined with a time-delayed NIR pulse in a Mach-Zehnder-type interferometer. Fourth, the prepared two-color field is focused into an interaction zone with the sample matter and the XUV spectra are measured by an XUV spectrometer. A drawing of the setup is shown in Fig 3.1.

3 Experimental Setup

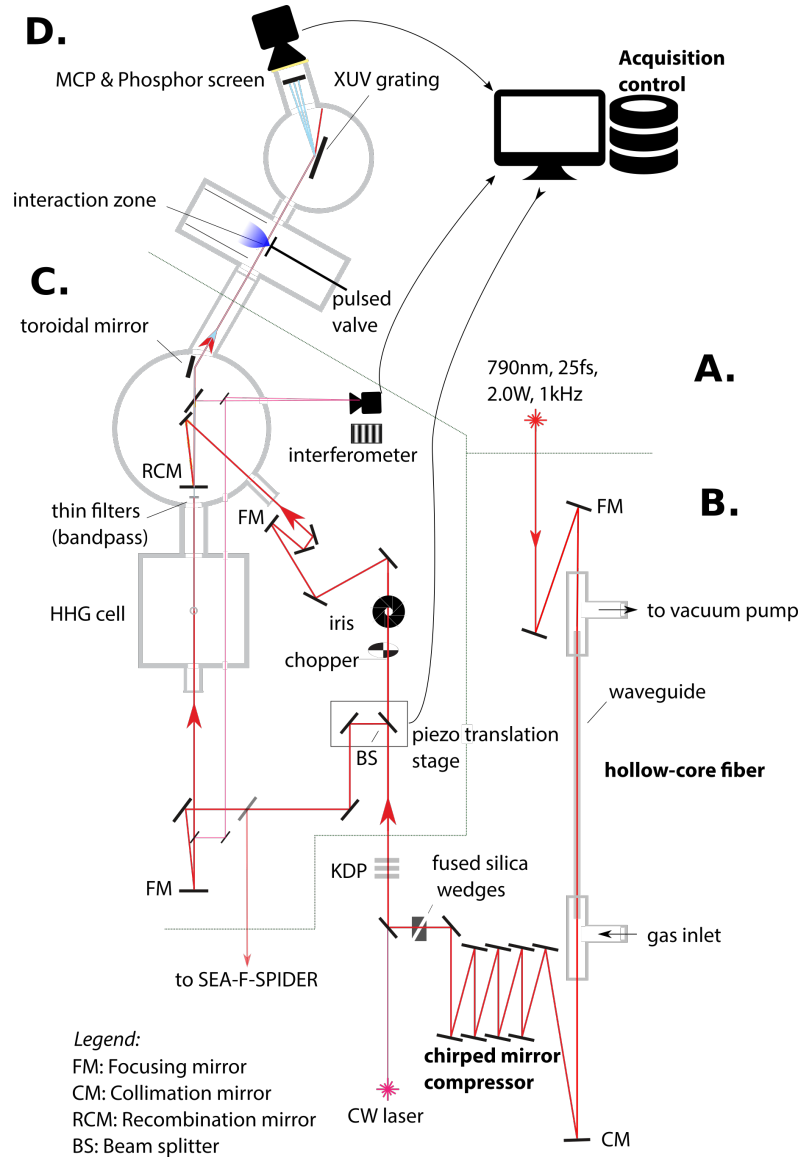


Figure 3.1: Overview of the Experimental Setup. **A.** The laser amplifier system (not depicted) provides ultrashort NIR pulses at a repetition rate of 1 kHz. **B.** The pulses are broadened in spectrum in a hollow-core fiber and compressed in time by the dispersion management optics. **C.** The few-cycle pulses are split by a beam-splitter and delayed with respect to another by a piezo-motorized translation stage. One part of the beam is used to generate high harmonics in a gas cell. Both beams are recombined and refocused into the target chamber. **D.** The XUV and NIR pulses interact with the medium in a pulsed gas jet or an absorption cell (not depicted). The XUV spectra are dispersed and imaged by a multi-channel plate (MCP) and phosphor screen and digital camera.

The laser system has been developed by Amplitude Technologies and features a carrier-to-envelope phase-stabilized [62 Eq. 2.9 (p. 11)] Ti:Sa [63] oscillator [62 p. 44] and a multi-stage chirped-pulse amplifier [64], capable of delivering two NIR laser beams, operating at 10 kHz and 1 kHz, respectively, with a designed output power of up to 20 W each [62 p. 55]. Dispersion in the amplifier can be controlled by compression gratings and an acousto-optical modulator (DAZZLER [65]) and gain-narrowing (i.e. the loss of spectral bandwidth by a stronger amplification in the center of the pulse spectrum than in the wings) in the amplification stages can be limited by an intra-cavity acousto-optical absorber (MAZZLER [66]). With these, pulse durations of 23 fs (FWHM) centered around a wavelength of 790 nm can be achieved at the 1 kHz output, which is the output used for the current experiments. While higher pulse energies are available, only up to 3 mJ of pulse energy are currently used in the beamline. To improve the stability of the laser output, the last amplification stage (a cryogenic booster amplifier) in the 1 kHz beamline can be bypassed (this configuration was used for the experiment in Chapter 4, see Ref. [62 pp. 46 sqq.]).

To obtain few-cycle NIR pulses, 1.3 - 2 mJ of the 1 kHz output are focused into a home-built hollow-core fiber system to broaden the spectrum by self-phase modulation (SPM) in Ne [67, 62 pp. 7-10, 42-44]. The hollow-core fiber hereby acts as a waveguide to keep the laser beam collimated at a small beam diameter (the hollow-core has a diameter of 300 μm) over a long distance (here 1 m), and therefore at a high field intensity. The high intensity of the laser beam leads to a non-linear modulation of the refractive index of the medium inside the hollow-core of the fiber (typically a pressurized rare gas with a high ionization potential, e.g. neon). The non-linear refractive index depends on the change of pulse intensity, which leads to a spectral broadening of the pulse [62 Eq. 2.5 (p. 9)].

The SPM leads to a temporal dispersion of the pulses [62 p. 8], but more significantly the propagation of the broad pulses through the gaseous medium inside the fiber and through air after the fiber leads to dispersion and therefore stretching of the pulses. To obtain short, compressed pulses, this dispersion is compensated by an array of chirped mirrors (Ultrafast Innovations PC70 [62 p. 44]). The dielectric coating of these mirrors allows for a deeper penetration of longer wavelengths while shorter wavelengths are reflected earlier. This optical pathlength difference leads to a negative group-delay dispersion in the pulses (GDD). To be able to fine control the dispersion in the pulses, the system is designed in such a way, that the chirped mirrors overcompensate the positive GDD of the pulses from their propagation through air and glass. Then additional dispersion can be introduced by a pair of wedged fused-silica plates to form a variable thickness glass-plate [62 pp. 59-60]. To characterize the disper-

3 Experimental Setup

sion parameters of the few-cycle pulses, a SEA-F-SPIDER (spatially-encoded arrangement for filter-based spectral phase interferometry for direct electric field reconstruction) device is available [68, 62 p. 45].

To perform pump-probe experiments with few-cycle NIR pulses and HHG XUV pulses, the compressed NIR pulses are split into two beams. The first beam is focused into a vacuum chamber containing a gas cell of 3 mm length to generate high harmonics [62 p. 60]. The gas cell can be flushed with different gases at controlled pressures to obtain optimal XUV intensities in the different spectral regions of interest. For the experiments described here, Xe ($p \sim 23$ mbar) and Ar ($p \sim 42$ mbar) were used. The cell can be moved along the beam direction to optimize phase-matching [69] for short trajectories in HHG [70, 71]. After generation of high harmonics, the co-propagating residual NIR driving-field can be filtered with thin metal filters (100 nm or 200 nm) with different photon-energy band-passes [62 p. 60], such as Al (17 eV to 72 eV) and In (11.5 eV to 16.5 eV). Using the 200 nm thick Al filter conveniently also allows to compensate the dispersion of XUV pulses generated by HHG (*attochirp*, see [67, 72]). Afterwards the filtered beam traverses a central hole in a mirror from the backside.

The second beam can be attenuated by either a set of pre-drilled irises or by a motorized iris, which was installed recently, and the beam pathlength can be controlled with respect to the other beam by reflection off of a mirror on a piezo-motorized translation stage. It is then also focused into the vacuum system and reflected off the front of the holey mirror, so that the combined XUV and IR beams propagate co-linear and with the same focal planes.

The combined two-color beam is then re-imaged 1:1 (2f:2f) by a platinum coated toroidal mirror at grazing incidence into the experiment chamber. There it propagates through the gaseous samples either inside a gas cell inserted from above or through a pulsed gas jet mounted on the side of the chamber. After interaction with the sample in the interaction zone, the beam is dispersed on a concave grating to spectrally disperse the XUV frequencies on a flat spectral plane [40 pp. 34-36]. Two different gratings can be used, depending on the spectral region of interest (600 lines/mm or 1200 lines/mm average density). In the spectral imaging plane, a microchannel-plate (MCP) and phosphor-screen detector together with a digital camera detect the XUV spectra [40 pp. 34-36].

To ensure stability of the NIR and XUV pulse delay, a CW-laser from a mode-stabilized diode co-propagates the interferometer arms and the two beams are imaged onto a digital camera [62 pp. 62-64]. A slight horizontal angle between the two wave-fronts then produces a vertical-stripe interference pattern on the digital camera chip. The relative phase-delay between the two arms is inferred from the position of constructive and destructive interferences in the pattern imaged by the camera [62 Eq. 3.1, p. 63] and fed back to the piezo-motorized

stage to set and control the desired delay between the pulses. Typically, a delay stability of 100 as (RMS) is reached.

3.2 Upgrade to the Pulse-Compression-Scheme

To avoid non-linear effects or damage in the windows leading into the hollow-core fiber, the hollow-core fiber is housed inside a larger, sealed container. This design allows the windows to be moved away from the fiber entrance and exit, i.e. the points of highest field intensity. Previously, the fiber container was statically flushed with up to 2 bar of Ne. At the desired pulse energies, however, the high field-intensity at the entrance of the fiber led to plasma generation in the Ne medium. Such parasitic non-linear effects are known to cause high-order temporal-phases, which are difficult to compensate and compress (such as self-steepening [73]), and decrease coupling efficiency into the fiber. Additionally, high peak powers lead to self-focusing inside the fiber [62 Eq. 2.8, p. 9] and transfer from the desired low order fiber-mode (an $\text{EH}_{1,1}$ (electric hybrid) mode [62 Eq. 2.4, *ibid.*]) to higher order modes, which suffer higher losses through the fiber [74]. A common solution to this problem is to change the fiber-container system from a statically filled operation to a gradient pressure system [75, 76]. Here, the container is divided in two chambers connected by the hollow-core fiber. The first chamber housing the entrance to the hollow-core fiber is evacuated, while gas is continuously pumped into the exit chamber. This leads to a gradient gas pressure inside the fiber. Plasma generation at the entrance and self-focusing are then avoided due to the dilute medium.

Since it was additionally observed, that the high laser intensity in the focused beam led to non-linear effects in the thin fused-silica windows of the container, a new hollow-core fiber system was designed that allowed for an operation using the gradient pressure configuration and the entrance and exit windows were moved further away from the focus position and fiber exit. Due to spatial constraints and compatibility considerations, the hollow-core fiber dimensions themselves were kept equal (length 1 m, 300 μm diameter of hollow-core). To compensate the lessened broadening at the entrance part of the fiber (due to the pressure gradient) the maximum pressure in the container was increased to up to 4 bar.

The increased dispersion in the upgraded pressure-gradient hollow-core fiber system, due to longer propagation through Ne and air, required additional pairs of chirped mirrors to be added. While good results were obtained to compensate and manage the GDD, a large negative third-order dispersion (TOD) was observed in the pulse characterization and in the experiment, where

3 Experimental Setup

it led to pre-satellites of the NIR pulse. While common optical materials (i.e. fused-silica glass) have positive TOD, the GVD is generally larger, meaning additional compensation mirrors for the GDD would be required. However, a few available materials exhibit a stronger TOD than GVD due to anomalous dispersion. Recently, ADP [77] (TOD: $\approx 59 \text{ fs}^3/\text{mm}$, GVD: $\approx 28 \text{ fs}^2/\text{mm}$)¹ and KDP [79] (TOD: $\approx 52 \text{ fs}^3/\text{mm}$, GVD: $\approx 27 \text{ fs}^2/\text{mm}$) crystals have been discussed to compensate the TOD, as well as water cells (TOD: $\approx 33 \text{ fs}^3/\text{mm}$, GVD: $\approx 25 \text{ fs}^2/\text{mm}$ [77]) [80]. While ADP has a slightly better TOD to GVD ratio than KDP, KDP is more widely available. Three pieces of KDP crystals at X-cut direction were available with varying thicknesses to effectively compensate most of the TOD.

The effect of these upgrades is shown in Fig. 3.2. It shows the electric field intensity measured with SEA-F-SPIDER for the static pressure fiber, as used for the experiment described in Chapter 4, and after the upgrade to the gradient pressure system and with 2.5 mm KDP inserted. While the earlier pulses show a train of pre-pulses due to the TOD, the pulses recorded after the upgrade show a cleaner pulse structure and a decreased FWHM duration.

¹TOD and GVD were calculated from Sellmeier equations as reported for ADP and KDP in Ref. [78]

3.2 Upgrade to the Pulse-Compression-Scheme

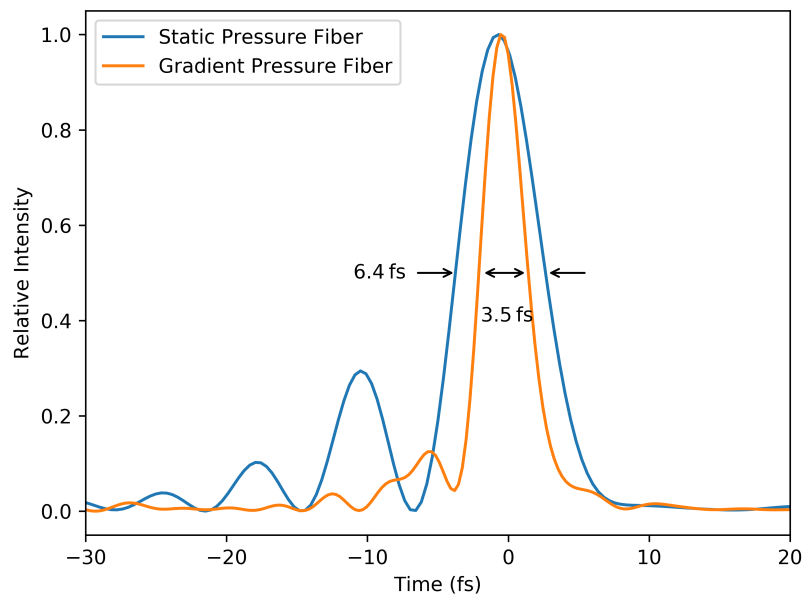


Figure 3.2: Comparison of NIR pulse durations. The pulses generated by the static pressure fiber show a few-cycle main pulse (FWHM 6.4 fs) and a series of pre-pulse satellites due to the uncompensated third-order dispersion. After the upgrade to the gradient pressure fiber and insertion of 2.5 mm KDP crystals, the satellites are reduced and a shorter main pulse of 3.5 fs (FWHM) is achieved. The pulse intensity has been measured and reconstructed by SEA-F-SPIDER [68]

4 State-Resolved Probing of Attosecond Timescale Molecular Dipoles

In this chapter, a study of attosecond transient absorption spectroscopy to obtain a state-resolved picture of the induced-dipole response of iodomethane (CH_3I) molecules is presented. As discussed in Chapter 2, we use the transient modification of absorption of attosecond XUV pulses by a phase-locked NIR-pulse to infer the coupling between the excited states and their polarizability. A spectrally broad XUV attosecond pulse train spanning the region between 45 to 62 eV is used to excite iodine 4d core-electrons into previously unoccupied valence and Rydberg states of CH_3I , that show a stark difference in polarizability.

The present study was motivated by previous work, in which it was shown that attosecond-timescale oscillations of NIR field-driven dipoles in small molecules can be observed by the delay-dependent variation of the ionization by a co-propagating XUV attosecond pulse train [55]. This observation was interpreted in terms of a screening of the XUV radiation by the NIR-induced polarization. It was anticipated that the amplitude of the oscillations should be governed by the polarizability tensor of the electronic states involved in the absorption of the XUV light. However, since only the overall ionization yield was recorded, no state resolution was achieved [55].

The experimental observation of ATAS in CH_3I is presented first in this chapter. Then, the finite-level numerical solution from Section 2.1 and Appendix A is used to simulate the results using *ab-initio* data as input, and a comparison is made to the experimental results. Lastly, a data analysis method based on sin-

This chapter is largely based on a previously published letter, adapted with permission from L. Drescher, G. Reitsma, T. Witting, *et al.* "State-Resolved Probing of Attosecond Timescale Molecular Dipoles." In: *The Journal of Physical Chemistry Letters* 10.2 (2019), pp. 265–269. doi: 10.1021/acs.jpcllett.8b02878. Copyright 2019 American Chemical Society. The author of this thesis performed the experiments and numerical simulation of ATAS signals, wrote the first draft and coordinated correspondence. Special thanks to S. Patchkovskii for performing the *ab-initio* calculations, to G. Reitsma und J. Mikosch for helping with the experiments and to all authors for contributing to the text.

gular value decomposition (SVD) is presented to study the light-induced phase in temporal and spectral decomposition.

4.1 Experimental Observation

The experiment has been performed at the Attosecond Beamline with the statically filled hollow-core fiber and without TOD compensation (see discussion in Chapter 3). Therefore, few-cycle laser pulses centered around 800 nm wavelength with a duration of 6 fs (FWHM) were employed to provide both the NIR field and to obtain XUV pulses by HHG in argon. The NIR pulses were characterized by the SEA-F-SPIDER (see Fig. 3.2). Since the oscillator of the laser system was not CEP-stabilized during this experiment, the CEP of the amplified laser pulses was random from shot to shot. The frequency spectrum of the few-burst XUV attosecond pulse train was near-continuous in the cut-off region between 40 and 60 eV photon energy, matching the investigated 4d pre-edge of iodine. A thin Al filter (200 nm) was used to block residual NIR light from the HHG. An absorption cell (3 mm length) was used in the interaction zone, which was filled with iodomethane gas. The absorption cell was connected to an evaporation reservoir of liquid CH₃I in a temperature bath cooled to a few degrees below the ambient temperature in the laboratory. Using a needle valve, the stagnation pressure was regulated to 0.32 mbar, leading to a background pressure of below 2×10^{-4} mbar in the vacuum chamber containing the absorption cell. XUV-only and XUV+NIR absorption spectra of CH₃I were measured in quick succession by using a chopper wheel to modulate the NIR beam. This configuration allowed recording of the XUV action spectrum, i.e. the NIR-induced change of the XUV absorbance $\Delta A(\omega, \tau)$ as a function of the delay (τ) between the XUV and NIR pulses and the XUV photon energy (ω). Slow drifts in the experimental conditions are efficiently compensated for by this setup. $\Delta A(\omega, \tau)$ is defined as the difference between the logarithms of the measured spectral intensities $I(\omega, \tau)$ with and without the NIR field: i.e. $\Delta A(\omega, \tau) = \log(I_{\text{NIR on}}(\omega, \tau)) - \log(I_{\text{NIR off}}(\omega, \tau))$ (see Eq. 2.6).

In Fig. 4.1 $\Delta A(\omega, \tau)$ is displayed in the spectral range between 48 and 62 eV photon energy, covering the CH₃I 4d-core-to-valence and 4d-core-to-Rydberg transitions. The NIR peak intensity in the interaction region was estimated to be 10^{12} W/cm². The delay τ between the XUV and NIR pulses was repeatedly scanned over 28 fs in 0.2 fs steps and was actively stabilized with a precision of around 100 as (RMS) using a co-propagating diode laser (see Chapter 3). For each XUV-NIR delay, 1024 XUV spectra were recorded both with and without the NIR field, each integrating the measurement of 39 transmitted XUV pulses.

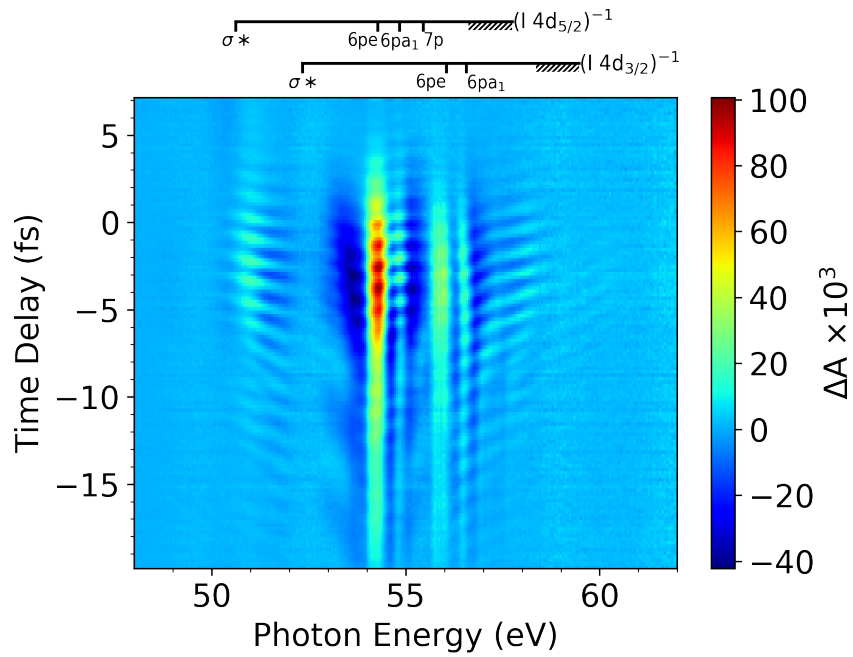


Figure 4.1: Attosecond Transient Absorption of CH₃I: Transient NIR-induced absorbance change $\Delta A(\omega, \tau)$ of iodomethane. Broad XUV spectra from HHG in Argon are used in the CH₃I 4d-core-to-valence and 4d-core-to-Rydberg spectral region. Following excitation by a short attosecond pulse train, a delayed NIR pulse modifies the free induction decay. Negative time-delays indicate the NIR arriving after the XUV pulse. The top scale shows transition energies and spectroscopic assignments from literature (see Table 4.1).

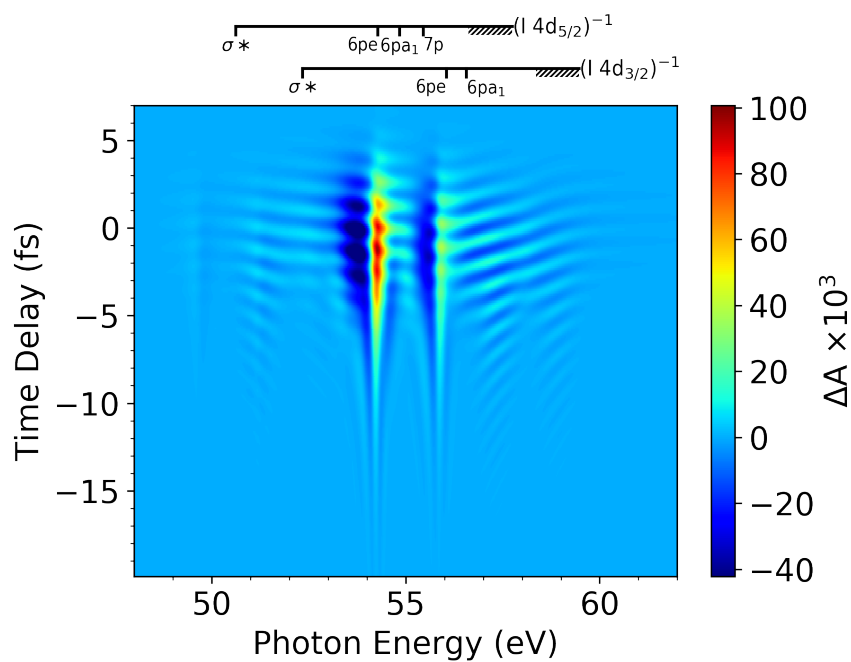


Figure 4.2: Numerical simulation based on *ab-initio* data. The simulated absorbance was averaged over all possible molecular orientations and the NIR carrier-to-envelope phase. The result was shifted in photon energy such that the features associated with the 4d-to-6p transitions occur at the experimentally observed photon energies.

Table 4.1: Literature Spectroscopic Assignments

Transition	E (eV) (Ref. [82])	$f \times 10^2$ (Ref. [82])	$\langle R^2 \rangle$ (a_0^2) ^a
4d _{5/2} (I) \rightarrow σ^*	50.62	0.060	16
4d _{3/2} (I) \rightarrow σ^*	52.34	0.043	16
4d _{5/2} (I) \rightarrow 6p e	54.29	0.016	1.0×10^3
4d _{5/2} (I) \rightarrow 6p a_1	54.84	0.010	1.3×10^3
4d _{5/2} (I) \rightarrow 7p	55.45	0.004	^b
4d _{3/2} (I) \rightarrow 6p e	56.05	0.019	1.0×10^3
4d _{3/2} (I) \rightarrow 6p a_1	56.57	0.014	1.3×10^3

^a Expectation values $\langle R^2 \rangle$ were derived from the *ab-initio* calculations described in Section 4.2

^b Only Rydberg orbitals up to 6p were included in the calculations.

The delay scan was repeated 8 times (30 hours of data acquisition). Small drifts of the XUV-NIR delay (<400 as), attributed to changes of the laboratory environmental conditions, were removed during the analysis by requiring that clearly visible sub-cycle dependent features overlap. In Fig. 1(a) the zero XUV-NIR time delay is assigned to qualitatively coincide with the zero-delay in the numerical simulation (see below). Larger negative time delays correspond to the XUV pulse preceding the NIR pulse.

The static XUV absorption spectrum of CH₃I in the spectral region between 48 and 62 eV photon energy is dominated by electronic excitation around 50.6 eV and 52.3 eV from the iodine 4d_{5/2} and 4d_{3/2} semi-core levels to the lowest unoccupied molecular orbital (LUMO) σ^* , which has valence character (see oscillator strengths f in Table 4.1) [39, 82, 83]. As seen in Fig. 1(a), only a small response $\Delta A(\omega, \tau)$ is observed at these energies (note the XUV target state scale at the top of the figure). A much stronger response is seen at higher photon energies, where significantly weaker transitions from the ground state to low-lying core-excited Rydberg states occur (see Table 4.1) [82, 83]. In this energy region $\Delta A(\omega, \tau)$ shows an oscillation with a 1.3 fs period - i.e. half the period of the NIR field (henceforth called a 2ω oscillation). Smaller values of $\Delta A(\omega, \tau)$ are observed for transitions to higher-lying Rydberg states, converging to the $(4d_{5/2})^{-1}$ and $(4d_{3/2})^{-1}$ ionization potentials (shaded gray areas at the top of Fig. 4.1).

The ATAS in the region between 53 and 57 eV is characterized by a series of features showing a decrease in absorbance below the resonant photon energy accompanied by an increase in absorbance above the resonance. Similar effects have been seen in studies of rare gas atoms and homonuclear diatomic mole-

cules. As discussed in Section 2.2, absorption line profiles are reshaped (from Lorentzian to dispersive, i.e. Fano-like), as a result of an NIR light-induced shift of the transition energy [29]. Due to the AC Stark effect, an NIR light-induced phase (LIP) $\varphi(\tau)$ is accumulated [28, 29, 52], which can be obtained as the time integral over the intensity-dependent Stark shift, see Eq. 2.21. Since the lifetime of the core-excited states of iodine is known to be on the order of the NIR pulse duration, due to the rapid Auger decay of the core-hole [84], the LIP has been parametrized with a population distribution for the excited-state (see Appendix C):

$$\varphi(\tau) = \int_{-\infty}^{\infty} \vartheta(t - \tau) e^{-\frac{\Gamma}{2}t} \Delta E(t, \tau) dt, \quad (4.1)$$

where ΔE is the AC Stark shift (Eq. 2.20), ϑ the Heaviside function accounting for the step-like excitation by the short XUV pulse and the excited state lifetime is $\Gamma = 1/12.9 \text{ fs}^{-1}$ [84]. The lifetime of the excited states spans only about five cycles of the NIR field, resulting in a weak half-cycle dependence of $\varphi(\tau)$. The latter carries over to $\Delta A(\omega, \tau)$, in line with the experimental observations. When the XUV pulse arrives at the molecular sample sufficiently long before the NIR pulse (negative delays in Fig. 4.1), the XUV-excited population has decayed before the NIR field reaches its peak value. Small residual modulations of $\Delta A(\omega, \tau)$ then are caused by NIR pre-pulses, due to the uncompensated TOD.

Since the observed LIP features are dominant in the core-to-Rydberg excitation region, although they are weaker in static absorption, we conclude that the AC Stark shift must be stronger for the Rydberg-excited states than for the valence-excited states. Following our definition of the AC Stark shift from Eq. 2.20 this implies a stronger state-specific polarizability of the Rydberg-excited states in comparison to the valence-excited states.

4.2 Numerical Simulation Using *Ab-Initio* Results

To corroborate our experimental results, the ATAS spectra were simulated numerically. The Time-Dependent Schrödinger equation (TDSE) was solved in a finite basis of field-free states in order to obtain the time-dependent dipole moment and spectral response, as discussed in Section 2.1. The laser fields have been defined as in Eq. 2.13 with parameters listed in Table 4.2. Alternatively, a calculation with the NIR field reconstructed from the SEA-F-SPIDER measurement was performed (see Fig. 4.4(b)). Because the NIR field in the experiment is neither strong enough to induce transitions from the ground state to the core-excited states, nor to deplete or perturb the ground state, interaction of the NIR field with the ground state was neglected.

Table 4.2: Laser Parameters for Numerical Simulation

Parameter	NIR-Pulse	XUV-Pulse
Central Frequency	1.55 eV	52 eV
Pulse Duration (FWHM)	7.0 fs	200 as ^a
Peak Field Intensity	10 ¹² W/cm ²	10 ⁹ W/cm ²

^a Although a short APT was used in the experiment, coherent interaction of the molecule with multiple pulses is unlikely at weak XUV field intensities, therefore justifying the approximation as an isolated pulse.

To account for the rapid decay of the core-excited states due to Auger processes an imaginary energy term $i\Gamma/2$ was introduced, with $\Gamma=1/12.9 \text{ fs}^{-1}$ [84]. XUV and NIR laser electric fields were assumed to be linearly co-polarized. The absorbance was calculated from the single atom response via the Beer-Lambert law, taking into account the estimated gas density and interaction length. The simulations were averaged over 600 orientations of CH₃I, where we made use of the C_{3v} symmetry of CH₃I that limited the necessary range of rotation angles ($0 \leq \beta \leq \pi$ and $0 \leq \gamma < \frac{2}{3}\pi$, see Appendix A). Because the CEP of the NIR laser was not stabilized in the experiment, the calculations were furthermore averaged over 8 uniformly distributed values of the CEP within 0 and 2π . To obtain values for $\Delta A(\omega, \tau)$ comparable to the experiment, the calculated XUV-only absorbance was subtracted.

To obtain the state-to-state transition energies and dipole moments, *ab-initio* calculations were performed using GAMESS-US [30]¹. Scalar relativistic effects were treated using the second-order Douglas-Kross-Hess Hamiltonian [38,39]. Optimization of the neutral ground-state geometry was carried out using the scalar MP2 Hamiltonian. A diffuse-augmented valence triple-zeta basis set recontracted for the DKH Hamiltonian (aug-pVTZ-DK [40]) was used on carbon and hydrogen. A valence triple-zeta-quality DKH-adapted basis set from Ref. [41] was used on the iodine atom. This procedure leads to R(C-I)=2.117Å, R(C-H)=1.082Å, $\alpha(\text{H-C-I})=107.9^\circ$, in close agreement with the experimentally obtained values of R(C-I)=2.134Å, R(C-H)=1.084Å, $\alpha(\text{H-C-I})=111.4^\circ$ [42].

The single-particle molecular orbitals were optimized using a state-averaged minimal-valence CASSCF wavefunction (6 electrons in 4 valence orbitals) with a dynamical-weighting window parameter of 5 eV [43]. All 16 valence states, both singlets and triplets, were included in the averaging. The valence and 4d

¹As previously noted, these calculation were performed by S. Patchkovskii.

4 State-Resolved Probing of Attosecond Timescale Molecular Dipoles

core-excited electronic states and transition dipoles were calculated using spin-orbit configuration interaction (SO-CI) wavefunctions. Only single excitations from the valence CAS(6,4) were included in the SO-CI. Due to computational limitations, it was not possible to include more than 36 external orbitals (out of 160). As a result, our calculation can only capture the lowest Rydberg states below each ionization threshold.

To better represent the Rydberg character of the excited states, the calculation was repeated augmenting the basis set with Rydberg-type basis functions with $N=2.0-4.5$ (increment 0.5) and $L=0,1,2,3$ [44]. The Rydberg basis functions were placed on the center of mass of the molecule.

While we expect the transition dipoles of the large and diffuse Rydberg orbitals to be better represented in the calculation including the Kaufman Rydberg-type basis functions, the more drastic truncation of the CI expansion (36 out of 256 externals for the Rydberg-augmented basis set) reduces the accuracy of the calculated excitation energies. Because we deem the transition energies to be more important in our qualitative study of the CH_3I transient absorption spectrum, we chose to use the results from the first calculation in the simulations presented in this study.

To match the experimentally measured XUV-only absorption spectrum [23] (see Table 4.1), the calculated transition dipole moments between the ground and the 4d core-excited Rydberg states were scaled up by a factor of 3.0. Transition dipole moments between the core-excited states themselves were not scaled. Finally, in order to bring the calculated transition energies close to the measured line positions (see Table 4.1), all transition energies were shifted by -3.8 eV.

We used these *ab-initio* state energies and transition dipole coupling to numerically calculate $\Delta A(\omega, \tau)$ using the extension of our three state model from Chapter 2 as described in Appendix A. The result is shown in Fig. 4.2. All features observed in the experiment (Fig. 4.1) are qualitatively and semiquantitatively reproduced. The modulations of the absorption lineshapes in the region corresponding to the core-to-Rydberg transitions between 54 eV and 57 eV are particularly apparent, while the delay-dependent response in the core-to-valence region between 50 eV and 53 eV is small.

The dominant role of the features associated with the core-to-Rydberg excitation is also apparent in the numerical result. To understand this behavior, the transition dipole moments, obtained from *ab-initio* calculations, involving the relevant core-excited states of CH_3I are shown in Fig. 4.3 as circles with areas proportional to the (absolute) value of the dipole moment. Since many of the coupled spin-orbit states are clustered close-by, and to visualize overlapping contributions, each circle is drawn with an opacity of 5% at the ener-

getic position of the two coupled states. As can be seen, the TDM between the Rydberg-excited states is much stronger than between Rydberg- and valence-excited states. While a coupling exists between the valence-excited states themselves, it is too small to be visible on the scale presented in Fig. 4.3. Since the state-dependent polarizability is proportional to the absolute-square of the TDM (see Eq. 2.20) this supports our argument that the dominant role of the core-to-Rydberg transition is based on their higher polarizability.

At higher and lower energies relative to the central modulation region ($6p^1 4d_{5/2}^{-1}$ Rydberg states), i.e. at 50-52 eV and at 57-59 eV, we observe pronounced broad and slanted fringes both in the measured and calculated $\Delta A(\omega, \tau)$ (Fig. 4.1 and Fig. 4.2). These fringes feature a strong 2ω oscillation. Their energy-dependent slant changes with delay and is tilted in opposite directions on the high and low energy side. As described in Section 2.2 these features originate from a multi-path interference involving two-photon laser-dressed states, i.e. interference between XUV-only and XUV \pm 2 NIR absorption, mediated by dipole coupling to a dark state (i.e. a state without dipole transition from the ground state). The *ab-initio* calculation suggests that the observed fringes result mainly from coupling of the optically bright $6p^1 4d^{-1}$ Rydberg states and the $6s^1 4d^{-1}$ dark states, which are spaced by about 0.8 eV. In contrast with atomic ATAS studies, where couplings to dark states lead to the observation of light-induced structures (LIS) [85], no clearly identifiable LIS are observed in our experiment. These might be hidden due to the broadness of the interference fringes, which results from the high density of Rydberg states.

4.3 Analysis Using Singular Value Decomposition

To further analyze the observed LIP features, singular value decomposition is used to bilinearly decompose the transient absorption spectra. SVD is a numerical algorithm [86] to decompose a (real) matrix \mathbf{M} into three matrices of equal size, such that:

$$\mathbf{M} = \mathbf{U}\mathbf{S}\mathbf{V}^T, \quad (4.2)$$

where \mathbf{S} will be a diagonal matrix carrying the non-negative singular values, which are the square-roots of the Eigenvalues of the matrix $\mathbf{M}\mathbf{M}^T$, and the columns of \mathbf{U} and \mathbf{V} are the orthonormal Eigenvectors of $\mathbf{M}\mathbf{M}^T$ and $\mathbf{M}^T\mathbf{M}$, respectively. SVD is a numerical implementation of a principle component analysis (PCA). The relevance of this abstract mathematical formulation becomes clearer, if this decomposition is applied to the transient absorption spectrogram

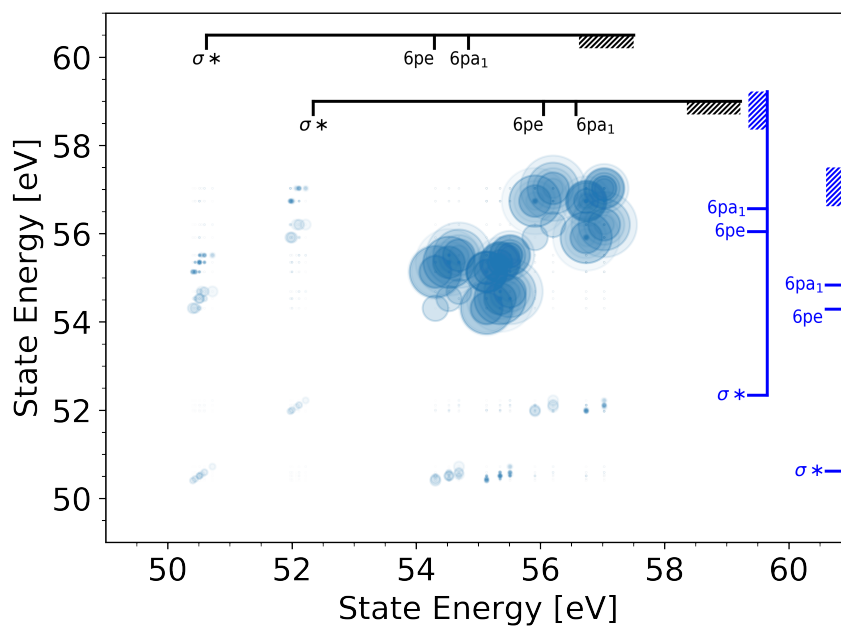


Figure 4.3: Transition Dipole Moments (TDMs) *ab-initio* calculation. The computed three-dimensional transition dipole moments were averaged over all possible orientations of the molecule and projected onto the laser polarization axis. The derived values are proportional to the area of the blue circles and are located at the energetic position of the coupled core-excited states.

4.3 Analysis Using Singular Value Decomposition

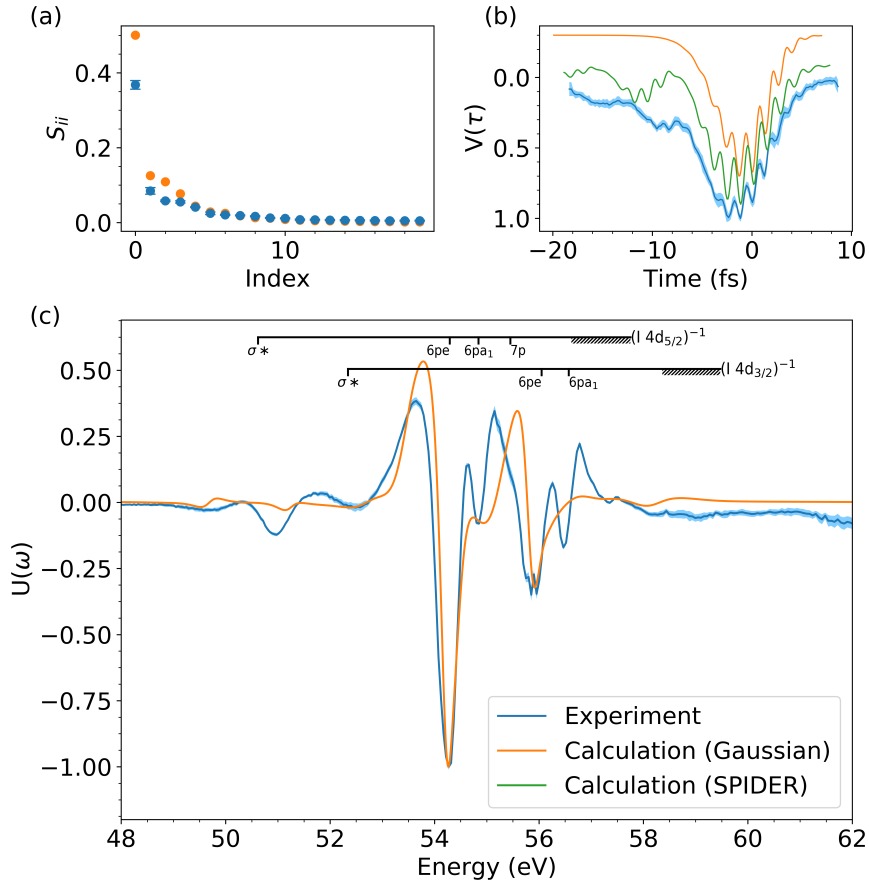


Figure 4.4: Singular Value Decomposition Analysis: **a** Singular values resulting from a SVD of the experimental (blue) and calculated (orange) $\Delta A(\omega, \tau)$ (Fig. 4.1 and Fig. 4.2). **b,c** The singular vectors associated with the dominant singular value. Displayed in (b) is the temporal component $V(\tau)$ of the experimental data (blue), of the calculated data with a Gaussian envelope (orange) and of the calculated data using the NIR-field from the SEA-F-SPIDER measurement (green). Both results from the calculated data have been shifted vertically for clarity. The spectral component $U(\omega)$ displayed in (c) exhibits the different response of core-to-valence and core-to-Rydberg transitions originating from the state-specific polarizability and XUV oscillator strength. Blue errorbars (a) and line-shades (b,c) show the standard deviation of 8 individual measurements.

4 State-Resolved Probing of Attosecond Timescale Molecular Dipoles

$\Delta A(\omega, \tau)$, so that:

$$\Delta A(\omega, \tau) = \sum_n f_n(\omega) s_n g_n(\tau) \quad (4.3)$$

describes the observable $\Delta A(\omega, \tau)$ as a sum over a set of spectral- and temporal-basis functions $f_n(\omega)g_n(\tau)$ weighted by s_n . Since the data obtained from the experiment is a matrix that samples $\Delta A(\omega, \tau)$ at discrete time-delays and spectral frequencies, we can apply SVD to our experimental (or numerical) data matrix to obtain the decomposed features. Intriguingly, a spectral feature that can be bilinearly separated in a set of a single function $f(\omega)$ and $g(\tau)$ would be completely represented by the set of one column-vector in \mathbf{U} and its corresponding column-vector with the same index in \mathbf{V}^T .

Using the derived description of the LIP features from Section 2.2, we will show, that the LIP feature can with good approximation be described in a bilinear representation.

Following Eq. 2.19, $\Delta A(\omega, \tau)$ for a single resonance n at photon energy E_n with spectral width Γ in the presence of the delay-parametrized LIP $\varphi(\tau)$ can be written as:

$$\Delta A_n(\omega, \tau) \propto |d_{0n}|^2 \left(\cos \varphi(\tau) \frac{\frac{\Gamma}{2}}{\sqrt{2\pi} \left[\frac{\Gamma^2}{4} + (\omega - (E_n))^2 \right]} - \sin \varphi(\tau) \frac{\omega - (E_n)}{\sqrt{2\pi} \left[\frac{\Gamma^2}{4} + (\omega - (E_n))^2 \right]} \right), \quad (4.4)$$

where d_{0n} is the transition dipole moment from the ground-state.

For expected peak AC Stark shifts of $\Delta E \leq 1$ eV, the LIP $\varphi(\tau) \ll 1$ and Eq. 4.4 simplifies to

$$\Delta A_n(\omega, \tau) \propto -|d_{0n}|^2 \varphi(\tau) \frac{\omega - (E_n)}{\sqrt{2\pi} \left[\frac{\Gamma^2}{4} + (\omega - (E_n))^2 \right]}. \quad (4.5)$$

Hence, for a single resonance a bilinear approximation holds for $\Delta A_n(\omega, \tau)$ due to the LIP, as long as the light-induced phase (LIP) is small. Likewise, the same is true for a $\Delta A(\omega, \tau)$ from multiple resonances, if the state-specific Stark shift $\Delta E(t, \tau)$ in Eq. 4.1 can be bilinearly factorized. Recalling from Section 2.2 that the energy shift for non-resonant coupling to nearby states can be approximated as the AC Stark shift [23, 28]:

$$\Delta E(t, \tau) \approx \varepsilon_{\text{IR}}(t, \tau)^2 \alpha_n = \varepsilon_{\text{IR}}(t, \tau)^2 \sum_{n \neq m} \frac{E_{nk} |d_{nm}|^2}{E_{nm}^2 - \omega_{\text{IR}}^2}, \quad (4.6)$$

4.3 Analysis Using Singular Value Decomposition

where $\epsilon_{\text{IR}}(t, \tau)$ is the NIR electric field with frequency ω_{IR} , and α_n the state-specific polarizability, which as shown depends on the transition dipole moment to nearby states d_{nm} and the energy difference ω_{nm} between these states.

Combining Eq. 4.5 with $\varphi(t, \tau)$ from Eq. 4.1 and the $\Delta E(t, \tau)$ from Eq. 4.6, $\Delta A(\omega, \tau)$ from multiple resonances can be written as

$$\begin{aligned} \Delta A(\omega, \tau) &\propto \left(\sum_n |d_{0n}|^2 \alpha_n \frac{\epsilon(\omega)}{1+\epsilon(\omega)^2} \right) \left(\frac{1}{\hbar} \int_{-\infty}^{\infty} \vartheta(t - \tau) e^{-\frac{\Gamma}{2}t} \epsilon_{\text{IR}}(t, \tau)^2 dt \right), \\ &= U(\omega) \cdot V(\tau), \end{aligned} \quad (4.7)$$

in other words as the product of a spectral component $U(\omega)$ and a temporal component $V(\tau)$.

$U(\omega)$ thereby represents the spectral manifestation of the LIP, a series of dispersive (Fano-like) lineshapes at the resonance energies of the XUV-excited states with amplitudes proportional to the state-specific polarizability (α_n) and oscillator strength ($f_n \propto |d_{0n}|^2$). $V(\tau)$ represents the temporal manifestation, the NIR laser intensity convoluted with the excited state lifetime and the XUV pulse.

Can the other features, such as sidebands, oscillating fringes and light-induced structures (LIS) (see Chapter 2.2) be bilinearly decomposed? In Chapter 7.2, an analytical solution for these features will be derived in time-domain, with the approximated spectral solutions in Appendix B. There, we will see that these features depend on terms of the form $\cos \omega\tau$, i.e. they have a hyperbolic co-dependence of ω and τ , which can not be bilinearly decomposed. The application of SVD to the data matrix representation of these features will therefore lead to a spread of their contribution over multiple singular values and vectors.

Most importantly, any random statistical noise is not factorisable and is therefore spread over all components of the singular value decomposition. Hence, a SVD is expected to suppress these background effects and highlight the effects of the LIP more clearly. To show the effect of the SVD, the twenty largest singular values for both the experimental and numerical two-dimensional datasets shown in Fig. 4.1 and Fig. 4.2 are plotted in Fig. 4.4(a), ordered by their magnitude, and normalized to a sum of one. The SVD yields a single dominant singular value, followed by a large number of smaller singular values that quickly converge to zero. In the experimental data the convergence is slightly slower, attributed to the noise in the measurement. Even so, Fig. 4.4(a) shows that in the experiment the dominant singular value accounts for 37% of the total variance in the data (50% in the simulated spectrum). The singular vectors associated with the dominant singular value are plotted in Fig. 4.4(b),(c) for both the experimental and simulated results. The principal spectral component $U(\omega)$

(Fig. 4.4(c)) displays the afore-mentioned NIR-induced dispersive (Fano-like) lineshapes, with recognizable contributions from several XUV transitions.

Following our argumentation, the strong response of the core-excited Rydberg states is due to their large polarizability, which originates from the strong dipole coupling among them. As can be quantitatively seen from $U(\omega)$ (Fig. 4.4(c)), the relative intensity of the lowest core-excited Rydberg state is by far dominant, while the intensities of core-excited valence states, carrying a four-fold larger XUV oscillator strength, are minuscule. The coupling effects a LIP $\varphi(\tau)$ that depends on the NIR laser intensity convoluted with the excited state lifetime Γ and XUV pulse (see Eq. (4.1)) and hence shows a clearly visible 2ω oscillation in the principal temporal component $V(\tau)$ (Fig. 4.4(b)). A comparably strong coupling to nearby states is missing for the valence-excited states with which the dominant XUV oscillator strength is associated (at 50-53 eV, see Fig. 4.3), resulting in a low polarizability and a weak signature of these states in the ATAS experiment.

To further illustrate the effect of the SVD, we have reconstructed the two dimensional representation of the experimental data for the different components from:

$$\Delta A_L(\omega, \tau) = \sum_{n \in L} S_n \mathbf{u}_n \mathbf{v}_n^T. \quad (4.8)$$

The spectrograms are shown in Fig. 4.5. Fig. 4.5(a) shows the spectrogram of only the first, dominant singular value $L = 1$, while the spectrogram in Fig. 4.5(b) shows the summed spectrogram of the 15 following singular values $L = 2, 3, \dots, 16$. While the spectral feature of the LIP is seen in (a) as the outer product of the principal components U and V from Fig. 4.4, (b) contains the hyperbolic features such as the fringe sidebands. The sum of the remaining singular values ($L = 17, 18, \dots, 146$) is shown in Fig. 4.5(c), showing the statistical noise. Note the different color-scales for each of these spectrograms. The effect of the noise reduction is also evident in Fig. 4.4, where we have plotted the standard deviation for the experimental data from eight individual measurements as errorbars (a) or shades (b and c).

4.4 Conclusion

Our combined experimental and theoretical study reveals light-induced couplings of core-excited states in molecules in a state-resolved manner. We demonstrate that the state-specific induced dipole response to a moderately intense NIR field is strongly dependent on the dipole coupling to nearby states.

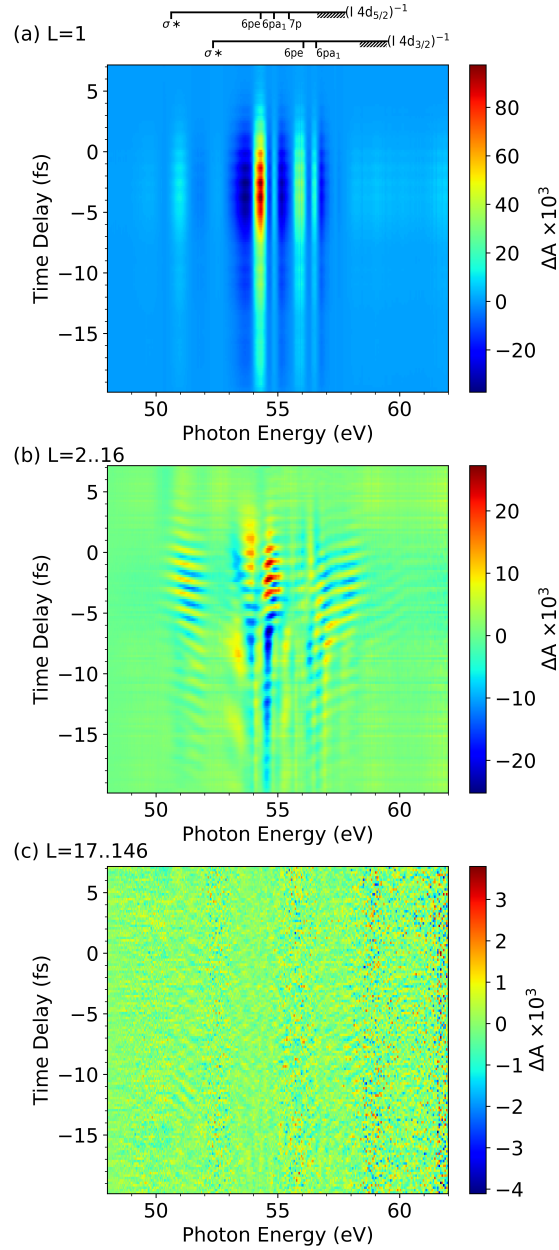


Figure 4.5: Reconstructed Spectrograms from Singular Value Decomposition: The spectrograms are reconstructed from a range of singular values and corresponding vectors (see Eq. 4.8). **a** Spectrogram from the dominant singular value ($L = 1$), which we associate with the LIP signal. **b** Spectrogram from the following singular values ($L = 2, 3, \dots, 16$) shows the hyperbolic features, mainly the perturbed induction decay and sideband fringes. **c** The weakest singular values ($L = 17, 18, \dots, 146$) show the statistical noise of the measurement.

This coupling is particularly strong between the Rydberg-excited states. The transition dipole moment can be written in integral form as:

$$\mathbf{d}_{nm} = \int \Phi_m^* \mathbf{r} \Phi_n d\mathbf{r}, \quad (4.9)$$

i.e. the spatial integral over the final- and initial-state wavefunction and the dipole-operator \mathbf{r} . If we assume, that the excited state wavefunction is dominated by the radial term of the highest occupied orbital, the large, diffuse Rydberg orbitals would result in a larger polarizability compared to the valence orbitals, which outweighs by far the effect of the smaller core-to-Rydberg oscillator strengths. The expectation values $\langle R^2 \rangle$ for the Rydberg orbitals are larger by about two orders of magnitude than for the valence orbitals (see Table 4.1).

Our study shows, that ATAS in molecules is sensitive to the magnitude of these light-induced couplings. These couplings cannot be revealed in linear spectroscopy. Due to the short lifetimes of the core-hole states they are also difficult to observe with standard two-photon spectroscopies. By accessing a regime where core-to-valence and core-to-Rydberg transitions co-exist, we show that while the valence states dominate the XUV absorption in the absence of the field, the Rydberg states dominate the NIR-dressed XUV absorption. While our observations can be understood by combining several elements of well-known physics this is an important and novel aspect of ATAS that is general to polyatomic molecules and is absent in the work on atoms and diatomic molecules reported in recent years. It also represents a first hint at how ATAS can become complementary to the existing spectroscopic techniques. It enables the reconstruction of the molecular transition dipole moments from a local point-of-view inside the molecule, allowing for a reduction in complexity of states in the molecular valence. Our study hence paves the way to observing ultrafast intra-molecular dynamics, since changes in absorbance are sensitive to small shifts in coupling and energy during the very short decay times of core-excited states. With the advent of HHG-based XUV light sources in the water window [87, 88] with attosecond pulse duration, where transitions from core-orbitals in nitrogen, carbon and oxygen atoms are located, we anticipate that ATAS of light-induced couplings in molecules will become a tool to study ultrafast phenomena in organic molecules, not only with excellent time and energy resolution, but also from the local perspective of an intra-molecular reporter atom.

5 Chapter 5

5 Extreme-ultraviolet Refractive Optics

Refraction is a well-known optical phenomenon that alters the direction of light waves propagating through matter. Microscopes, lenses and prisms based on refraction are indispensable tools for controlling the properties of light beams at visible, infrared, ultraviolet and X-ray wavelengths [90]. In the XUV to soft X-Ray region, however, refractive optics have so far been absent because of the small refractivity of high energy photons and the large absorption of common optical materials in those regions.

The low refractivity for high energy photons was already discovered for X-Rays by W. Röntgen in 1895, when he attempted refraction experiments using prisms and lenses [91]. Since he observed no significant deflection of the X-rays, he concluded that refractive lenses are not suitable for focusing X-ray radiation. A century later, a compound refractive lens consisting of a lens array was nevertheless developed for the hard X-ray regime, assisted by the comparably low absorption in this spectral region. Compound refractive lenses are used to focus X-rays emitted from modern synchrotron [92, 93] and free-electron laser facilities [94, 95]. They have e.g. been applied for hard X-ray microscopy [96], for X-ray nanofocusing [97], for the investigation of crystal scattering [98], as well as for coherent diffractive imaging of nanoscale samples [99]. The large absorption of solids in the XUV region, however, excludes the use of compound refractive lenses. As an alternative, the use of specially designed microscopic refractive lenses has been proposed [100, 101]. However, the need to use very thin lenses with a sophisticated design makes a practical implementation extremely challenging, and no demonstrations exist to date. Hence, focusing of XUV and soft X-ray pulses has so far typically been achieved by reflective mirrors and diffractive Fresnel zone plates [102].

This chapter is in large parts based on a previously published letter: L. Drescher, O. Kornilov, T. Witting, *et al.* “Extreme-Ultraviolet Refractive Optics.” In: *Nature* 564.7734 (2018), p. 91. doi: 10.1038/s41586-018-0737-3. The author of this thesis performed and evaluated the prism experiments in collaboration with B. Schütte, who performed the lens experiments and drafted a first version of the letter. Thanks to O. Kornilov for the numerical calculations. Thanks to all authors for contributing to the text.

In this chapter we demonstrate that control over the refraction of XUV pulses can be achieved by using gases instead of solids. In the first part, broadband HHG pulses are spectrally dispersed and deflected when propagating through a gas jet with a density gradient, which induces an optical path gradient across the XUV beam profile. The operation principle thus resembles that of a prism that leads to a frequency-dependent deflection of the XUV beam. In the second part, we demonstrate the operation of a deformable XUV refractive lens using a cylindrical gas jet. Individual harmonic orders are focused to a spot size that is controlled by the type of gas and the gas pressure. In the third part, a combination of transient absorption and transient refraction spectroscopy is proposed to reconstruct the full complex transient dipole spectrum.

5.1 Gas Phase XUV Prism

In the vicinity of atomic resonances, the refractive index n exhibits a dispersive lineshape as depicted in the top part of Fig. 5.1(a). As the photon energy approaches the resonant energy, n first increases and then steeply decreases across the resonance to values below unity, before increasing again. [103, 104].

Our scheme for control over the refraction of XUV pulses employing an inhomogeneous gas target is presented in the middle and bottom panels of Fig. 5.1(a). The XUV pulses pass through a gas jet, which propagates in a direction perpendicular to the XUV beam and which has a density gradient in the vertical direction (middle panel in Fig. 5.1(a)). When the XUV pulse crosses the gas jet off-center, the latter acts as a prism and induces angular dispersion and deflection of the XUV radiation. For an XUV beam that is incident below the center of the gas jet, spectral components of the beam for which $n > 1$ are deflected upwards (red color in the bottom panel of Fig. 5.1(a)), whereas spectral components of the beam, for which $n < 1$, are deflected downwards (blue color in the bottom panel of Fig. 5.1(a)).

An experimental demonstration of the prism concept, that has been performed at the Attosecond Beamline described in Chapter 3, is presented in Fig. 5.1(b,c). Fig. 5.1(b) shows an XUV spectrum produced by HHG in Xe using NIR pulses with a duration of 4.5 fs. The spectrum was measured on a 2D detector, in which the horizontal axis represents the axis along which the XUV spectrum is dispersed using a flat-field grating spectrometer.

Control over the XUV refraction was achieved by a pulsed gas jet that was positioned near the XUV focus. The gas jet was generated by a piezoelectric valve with a nozzle diameter of 0.5 mm. A three-dimensional manipulator was used to position the gas jet with respect to the XUV focal spot. The XUV beam

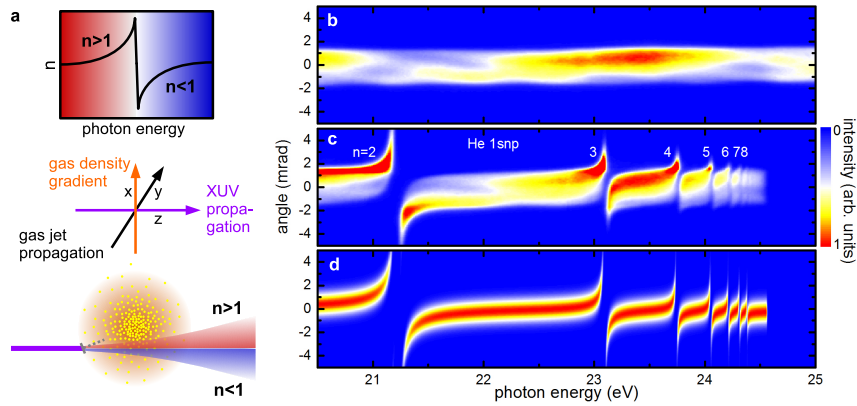


Figure 5.1: XUV refractive prism. **a**, Top panel: Dispersive lineshape of the refractive index in the vicinity of an atomic resonance. Spectral components at photon energies below the resonance ($n > 1$) are referred to by a red color, whereas spectral components at photon energies above the resonance ($n < 1$) are referred to by a blue color. Middle panel: Experimental configuration, showing an XUV pulse (violet arrow) that crosses a gas jet (black arrow), which has a density gradient in the vertical direction (orange arrow), at right angles. Bottom panel: Deflection of an XUV pulse propagating below the center of the gas jet. **b**, Angle-resolved spectrum of a broadband HHG pulse measured in the absence of the gas jet. The angular divergence of the XUV beam in the vertical direction is reflected in the spatial distribution along the vertical axis. **c**, The same spectrum after propagation at a distance of 0.3 mm below the center of a dense He gas jet (generated using a backing pressure of 10 bar) shows clear signatures of refraction. Spectral components with photon energies just below the $1snp$ resonances of He are deflected upwards, whereas spectral components just above these resonances are deflected downwards. The deflection angles are largest close to the $1s2p$ resonance and decrease for higher resonances due to the decreasing oscillator strengths. Above the ionization potential of He (at 24.58 eV), the XUV radiation is strongly absorbed. **d** Simulation of the XUV refraction in an inhomogeneous He gas jet, taking into account $1snp$ resonances with $n = 2, 3 \dots 8$. The simulation indicates that using a backing pressure of 10 bar, a gas jet with a peak density of 9×10^{19} atoms/cm³ (corresponding to a pressure of 3.7 bar at 300 K) was achieved in the interaction zone.

crossed the gas beam close to the exit of the nozzle, at a distance of a few 100 μm where gas densities up to 10^{20} cm^{-3} were achieved. When applying a certain backing pressure, we estimate the peak pressure in the interaction region to be smaller by a factor of about 3 (when assuming a temperature of 300 K) which we find to agree well with the theoretical calculations (see below). We estimated the amount of matter intersected by the beam (i.e. the pressure-length product) in the direction perpendicular to the nozzle direction and the beam propagation direction by moving the nozzle vertically and comparing the absorbance in the spectral region above the He ionization potential (i.e. between 25 eV and 26 eV). An approximately parabolic dependence of the pressure-length product on the nozzle position is observed with a diameter of 1 mm. The XUV focal spot size ($\approx 100 \mu\text{m}$) was small compared to the extension of the gas jet at the laser position. The gas density gradient along the nozzle direction is estimated to be much smaller than the density gradient in vertical direction.

When the broadband HHG pulses propagate 0.3 mm below the center of a dense He gas jet, the XUV spectrum is strongly modified, see Fig. 5.1(c). Spectral components below the $1snp$ ($n = 2, 3, \dots$) resonances of He are deflected upwards, whereas spectral components above the $1snp$ resonances are deflected downwards.

Microscopically, refraction is explained in terms of the oscillating dipole induced by the XUV pulse. The incoming XUV pulse excites atoms that re-emit radiation at the same photon energy (free induction decay) [20–24]. Our prism exploits the fact that this re-emitted radiation is phase-shifted with respect to the exciting XUV pulse. By inducing a gas density gradient, the upper part of the XUV pulse acquires a different phase shift than the lower part, which leads to a tilt of the XUV wavefront.

Revisiting the propagation equation presented in Chapter 2, the XUV field after propagation through the gas jet is:

$$\varepsilon(\omega, x, z = L) = \varepsilon(\omega, x, z = 0)e^{-\alpha(\omega, x)L}e^{i\Delta n(\omega, x)\frac{\omega}{c}L}, \quad (5.1)$$

where we have introduced x as the coordinate in the direction of the density gradient. While the interaction with the medium could be calculated using the semi-classical methods introduced in Chapter 2, to estimate the phase-front tilt we will use the classical Lorentz-Lorenz [105] formula to directly calculate the complex refractive index \tilde{n} , since only monochromatic effects need to be considered:

$$\frac{\tilde{n}^2 - 1}{\tilde{n}^2 + 2} = \rho(x)\frac{e^2}{3m_e\epsilon_0} \sum_j \frac{f_j}{\omega_{0j}^2 - \omega^2 - i\Gamma_j\omega}. \quad (5.2)$$

Here $\rho(x)$ is the (spatially-dependent) atomic density, e is the electron charge, m_e is the electron mass, ϵ_0 is the vacuum permittivity, f_j is the oscillator strength of the transition j , ω is the angular frequency of the XUV light, and ω_{0j} and Γ_j are the resonant frequencies and widths, respectively. The real part of the refractive index, n , and the absorption coefficient, α , are then calculated according to the following equations:

$$\Delta n(x) = \sqrt{0.5 \times (|\tilde{n}(x)|^2 + \text{Re}\{\tilde{n}(x)^2\})} - 1, \quad (5.3)$$

$$\alpha(x) = \sqrt{0.5 \times (|\tilde{n}(x)|^2 - \text{Im}\{\tilde{n}(x)^2\})}. \quad (5.4)$$

Values for the oscillator strengths and linewidths were taken from Refs. [106, 107].

If the beam propagates 0.3 mm below the center of the beam, we estimate that the pressure-length product is 0.84 of the maximum value (i.e. the center of the gas jet) at the upper half-maximum and 0.36 at the lower half-maximum of the Gaussian beam profile. With an estimated peak pressure-length product of $p \cdot l = 2.22 \text{ bar} \cdot \text{mm}$ at a backing pressure of 10 bar, we can estimate the wavefront tilt based on Eq. 5.1 and Eq. 5.2. We have kept the interaction length $L = 1 \text{ mm}$ in Eq. 5.1 and varied the atomic density in Eq. 5.2 to match the pressure-length products. At a photon energy of 21 eV, i.e. 0.22 eV below the 1s2p resonance, the wavefront tilt then is 0.03° . Different spectral components are deflected into different directions, with the stronger deflection occurring close to a resonance.

The effect of the wavefront tilt in the far-field can be described with the Fresnel-Kirchhoff diffraction formula [105]. We assume an infinite aperture in the direction of the density gradient (x -direction) to calculate the electric field at a displaced coordinate ξ on a screen at distance S for each frequency ω :

$$\varepsilon(\xi, z = S) = -\frac{i\omega}{c} \int_{-\infty}^{\infty} \varepsilon(x, z = L) \exp\left[i\frac{\omega}{2Sc}(x^2 - 2x\xi)\right] dx, \quad (5.5)$$

where $\varepsilon(x, z = L)$ is the electric field after interaction with the gas jet. Note that the integral is a Fourier integral ($\int_{-\infty}^{\infty} f(x)e^{i\xi x} dx$), which allows for a fast numerical calculation. Eq. 5.1 is used to calculate the propagation of the field through the medium at each coordinate x with the respective density of the gas-jet $\rho(x)$. The different refractive indices $n(\omega, x)$ across the spatial dimension hereby act as a phase mask that induces the wavefront tilt. The initial beam can be described with a Gaussian distribution of amplitude in the x -direction and a flat spatial phase.

As shown in Fig. 5.1(d), the simulation reproduces the experimental result well.

The deflection of the XUV beam can be controlled by varying the gas pressure. Angle-resolved spectra for He backing pressures of 1 bar, 3 bar and 9 bar are presented in Fig. 5.2(a-c) and show increasing deflection for increasing backing pressure. The average deflection angle as a function of the photon energy (determined by comparing the center-of-mass of the distribution along the vertical axis with and without the He gas jet) is plotted in Fig. 5.2(d) for backing pressures of 3 bar (cyan solid curve) and 9 bar (orange solid curve). For small angles, the deflection is proportional to the refractivity (i.e. $n - 1$), which was calculated using the Lorentz-Lorenz formula. The shapes of the measured deflection angles (solid curves) and the calculated refractivities (dotted curves) agree well, apart from the region near resonance, where the angular acceptance and the resolution of the XUV spectrometer are no longer sufficient.

5.2 XUV Refractive Lens

The observed deflection of XUV pulses in the vicinity of atomic resonances can be exploited for the design of an XUV refractive lens. This is demonstrated in a second set of experiments, which have been performed by Dr. B. Schütte using high harmonics with a narrow bandwidth of 100 – 200 meV and a low beam divergence beamline [108]: NIR pulses with a pulse energy of 30 mJ and a duration of 35 fs were generated using a home-built Ti:Sa amplifier [109] and high harmonics were generated by focusing the NIR pulses using a spherical mirror with a focal length of 5 m into a 10 cm long gas cell that was filled with Xe. In order to focus the XUV beam, a piezoelectric valve with a nozzle diameter of 1 mm was positioned at a distance of 5 m behind the generation cell. Before propagating through the gas jet, the HHG beam was truncated by a slit to a horizontal width of 200 μm to increase the spectral resolution in the spectrometer located downstream. A 100 nm thick Al filter was used in the He experiment, which was removed for the Ar experiment, because it absorbs the 9th harmonic. An XUV spectrometer consisting of a plane grating, a multichannel plate and phosphor screen assembly and a digital camera was used to spectrally and spatially characterize the XUV pulses.

Fig. 5.3(a) depicts the spatially-resolved spectrum around 20.2 eV (corresponding to the 13th harmonic) as recorded at a distance of 6 m behind the HHG cell. The photon energy of 20.2 eV is about 1 eV below the 1s_{2p} resonance of He. The spatial extension of the harmonic along the vertical axis (2.7 mm, see Fig. 5.3(d)) corresponds to a FWHM divergence of 0.45 mrad. When a He gas

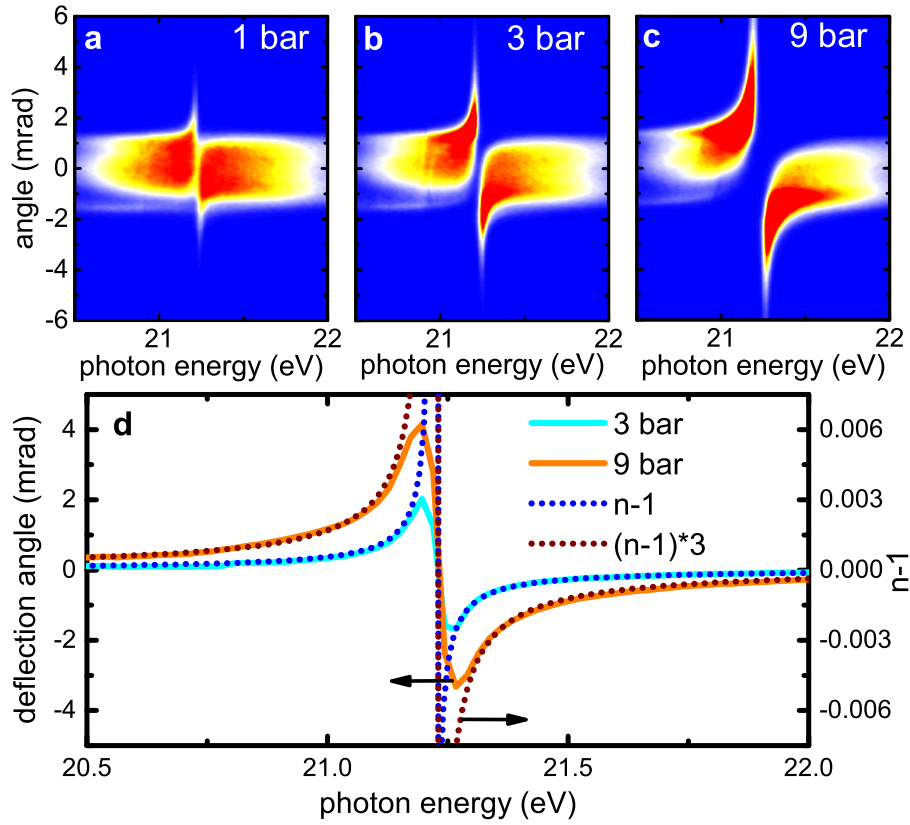


Figure 5.2: Control over the XUV deflection by the gas pressure. Angle-resolved XUV spectra after propagation at a distance of 0.3 mm below the center of a He gas jet using backing pressures of **a**, 1 bar, **b**, 3 bar and **c**, 9 bar. **d**, The average deflection angle as a function of the photon energy for backing pressures of 3 bar (corresponding to a peak pressure in the interaction zone of about 1 bar, cyan solid curve) and 9 bar (orange solid curve). For comparison, the calculated refractivity (i.e. $n - 1$) at standard temperature (273.15 K) and standard pressure (1 bar) is plotted on top of the deflection results (blue dotted curve). Note that the calculated refractivity is proportional to the pressure.

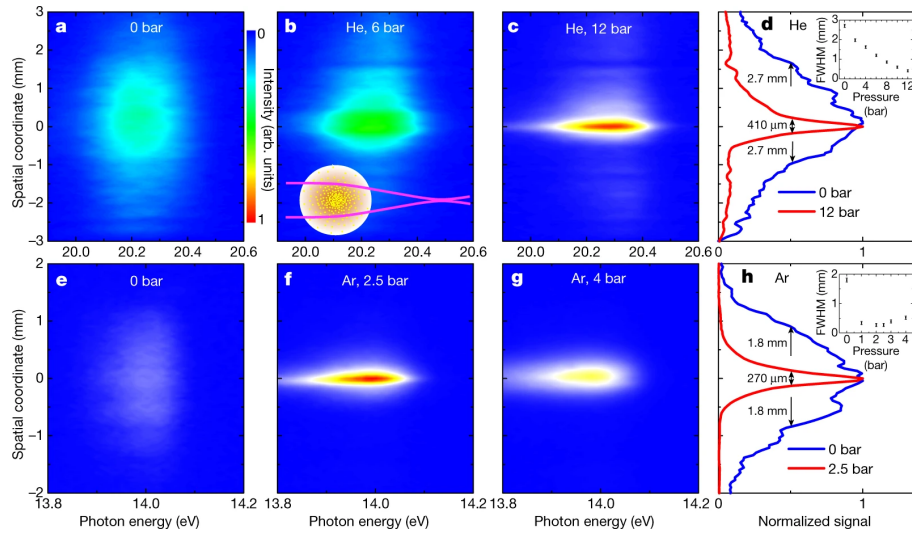


Figure 5.3: XUV refractive lens. **a**, Spatially-resolved spectrum of the unfocused 13th harmonic. The divergence of this harmonic is altered after propagation through a He gas jet, which results in a smaller vertical beam size on the detector, as shown for backing pressures of **b**, 6 bar and **c** 12 bar. **d**, Comparison between the vertical beam profile using backing pressures of 0 bar (blue curve) and 12 bar (red curve). **e**, Spatially-resolved spectrum of the 9th harmonic, whose photon energy is close to the 3d and 5s resonances of Ar. **f**, Focusing of this harmonic is achieved by an Ar gas jet at a backing pressure of 2.5 bar. **g**, When further increasing the backing pressure to 4 bar, an increasing beam size is observed, since the Ar lens focuses the XUV beam between the gas jet and the detector. **h**, The vertical beam profile of the 9th harmonic for Ar backing pressures of 0 bar (blue curve) and 2.5 bar (red curve). The inset shows the pressure-dependent spot size, where the error bars reflect the uncertainties in determining the spot sizes.

jet with a parabolic profile [110] and a spatial extent of about 2.5 mm (that is, similar to the XUV beam diameter, which is 2.3 mm at this point) is placed 0.9 m in front of the detector, the former acts as a lens, as sketched in the inset of Fig. 5.3(b). Fig. 5.3(b,c) demonstrates focusing of radiation at 20.2 eV for two different backing pressures. Fig. 5.3(d) shows that the FWHM in the vertical direction is reduced from 2.7 mm to 410 μm by operating the gas jet at a backing pressure of 12 bar (the highest pressure used in the experiment, leading to a peak density in the experiment of about 1×10^{20} atoms/cm³). We found that absorption of the XUV beam by the He lens is small, i.e. below the estimated detection threshold of 5 %. The geometry of the current experiment leads to focusing in one dimension, analogous to the focusing by a cylindrical lens. A sequence of two perpendicularly placed gas jets, each with a cylindrically shaped density gradient, could be used to focus XUV pulses both horizontally and vertically.

As the deflection of XUV radiation increases for photon energies approaching an atomic resonance, we have studied another example using radiation at 14.0 eV (corresponding to the 9th harmonic, see Fig. 5.3(e)), which is close to the $3p^55s$ (at 14.09 eV) and $3p^53d$ (at 14.15 eV) resonances of Ar. In this case, an Ar gas jet with a moderate backing pressure of 2.5 bar (corresponding to a peak density in the interaction region of about 2×10^{19} atoms/cm³) was used to focus the XUV radiation, as shown in Fig. 5.3(f). When further increasing the gas backing pressure to 4 bar, the beam size on the detector increases again (Fig. 5.3(g)). In this case, the focal plane shifts closer to the jet, and a divergent beam is detected.

A minimum beam size of 270 μm was observed in the experiments with the Ar lens (Fig. 5.3(h)), which is small enough for many applications including photoion and photoelectron spectroscopy. Some applications, however, such as the investigation of XUV-induced nonlinear processes [108, 111–114] and single-shot HHG-driven coherent diffractive imaging using photon energies around 20 eV [115] require substantially smaller XUV spot sizes. The achievable focal spot size is limited by geometric and chromatic aberrations. For ideal focusing conditions, the profile of the gas density integrated along the XUV beam propagation axis needs to be parabolic. While the gas density profile generated by a cylindrical nozzle is parabolic to a good approximation [110], deviations from the parabolic shape lead to geometric aberrations, affecting the focal spot size that can be achieved. Furthermore, a density gradient is present along the propagation axis of the gas beam that leads to geometric aberration. In the future, the gas density profile may be optimized by tailoring the gas nozzle designs [110].

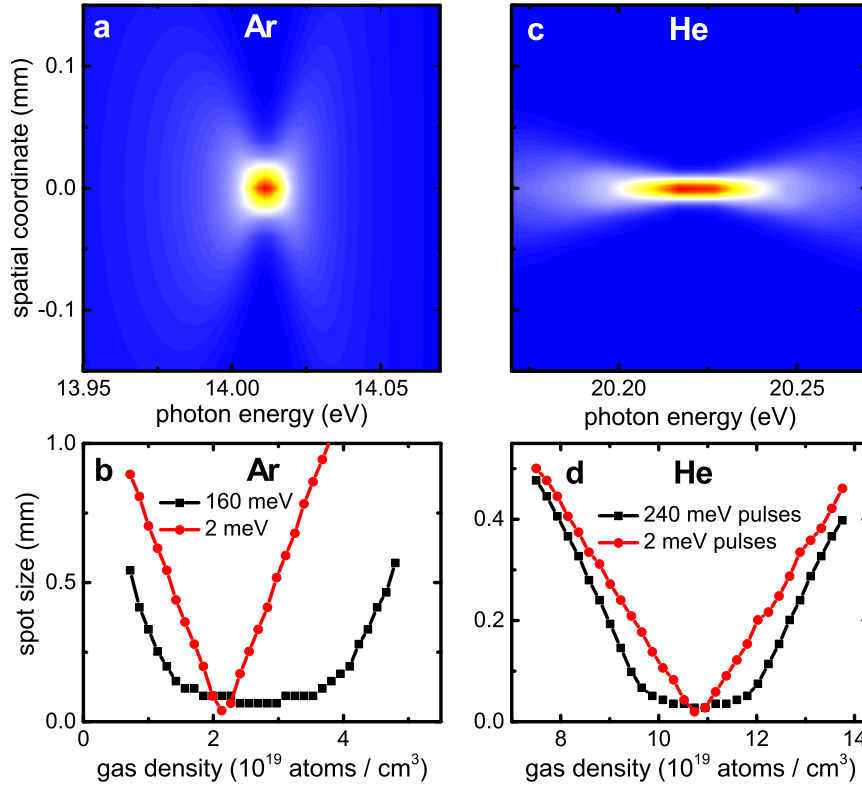


Figure 5.4: Simulation of the XUV focus. **a**, Simulated focus in the vertical direction as a function of the photon energy following propagation of a 9th harmonic XUV pulse at 14.015 eV (1.9 mm FWHM diameter) through an Ar gas jet with a peak density of 2.2×10^{19} atoms/cm³ (corresponding to a pressure of 0.9 bar at 300 K). Due to chromatic aberration, the XUV spot size depends on the photon energy. **b**, Spot size as a function of the Ar gas density for XUV pulses with a bandwidth of 160 meV (black curve) and 2 meV (red curve), showing minimal spot sizes of 74 and 40 μm , respectively. **c**, The chromatic aberration is reduced for photon energies that are further away from the resonance. This is shown for the example of a 13th harmonic XUV pulse at a photon energy of 20.22 eV (2.4 mm FWHM diameter) that propagates through a He gas jet with a peak density of 1.0×10^{20} atoms/cm³ (corresponding to a pressure of 4.3 bar at 300 K). **d**, Spot size as a function of the He gas density for XUV pulses with a bandwidth of 240 meV (black curve) and 2 meV (red curve), which exhibit minimal spot sizes of 28 and 20 μm .

Assuming an ideal parabolic gas density profile, the spot sizes achieved by an Ar lens for a collimated XUV beam at 14.0 eV with a FWHM diameter of 1.9 mm have been simulated¹. The focal length f of the gas-phase lens is thereby estimated as a biconvex lens with equal radii as:

$$f = \frac{R}{2(n_2 - n_1)}, \quad (5.6)$$

where R is the radius of the curved surface, n_2 is the refractive index of the lens material and n_1 is the refractive index of the surrounding material (i.e. vacuum in our case). The biconvex He lens is approximated with a Radius of 1 mm, corresponding to the density profile of the parabolic gas jet. The refractive index at 20.22 eV at a gas density of 1.07×10^{20} atoms/cm³ is $n_2 = 1.000542$. Using these values, a focal length of 92 cm is obtained, which is in good agreement with the results shown in Fig. 5.4(d).

The XUV spot size at a distance of 90 cm behind the gas lens depends on the photon energy, as shown in Fig. 5.4(a). This chromatic aberration, which is a direct consequence of the variation of the refractive index within the XUV bandwidth, results in a spot size that is larger than that of a monochromatic XUV beam. Note that this effect is not visible in the experimental data due to the spectral resolution of about 100 meV and the spatial resolution of about 100 μ m.

The gas-density dependent spot size at a distance of 90 cm from an Ar lens is plotted in Fig. 5.4(b), showing a minimum spot size of 74 μ m for an XUV pulse with a bandwidth of 160 meV, which is similar to the bandwidth of the 9th harmonic observed in the experiment (black curve in Fig. 5.4(c)). When reducing the XUV bandwidth to 2 meV, a minimum spot size of 40 μ m is obtained (red curve in Fig. 5.4(b)). The measured spot sizes show little variation over a broad range of gas densities because of chromatic aberration, which explains the behavior shown in the inset of Fig. 5.3(h). When reducing the XUV bandwidth in the calculation to 2 meV, a minimum spot size of 40 μ m is obtained (red curve in Fig. 5.4(b)). The chromatic aberration is reduced when exploiting refraction due to a resonance that is further away from the XUV photon energy, as shown for a He lens with a FWHM diameter of 2.4 mm in Fig. 5.4(c). A minimum spot size of 28 μ m is obtained in this case using a pulse with a bandwidth of 240 meV (similar to the bandwidth of the 13th harmonic used in the experiment shown in Fig. 5.3, black curve in Fig. 5.4(d)), and it is reduced to 20 μ m for a pulse with a bandwidth of 2 meV (red curve in Fig. 5.3(d)).

The simulations show that by further increasing the gas density to 3.1×10^{20} atoms/cm³, corresponding to a shorter focal length of 30 cm, a focal

¹As mentioned, these simulations have been performed by O. Kornilov

spot size below $10\ \mu\text{m}$ could be achieved (resulting in an XUV intensity of up to $10^{13}\text{W}/\text{cm}^2$). This is in the range of recent experiments studying XUV-induced Rabi cycling [116], XUV double ionization of atoms [113] and single-shot coherent diffractive imaging [115], where spot sizes between $3\ \mu\text{m}$ and $16\ \mu\text{m}$ were used, thus putting us in the realm where XUV nonlinear optics experiments become possible.

When using a refractive lens to focus ultrashort XUV pulses, another important aspect is the XUV pulse duration at the focus. Since HHG and free-electron laser pulses have an intrinsic negative chirp [117, 118], a refractive lens, which induces a positive chirp, can lead to compression of the XUV pulses. Assuming a pulse with a duration of 24 fs and a chirp of $-8\ \text{meV}/\text{fs}$, which is in the range of previous measurements of the 13th harmonic [119], the simulations show compression to 16 fs by a He lens with a peak gas density of $4.9 \times 10^{19}\ \text{atoms}/\text{cm}^3$ (corresponding to a focal length of 1.9 m). The temporal envelope of the XUV pulse is calculated by taking the square of the Fourier transform along the spectral axis in Fig. 5.3 and averaging over the spatial coordinate. Note that this value is larger than the Fourier-limited pulse duration of 8 fs due to a nonlinear chirp that is introduced by the lens. When increasing the peak gas density to $1.1 \times 10^{20}\ \text{atoms}/\text{cm}^3$ (corresponding to a focal length of 90 cm), we predict a moderate stretching from 24 fs to 29 fs. Focusing of shorter XUV pulses may be achieved by combining a refractive lens with another focusing element. For example, the development of a multi-component lens consisting of an XUV refractive lens and a Fresnel zone plate was suggested [100, 101]. It was theoretically shown that these multi-component lenses can be used to focus broadband attosecond pulses to nanometer spot sizes [101], which may enable the investigation of electronic processes with attosecond temporal and nanometer spatial resolution.

5.3 Conclusion and Outlook

In conclusion, we have presented a method to deflect and focus XUV pulses by exploiting the inhomogeneity of a gas jet placed in the way of an XUV beam. Our results enable the transfer of concepts based on refractive optics that are widely used in other spectral regions to the XUV regime, including microscopy, nanofocusing and the compression of ultrashort pulses. XUV gas-based lenses have several advantages, including their high transmission, formability and tunability (by varying the gas composition, the gas pressure and the gas jet geometry). Compared with reflective mirrors that are often used to focus XUV pulses, these XUV lenses are immune to damage (because the gas sample is constantly

replenished) and preserve the propagation direction of the incoming XUV light, thereby facilitating their use in experimental setups.

Refractive XUV gas-phase lenses can be designed for photon energies between 10 eV and 24 eV by carefully selecting appropriate atoms or molecules for different photon energies. Above the ionization potential of the neutral medium, the transparency of the gaseous medium is reduced due to ionization. A gas lens in the vicinity of the Xe 4d giant dipole resonance [120] would be interesting for applications of EUV lithography at its current design wavelength (13.5 nm [121]). However, a first experiment to achieve an XUV prism using the Xe 4d giant dipole resonance did not yield a positive result, due to the large absorption in the vicinity of the Xe 4d ionization edge. In the future, this limitation could be lifted, by developing lenses that exploit refraction in an inhomogeneous plasma consisting of highly charged ions and electrons.

While we have so-far emphasized the refraction of XUV pulses as a result of the static refractive index of the gas medium, the method may be extended to study and exploit transient refractive index changes in the XUV regime. As a first proof-of-principle of this time-resolved measurement, the temporal build-up of the resonant shape of the refractivity was measured in a He gas-phase prism by perturbing the free induction decay (FID) of the He 1s2p resonance with a time-delayed NIR pulse. The measured angular-resolved spectrum is shown in Fig. 5.5: The XUV refraction of the He 1s2p resonance in the absence of a NIR pulse or with a NIR pulse preceding the excitation by the XUV attosecond pulse by 500 fs is shown in Fig. 5.5(a) and (b). At temporal overlap, much of the XUV radiation in the vicinity of the resonance is absorbed (Fig. 5.5(c)), due to the NIR-mediated coupling to nearby states or the continuum (cf. Chapter 6). At a time-delay of 200 fs (Fig. 5.5(d)), the refracted signals close to the resonance are suppressed and a characteristic fringe modulation due to the perturbed induction decay (cf. Chapter 2) is visible. At an even later perturbation by the NIR pulse (4 ps delay, Fig. 5.5(e)) most of the refracted resonance is visible and only the contributions at highest refraction angles are missing. The results show, that a perturbative NIR pulse can be used to time-dependently control the refractivity around an atomic resonance.

The theoretical tools to calculate attosecond transient refractive index changes are already developed through the efforts of describing transient absorption spectroscopy, as it has been done in Chapter 2, since the change of refractive index and absorption correspond to the real and imaginary part of the ratio of the complex dipole spectrum and the incident electric field, respectively.

5 Extreme-ultraviolet Refractive Optics

This is in contrast to attosecond transient absorption spectroscopy, where the change of refractive index is lost, since an incoherent measurement (represented in Eq. 2.6 by taking the absolute square of the spectral field) of the spectral intensity before and after interaction is made. The gas-phase prism, however, intriguingly allows to simultaneously observe the effect of refraction and absorption in a single experiment.

In linear spectroscopy, the change of refractive index and the absorption coefficient are related by the Kramers-Kronig formula, meaning they obey:

$$\Delta n(\omega) = \frac{c}{\pi} \text{P.V.} \int_0^{\infty} \frac{\omega' \alpha(\omega')}{\omega'^2 - \omega^2} d\omega', \quad (5.7)$$

where P.V. indicates that the integral is a Cauchy principle value integral.

A similar Kramers-Kronig relation can be found, for the transient dipole spectrum if:

$$\begin{aligned} \text{Re } d(\omega) &= -\mathcal{H}(\text{Im } d(\omega)) \\ \text{Im } d(\omega) &= \mathcal{H}(\text{Re } d(\omega)), \end{aligned} \quad (5.8)$$

where \mathcal{H} is the Hilbert transform:

$$\mathcal{H}(f)(x) = \frac{1}{\pi} \text{P.V.} \int_{-\infty}^{\infty} \frac{f(y)}{x-y} dy. \quad (5.9)$$

This relation holds if the time-domain representation $d(t) = \vartheta(t)f(t)$, where $\vartheta(t)$ is the Heaviside function. We will see in Chapter 7.2 that this condition is fulfilled, if the initial excitation by the XUV pulse can be approximated as impulsive, i.e. with a Dirac-delta function. This approximation implies that a causal excitation of ATAS is considered, e.g. where the NIR pulse can not alter population prior of the arrival of the XUV pulse. A similar consideration of an impulsive excitation and causality requirement to reconstruct the time-dependent dipole from the measured ATAS signal was recently done by V. Stooß *et al.* [122]. The existence of this Kramers-Kronig relation allows to additionally utilize the combined measurement of transient refraction spectroscopy and transient absorption spectroscopy to increase the fidelity of the experimental measurement. At the same time, it allows the reconstruction of the full complex spectral dipole or time-dependent dipole, without relying on Kramers-Kronig relations or an impulsive excitation. However, a robust method to extract the real part of the spectral dipole from the experimentally obtained angle-resolved spectra is needed. While we have relied on a central-weight method to estimate the refractive index from the observed angular deflections (e.g. in

Fig. 5.2), more complex structures, as presented in Fig. 5.5, where both absorption and refraction need to be considered, require careful numerical analysis. The same is true for measurements at reduced gas pressures, which might be required for combined absorption and refraction experiments at higher photon energies (e.g. above the ionization potential). One such method could be an inversion of the Kirchhoff-diffraction equation (Eq. 5.5) by a phase-retrieval algorithm, as often applied to similar problems in e.g. FROG-CRAB [123], which we hope to develop in the future.

For solid-state materials, time-resolved reflection spectroscopy has recently been used to measure the complex spectral dipole [124, 125]. A transient dipole spectroscopy can be seen as the complementary method for materials in the gas-phase, where the lack of a defined interface hinders the application of time-resolved reflection spectroscopy.

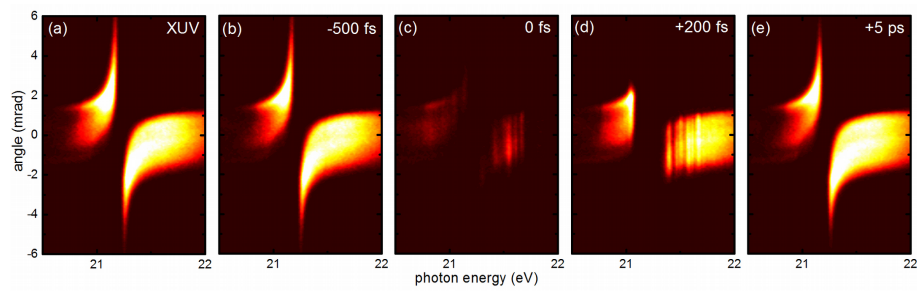


Figure 5.5: Time-Dependent Refraction. **a**, Angle-resolved XUV spectrum around the He 1s2p resonance after crossing a 1 mm diameter gas jet 0.3 mm below its center at an estimated peak density of 5×10^{19} atoms/cm³. XUV radiation from HHG in Xe is deflected upwards below the resonant energy (21.22 eV) and downwards above due to the refractive index and the gas-phase prism effect. **b** When applying an additional NIR pulse ($I \sim 5 \times 10^{12}$ W/cm²) long before the XUV pulse arrives, the angle-resolved XUV spectrum remains unperturbed. **c** At temporal overlap, the XUV spectra are strongly absorbed. **d,e** At a time-delay after XUV excitation, the NIR pulse perturbs the build-up of the refraction feature.

Chapter 6

6 XUV Spectral Compression by Four-Wave-Mixing

As mentioned in Chapter 1, XUV sources often have characteristic spectral bandwidths that might not fit the needs of the desired XUV application. We have already seen that ATAS requires broad XUV spectra covering the spectral region of interest. Other applications can have different demands on the XUV bandwidth. To reiterate as a prime example, coherent diffractive imaging (CDI) can have very different demands on bandwidth depending on its specific usage: While an ultrashort pulse duration and therefore broad bandwidth is important for CDI studying the structure of biomolecules or nanotargets, where the imaging process needs to be faster than a possible light-induced destruction of the target (*diffract-and-destroy* [126]). On the other hand a narrow XUV bandwidth would increase the spatial resolution of CDI. EUV lithography [127] or time- and angle-resolved photoelectron spectroscopy [128–130] are further examples for applications demanding narrow spectral bandwidths.

Several methods have been developed to select narrowband XUV radiation from a broadband XUV spectrum, including the use of grating monochromators [131], multilayer mirrors [132] and opto-optical modulation [24]. These techniques, however, come at the cost of losing XUV flux by spatially or spectrally filtering photons that are outside of the spectral region of interest.

In this chapter, a novel concept for the efficient generation of narrowband XUV radiation that is based on the conversion of broadband attosecond pulses and few-cycle NIR pulses via a four-wave mixing process is presented. Efficient compression of broadband XUV radiation into a narrow bandwidth is achieved by exploiting the steep gradient of the frequency-dependent refractive index between two closely spaced resonances, while the nearly flat dispersion in the incident vacuum ultra-violet (VUV) and XUV regimes allows for a broadband

This chapter is based on an article currently in preparation. The author of this thesis performed the experiments in collaboration with B. Schütte and V. Shokeen, wrote the first draft and performed the perturbation theory calculations. M. Vrakking performed the numerical propagation calculations. Thanks to B. Schütte, M. Vrakking, O. Kornilov and V. Shokeen for contributing to the manuscript. Further thanks to M. Ivanov, M. Richter, F. Morales, A. Housaku and S. Patchkovskii for discussion.

phase-matching. The concept is demonstrated by focusing XUV pulses created by HHG into a dense krypton gas jet in the presence of a few-cycle NIR pulse. A narrow emission peak is observed between the Kr 6s and 4d resonances. The non-resonant nature and generality of the reported process offers intriguing opportunities for tailoring the spectral bandwidth of XUV beams.

6.1 Four-Wave Mixing and Phase-Matching at Double-Resonances

Spectral conversion by FWM in the XUV region near resonances has been extensively studied in the past (see e.g. Refs. [133–139]). In these FWM processes (see e.g. Ref. [135]) photons are absorbed at an energy ω_1 together with typically two IR photons and a photon is emitted at energy ω_2 , due to a third-order polarization response. The effective bandwidth of the absorbed and emitted radiation is thereby limited to the regions of the refractive index curve at ω_1 and ω_2 where phase-matching can be achieved. A novel phase-matching concept is presented in Fig. 6.1, where bandwidth compression is achieved by selecting spectral regions in which the slope of the frequency-dependent refractive index in the absorbing region $n(\omega_1)$ is shallow and in the emitting region $n(\omega_2)$ much steeper. This scheme allows to collect radiation at a broad range of wavelengths but confines the emission to a very narrow range, leading to a stark increase in spectral intensity at the emission wavelength. We have chosen Kr to demonstrate this concept in Fig. 6.1. The simultaneous absorption of one vacuum-ultraviolet (VUV¹) photon at around 9 eV and two NIR photons in a dense Kr gas results in the emission of a photon around 12.365 eV due to FWM. The slope of n at the emission energy of 12.365 eV is three orders of magnitude larger than the slope of n at the absorption energy of ~ 9 eV. Using the near-constant refractive index of Kr in the NIR ($n_{\text{NIR}} \lesssim 1.0004$ [140]), both regions can be phase-matched over a broad range of photon energies in the absorption region around 9 eV in the presence of a few-cycle IR pulse, $\Delta E \sim 1$ eV, but only for a narrow spectral bandwidth for the emission ($\Delta E \lesssim 2$ meV).

The behavior of the refractive index around 12.365 eV originates in its position between two neighboring resonances (the Kr 4d and 6s resonances): As described in Chapter 5, in the vicinity of a resonance the refractive index typically shows a strong increase ($n > 1$) approaching the resonance from the lower energy side followed by a quick drop to below unity at the resonance and a rise back towards unity above the resonance. In the case of the two neighboring

¹The notation VUV (<10 eV) and XUV (>10 eV) is used here to distinguish the incoming and outgoing radiation, but is in no means a general limitation on the described processes.

6.1 Four-Wave Mixing and Phase-Matching at Double-Resonances

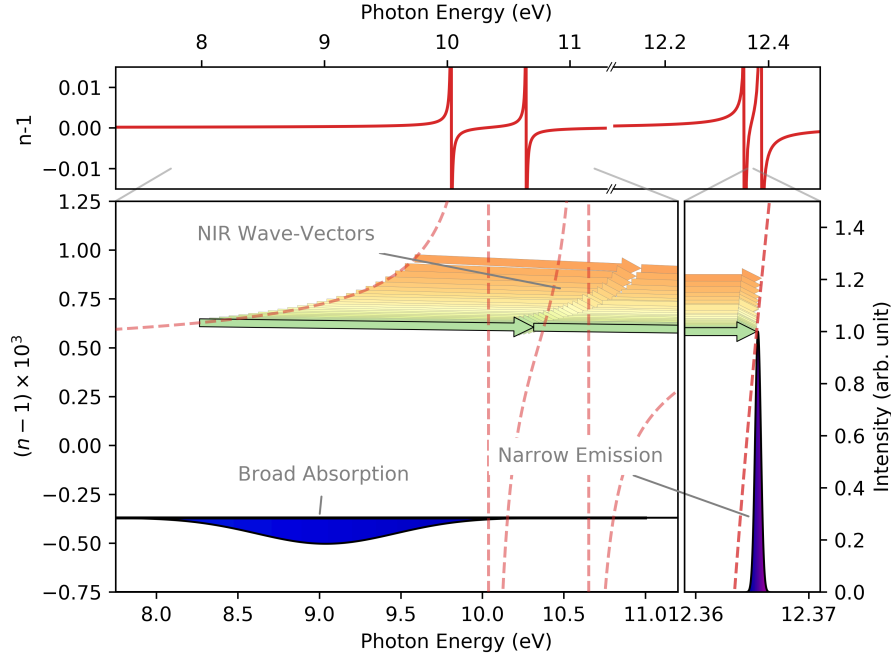


Figure 6.1: Bandwidth compression scheme in Kr: The extremely different slopes of the energy dependence of the refractive index n at the incident photon energy (~ 9 eV) and the emission energy (12.365 eV) allows phase-matching of a FWM process involving the absorption of two broadband NIR photons (colored arrows), generating XUV emission within a confined region ($\Delta E \lesssim 2$ meV) between the 4d and 6s resonances of Kr.

resonances, the refractive index varies extremely rapidly between the two resonances.

In this case the phase-matching condition:

$$\Delta k = n(\omega_{\text{XUV}}) \frac{\omega_{\text{XUV}}}{c} - n(\omega_{\text{VUV}}) \frac{\omega_{\text{VUV}}}{c} - 2n(\omega_{\text{NIR}}) \frac{\omega_{\text{NIR}}}{c} \ll \pi, \quad (6.1)$$

where $n(\omega)$ is the frequency-dependent refractive index at energy ω , can therefore only be fulfilled in a very narrow range of energies ω_{XUV} between the two resonances, whereas it can be satisfied for a broad range of photon energies ω_{VUV} , since the frequency dependence of $n(\omega_{\text{XUV}})$ is very steep and that of $n(\omega_{\text{VUV}})$ is shallow. Moreover, since between the two resonances the absorption cross section is small and the refractive index is close to unity, the FWM

process can be maintained at high pressure over a long propagation length, leading to a significant conversion efficiency at ω_{XUV} .

6.2 Experimental Demonstration of Bandwidth Compression

To demonstrate this concept in Kr experimentally, we make use of a gas-phase refraction prism, as described in Chapter 5. The experiments have been performed at the Attosecond Beamline, as described in Chapter 3. Short NIR pulses of 4.5 fs pulse duration (FWHM), centered around 800 nm wavelength, were used to generate high harmonics in Xe. Fig. 6.2(a) shows the angle-resolved XUV spectrum in the spectral region between 11 eV and 14 eV as recorded on the spectrometer. The broad harmonic spectrum is expected to extend below 11 eV, however due to technical constraints, the lowest photon energy detectable by the spectrometer setup was 11 eV. In Fig. 6.2(b) we show the spectrogram after the broadband XUV pulse passes 0.3 mm away from the center of the Kr gas jet. A thin In filter (100 nm) was inserted after the HHG (see Chapter 3), to ensure that this measurement was not influenced by the co-propagating residual NIR pulse from the HHG process. We note that this spectrum qualitatively is the same with and without the In filter. The peak number density is estimated to be $5 \times 10^{19}/\text{cm}^3$, corresponding to a fifth of the backing pressure at a temperature of 300 K (see Chapter 5). After passing through a region with a gas density gradient, the spectral components near resonances are deflected proportional to the value of the refractive index at this wavelength. The spectral range shown in Fig. 6.2 is centered around the $(^2P_{3/2})4d$ (12.355 eV) and $(^2P_{3/2})6s$ (12.385 eV) resonances [141]. As can be seen from the inset, in between the resonances the refractive index has a very steep slope and passes through $n = 1$, leading to a narrow undeflected feature between the two resonances.

When the In filter is removed and a moderately intense ($I \approx 1 \times 10^{12} \text{ W/cm}^2$) NIR pulse is temporally overlapped with the XUV pulses, an intense emission feature is observed (as shown in Fig. 6.2(b)) at the photon energy of the previously observed undeflected spectral component in Fig. 6.2(a), with a width of 26 meV, which is limited by the spectrometer resolution. A large fraction of the incoming XUV radiation at different energies is absorbed, due to the IR-induced coupling of excited states to other states and ionization continua [142]. This emission feature is not observed, when the In filter is present. To compare the spectral intensities of both measurements, with and without the In filter, the intensity of the measurements with the In filter were scaled to be compa-

6.2 Experimental Demonstration of Bandwidth Compression

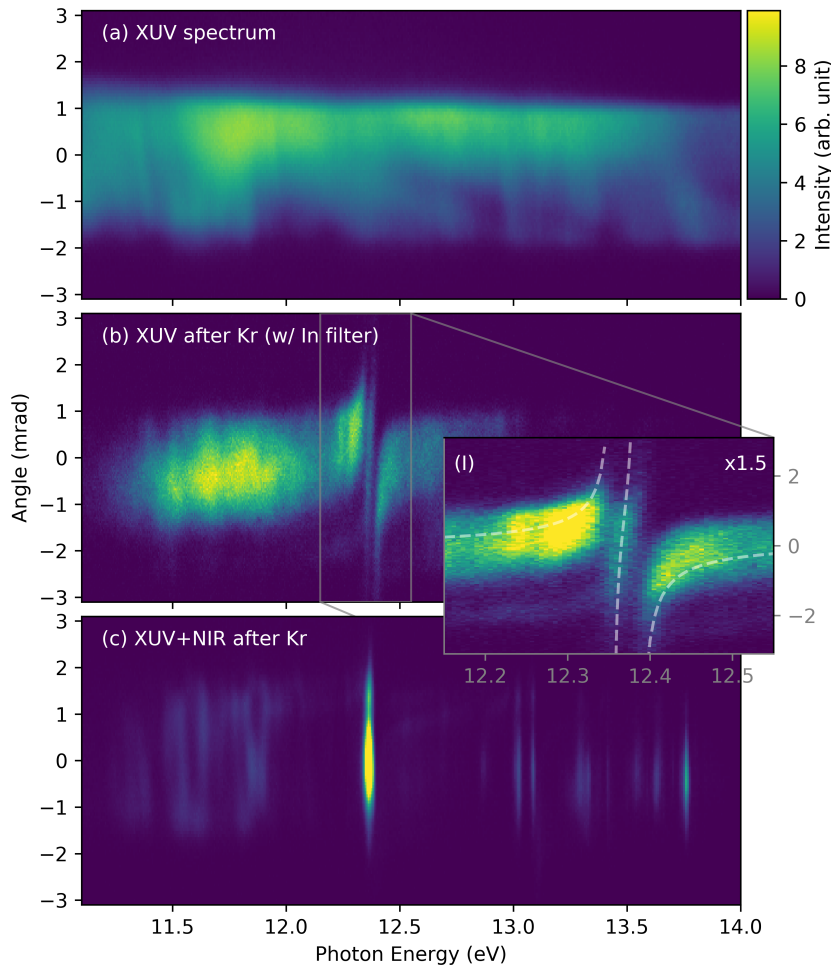


Figure 6.2: Experimental demonstration of FWM: a Angle-resolved XUV spectrum. **b** XUV spectrum (measured after transmission through an In filter) after propagation 0.3 mm below the center of a Kr gas jet ($\approx 3 \times 10^{19}$ atoms/cm³). The XUV spectra are deflected around the Kr resonances because of a wavefront rotation that results from the inhomogeneous transverse density profile (see Chapter 5). A narrow undeflected band can be seen between the 4d and 6s resonance (as indicated by the dashed white line in inset I). The location of this narrow feature is close to the photon energy where the XUV refractive index crosses unity. **b** In the presence of both XUV and NIR laser fields ($I \approx 1 \times 10^{12}$ W/cm²) a strong emission at the frequency of this narrow spectral band is observed.

6 XUV Spectral Compression by Four-Wave-Mixing

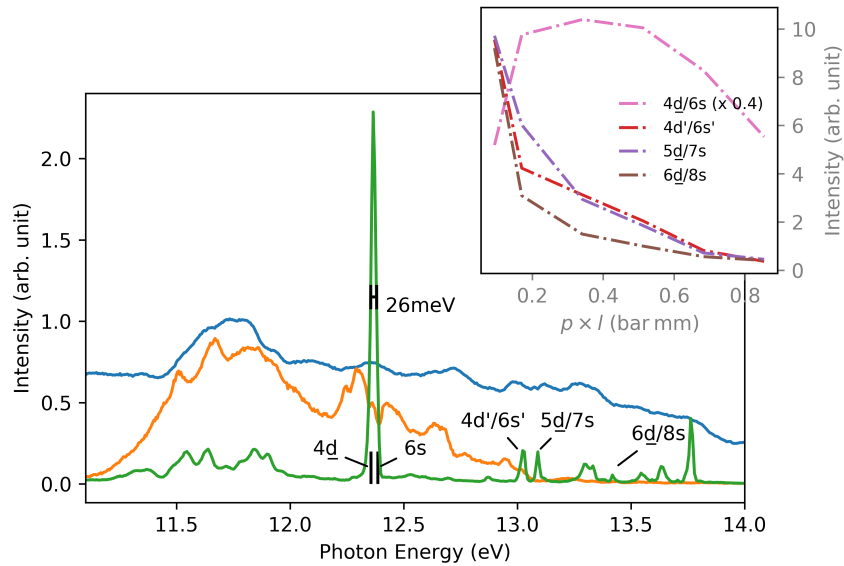


Figure 6.3: Spectral Intensity: Comparison of spectra integrated over an angular range between -3 mrad and $+3$ mrad. In the spectral range of the narrow-bandwidth feature, the signal intensity obtained after propagation through the gas jet, in the presence of the NIR pulse (green) exceeds the XUV intensity measured without gas jet (blue) or in absence of the NIR pulse (orange). The narrow feature has a spectrometer resolution-limited width of about 25 meV and a peak position of 12.365 ± 0.015 eV. Additional weak emission features are attributed to other resonances [141] and show a distinctively different dependence on the gas pressure (inset).

6.3 Perturbative Treatment of Third-Order Response

rable to those without, by relating the XUV spectra of both configurations in absence of the gas jet in the region of interest. Additionally, to exclude a pure NIR multiphoton process, we confirmed that no signal is observed at these NIR intensities in the absence of the XUV pulses.

Importantly, the measured spectral intensity at the emission feature significantly exceeds that of the incident XUV spectra at this photon energy, as expected from our bandwidth compression scheme.

Similar, but much weaker emission features at both lower and higher energies are observed, however their dependence on the gas pressure is distinctively different: Varying the pressure-length product of the Kr medium intersected by the XUV pulse (by varying the gas backing pressure) from $p \cdot l \approx 0.1$ bar mm to 0.9 bar mm (1.1 bar to 10 bar backing pressure), as shown in the inset of Fig. 6.3, a pronounced increase of the narrow-bandwidth feature is observed, with a maximum occurring at a pressure-length product of about 0.4 bar mm. In contrast, while the other observed emission features are of similar intensity at the minimal measured pressure-length product, they are rapidly suppressed with increasing pressure. This indicates that the phase-matching condition for bandwidth compression is not fulfilled for these states.

6.3 Perturbative Treatment of Third-Order Response

In order to further investigate the underlying conditions that lead to the observation of the emission features and their dependence on gas pressure, perturbation theory is used to calculate the third-order susceptibility for monochromatic waves in the atomic unit system as a sum over the excited states [48, 143]:

$$\chi^{(3)}(\omega) = \frac{N}{\epsilon_0} \sum_{abc} d_{ga} d_{ab} d_{bc} d_{cg} A_{abc}^{(3)} \quad (6.2)$$

where d_{nm} are the transition dipole moments, N is the number density, ϵ_0 the dielectric constant and

$$A_{abc}^{(3)} \approx \mathcal{P}_{ijk} \frac{1}{(\tilde{\omega}_{ag} - \omega_i - \omega_j - \omega_k)(\tilde{\omega}_{bg} - \omega_j - \omega_k)(\tilde{\omega}_{cg} - \omega_k)} \quad (6.3)$$

the frequency factors, with $\tilde{\omega}_{mn} = \omega_{mn} - i\Gamma$ being the field-free state energies with an added imaginary energy to account for their natural linewidth, and \mathcal{P} marking the sum over the permutations of the incoming waves ω_{VUV} and (twice) ω_{NIR} . The field-free state energies for a finite basis set of spin-orbit-free states up to an effective quantum number $n^* \leq 10$ are obtained from Ref. [144],

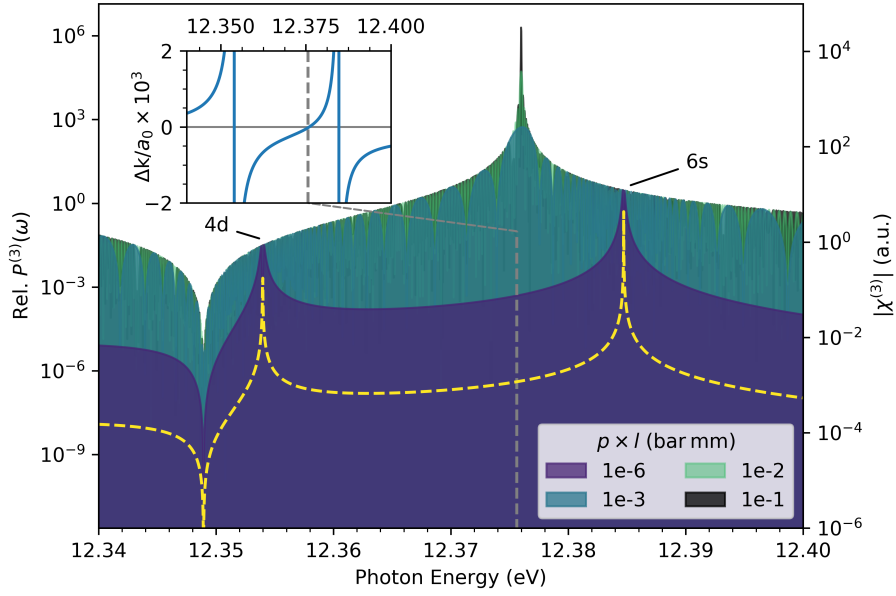


Figure 6.4: Polarization Response and Phase-Matching: The third-order susceptibility ($\chi^{(3)}(\omega_{XUV})$), dashed yellow line) of Kr in the vicinity of the 4d and 6s resonances and the zero-crossing of the wave-vector mismatch described by Eq. 6.1 (inset) allow for an effective FWM. For macroscopic pressure-length products, the narrow-bandwidth emission feature emerges in the relative third-order polarization response.

6.3 Perturbative Treatment of Third-Order Response

while the transition dipole moment matrix elements were calculated using standard angular momentum algebra and the method for evaluation the radial contribution to the matrix elements described in Ref. [145]. Since we assume the Kr atoms to be in the ground state, the counter-rotating terms are neglected. Due to conservation of energy $\omega = \omega_{VUV} + 2\omega_{NIR}$. Likewise for the phase-matching condition (Eq. 6.1), first-order perturbation theory is used to calculate the linear susceptibility [48]:

$$\chi^{(1)}(\omega) = \frac{N}{\epsilon_0} \sum_a \frac{d_{ag}d_{ga}}{\omega_{ag} - \omega}, \quad (6.4)$$

and the refractive index $n = \sqrt{1 + \chi^{(1)}(\omega)} \approx 1 + \frac{1}{2}\chi^{(1)}(\omega)$.

The polarization response of the FWM is calculated, which can be described for monochromatic plane-waves as [143]:

$$\frac{P^{(3)}(\omega_{XUV})}{P_{VUV}P_{NIR}^2} \propto |^2[\chi^{(3)}(\omega_{XUV})]^2 \text{sinc}\left(\frac{\Delta k(\omega_{XUV})l}{2}\right)^2, \quad (6.5)$$

where P_{VUV}, P_{NIR} are the respective monochromatic intensities, l the interaction length and $\chi^{(3)}(\omega_{XUV})$ and $\Delta k(\omega_{XUV})$ are the frequency- and (approximately linearly) pressure-dependent third-order susceptibility and wave-vector mismatch (see Eq. 6.1). The polarization response in vicinity of the 4d and 6s resonances is shown for different pressure-length products in Fig. 6.4 for a fixed NIR photon energy of 1.55 eV. For low pressure-length products ($p \cdot l \leq 10^{-6}$ bar mm) $P^{(3)}(\omega_{XUV})$ follows the third-order susceptibility (dashed yellow curve). For high pressure-length products ($p \cdot l \geq 10^{-1}$ bar mm), however, we observe the build-up of the narrowband emission at a spectral position that is determined by the wave-vector mismatch (inset in Fig. 6.4). The omission of spin-orbit coupling leads to a small energy shift of the narrow phase-matched region, when compared to the experimental results.

In contrast, the calculation for the region between the 5d and 7s resonance do not show this dependence, as shown in Fig. 6.5. While the third-order polarizability of these resonances is slightly stronger than of the 4d and 6s resonances, a strong wave-vector mismatch at 13.13 eV is observed (see inset of Fig. 6.4). It originates from the initial excitation of the 5s state by the VUV pulse and perturbs the phase-matching condition, explaining the absence of a narrow emission feature as observed between the 4d and 6s resonance. However, the formation of narrowband emission peaks at energies slightly below the 5d and 7s resonance are observed at higher pressure-length products in Fig. 6.5, which does not match the experimental observation. We note that varying the

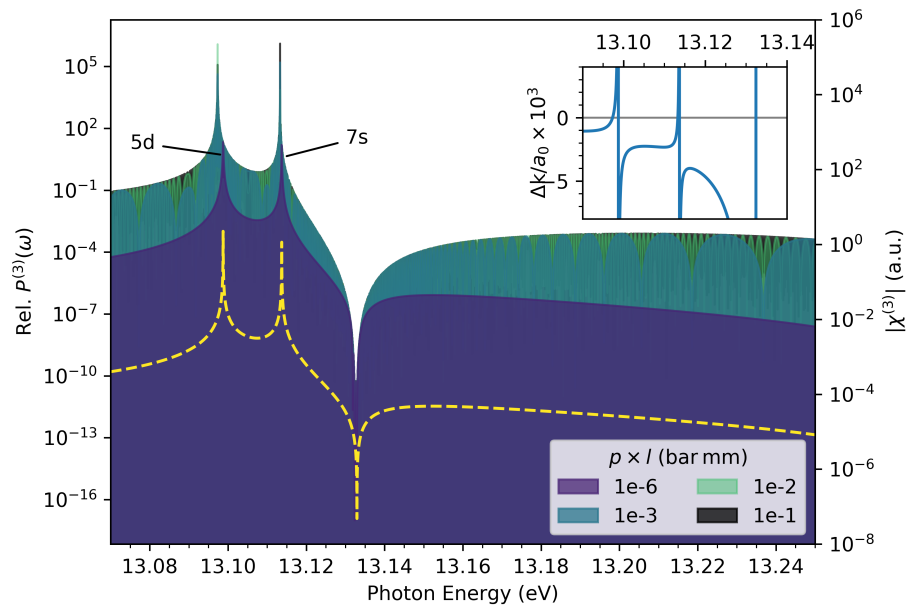


Figure 6.5: Polarization Response of 5d and 7s resonances: Although the third-order susceptibility ($\chi^{(3)}(\omega_{\text{XUV}})$), dashed yellow line) of Kr in the vicinity of the 5d and 7s resonances is similar to the 4d and 6s resonance (see Fig. 6.4) no build-up of a narrowband feature in the polarization response is observed between them for higher pressure-length products. This might be due to the different wave-vector mismatch (inset).

IR energy in Eq. 6.5 shows a strong influence of the position of the narrowband emissions below the 5d and 7s resonance, while the narrowband emission between the 4d and 6s resonance is only weakly shifted in energy. This indicates that while there might be an efficient FWM-process leading to emission at energies below the resonances, it can be only efficient for monochromatic waves. In contrast the narrow feature between the neighboring 4d and 6s resonances allows for an efficient FWM with broadband pulses.

6.4 Coupled Time-Dependent Schrödinger and Maxwell Wave Equation Propagation

To fully model the propagation of the VUV and XUV field through the dense Kr gas jet in presence of the broad NIR pulses, we can apply our numerical model described in Chapter 2 using the finite basis set of spin-orbit-free states as above. However, as we expect from our experimental observation, that the spectral and temporal structure of the two-color field will be drastically changed during propagation, the Beer-Lambert approximation, which was made in Eq. 2.5, is no longer applicable. As such the coupled TDSE and MWE is solved for a one-dimensional gas jet, by forward-integrating the wave equation of Eq. 2.3 and solving the TDSE for $d(\omega)$ at every step using the two-color electric field obtained in the previous step².

After a windowed Fourier transform to account for limited spectral resolution, the dipole spectrum $\tilde{d}(\omega)$ was used to calculate the modification of the two-color laser field according to Eq. 2.3. The TDSE was integrated over 6400 NIR cycles (corresponding to about 17 ps), whereas the integration step during the propagation described by Eq. 2.3 was typically 10^6 a.u. at a gas pressure of 1 mbar. The input laser parameters are listed in Table 6.1. As in the experimental observation, we note that the result of the simulation is robust to variations in these parameters defining the XUV and IR pulses, as well as to the inclusion of single-photon ionization by the IR laser (using ionization rates calculated for Ar using the TDSE code described in Ref. [146]).

In Fig. 6.6(a), we show the XUV spectrum after propagation of the two-color laser field using a pressure-length product $p \cdot l = 0.3$ bar mm. In agreement with the experimental findings, a strong and narrow emission feature is observed between the 4d and 6s resonance with a bandwidth of ≈ 2 meV (FWHM).

To estimate the efficiency of the spectral narrowing, the peak spectral intensity of the XUV narrow-bandwidth feature and bandwidth is compared to the

²As previously mentioned, these numerical calculations were performed by M. Vrakking.

Table 6.1: Laser Parameters for Numerical Simulation

Parameter	NIR-Pulse	XUV-Pulse
Central Frequency	1.55 eV	10.85 eV
Pulse Duration (FWHM)	15.0 fs ^a	400 as ^b
Peak Field Intensity	9×10^{11} W/cm ²	3.51×10^{10} W/cm ²

^a Sine-squared Pulse Envelope^b Gaussian Pulse Envelope

average spectral intensity in the VUV region of interest (≈ 9.27 eV) and the available two-photon NIR bandwidth. The 15 fs NIR-pulse with central frequency of 1.55 eV corresponds to a bandwidth of at least 0.14 eV. Although a sine-squared envelope was used in the calculations, we will estimate the two-photon bandwidth by convolution of two Gaussian distributions of this bandwidth. The estimated two-photon bandwidth is then $\Delta E_{2\text{NIR}} = \sqrt{2} \cdot 0.14$ eV. The peak spectral intensity of the emission after a pressure-length product of 0.3 bar mm shows a 60-fold increase of spectral intensity compared to the incoming spectral intensity at $\omega_{\text{VUV}} \approx 9.27$ eV, while the spectral width is reduced by a factor 100, from ≈ 0.2 eV to ≈ 2 meV. This implies an efficiency of $\sim 60\%$.

This supports our interpretation of the process observed in the experimental data of Figure 6.2 and Figure 6.3 as a non-resonant FWM process, where VUV/XUV radiation around 9 eV (i.e. below the ($^2P_{3/2}$)5s excited state at 10.032 eV [141]) and the absorption of two NIR pulses, aided by the ($^2P_{3/2}$)5p excited states (between 11.3 eV and 11.7 eV), lead to a third-order polarization response at a photon energy between the 4d and 6s excited states. Indeed, exclusion of any of these states in the TDSE quenches the observation of the emission feature. A further confirmation of the non-resonant nature of the observed process is the delay-dependence of the observed feature: Varying the delay between the XUV and NIR pulses, the experiment and the simulations show a fast reduction of the observed feature within the cross-correlation of the two pulses.

Fig. 6.6(b) depicts XUV spectra calculated by solving the TDSE and the Maxwell propagation as a function of the pressure-length product of Kr, showing rapid extinction of other emission features after short propagation lengths due to imperfect phase-matching and absorption. The observed reduction of the narrowband emission at high pressures/propagation lengths is attributed to the depletion of the VUV spectral power at $\omega_{\text{VUV}} = 9$ eV to 9.5 eV and absorption of the XUV emission. Within this presented model, the limiting factor for the conversion is the incoming VUV flux. Practically there are also limitations

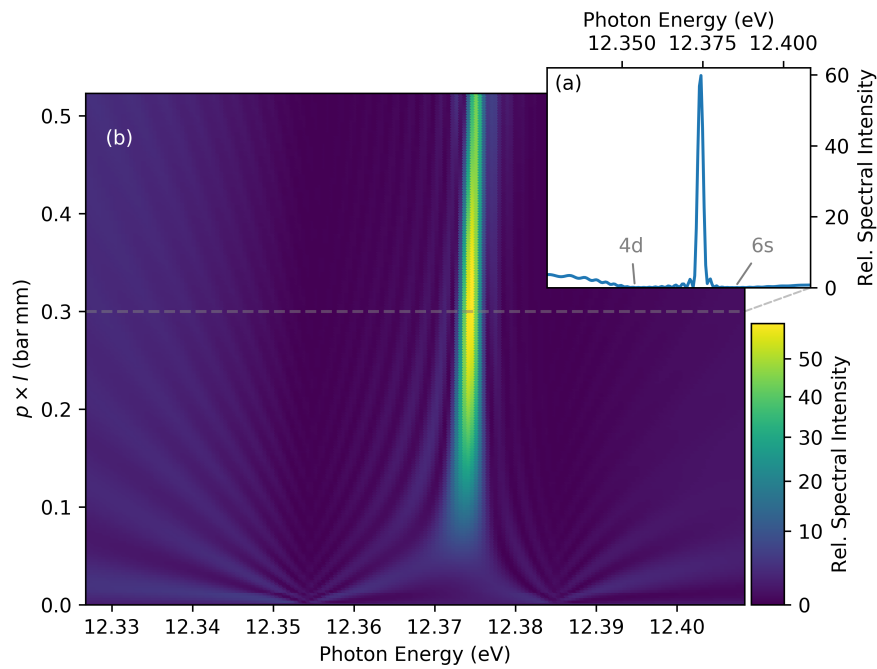


Figure 6.6: Simulated propagation dependent FWM signal of the narrowband feature: **a** XUV spectra after co-propagation with an NIR pulse through a one-dimensional Kr gas using coupled TDSE and Maxwell propagation equations. As in the experiment, a narrow-bandwidth emission feature at 12.37 eV is observed between the strongly absorbing 4d and 6s resonances. **b** The simulated XUV spectral intensity at different propagation depths through the medium. While at early propagation depths a broad emission between the two resonances can be seen, the bandwidth quickly narrows. A similar saturation region as in the experiment is observed.

on the propagation length and gas density, as the temporal walk-off between VUV and NIR pulse needs to be limited and beam geometrical constraints need to be taken into account.

In contrast, in Fig. 6.7 we show the evolution of the XUV spectrum during the propagation through the jet for the spectral region around the 5d and 7s resonances. While the formation of an emission feature between the 5d and 7s resonances during the early propagation lengths can be seen (i.e. around 13.11 eV at a pressure-length product of below 0.1 bar mm), this emission feature is not observed at larger propagations. However, a broad, weaker emission area is observable at energies below the 5d resonance. This confirms our argument that the phase-matching condition between the 5d and 7s resonance can not be fulfilled at higher density-length products (in contrast to the region between 4d and 6s resonance) and that, while a FWM process below the 5d resonance is possible, the phase-matching condition does not lead to a narrowband feature for a broad NIR pulse.

6.5 Conclusion

In conclusion, we have presented the experimental observation of an efficient XUV spectral compression scheme, whereby broadband radiation from an attosecond pulse is converted into narrow bandwidth XUV radiation. The residual third-order susceptibility for XUV frequencies between two electronic resonances in Kr leads to a strong polarization response and to a narrow-bandwidth emission feature with high spectral flux. The presented theoretical models show, that a phase-matching condition enables this process to be efficient at high pressure-length products, before the generated spectrum is re-absorbed. In view of its dependence on the nature of the refractive index changes around resonances, the underlying phase-matching mechanism is expected to be applicable whenever such features can be found, i.e. in other atomic and molecular gases at different frequencies. The use of ion plasma gases could allow to extend this scheme into the high energy XUV or even soft X-ray ranges [147].

Although we have used the presented mechanism here to generate an intense narrowband emission feature at an XUV frequency, the non-resonant FWM additionally enables reversal of the process: Using intense, comparably narrow-band XUV pulses, e.g. from a seeded FEL source [44] or soft-X-ray laser [43], the presented scheme could be used to generate XUV pulses with a larger bandwidth. Our method thereby opens a way to compress XUV pulses to shorter durations, similar to hollow-core fiber compression in the visible regime.

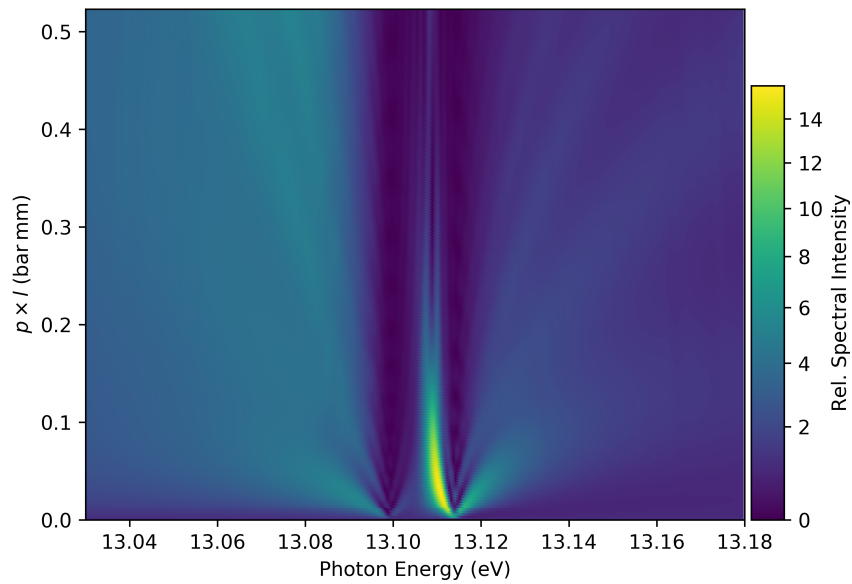


Figure 6.7: Simulated propagation dependent FWM signal near the Kr 5d and 7s resonances: XUV spectra after co-propagation with an NIR pulse through a one-dimensional Kr gas using coupled TDSE and Maxwell propagation equations. In line with the experimental observation, a narrowband emission feature in this spectral region is only observed during the early propagation. The formation of an efficient narrowband emission feature is not observed.

7 Chapter 7

The Time-Dependent Dipole of Non-Centrosymmetric Molecules

While the three state model, that we derived in Chapter 2 was sufficient to describe the phenomena we have discussed so far, it relied on an assumption, namely parity conservation. While it is an important guiding principle for recognizing the transitions that can occur in atoms, this is not longer the case in systems where the parity cannot be defined, i.e. systems that lack centrosymmetry, such as polar or chiral molecules. We will see that, when investigating these types of systems, two states can be coupled by both an odd or an even number of photons. In other words, excitation pathways in which the XUV pulse can coherently excite two states that can then be coupled via one or more IR photons need to be considered. A similar discussion has recently been done for polar molecules with a permanent dipole moment under consideration of only one excited state [148]. In this chapter we will discuss these additional pathways as follows: We will first apply our three state model to a He-like system that is non-centrosymmetric and present new spectral features that originate in the lowered symmetry. In the second part, an approximate analytical solution to the time-dependent dipole is presented using an adiabatic basis, which separates the fast dynamics of the XUV excitation from the slower dynamics of the IR induced coupling. The analytical description thereby offers further insight into the physical origins of the discussed features for both centrosymmetric and non-centrosymmetric systems. The new features of non-centrosymmetric ATAS offer novel opportunities to characterize polar and chiral molecules, as well as experimental parameters such as orientation and the carrier-to-envelope phase, as will be discussed in the third part.

This chapter is in parts based on an article currently in preparation. The author of this thesis performed the numerical calculations and the analytical derivation, wrote the first draft and coordinated communication. Thanks to M. Vrakking and J. Mikosch for contributing to the manuscript.

7.1 Discussion of Non-Centrosymmetric Attosecond Transient Absorption Spectroscopy

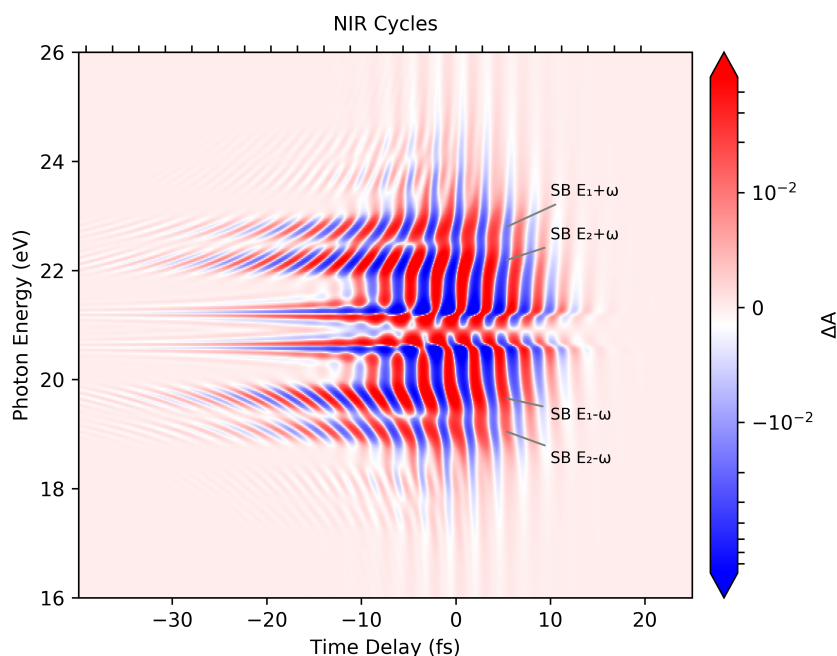


Figure 7.1: Attosecond Transient Absorption Spectrogram of the non-centrosymmetric problem calculated using the numerical solution of the three-level TDSE, once more using the energy levels of the He atom, but using selection rules that are applicable to a non-centrosymmetric system. The same parameters as in Fig. 2.1 are used, but the second excited state at E_2 can now be directly excited from the ground state. In the non-centrosymmetric case, the predominant features occur during overlap with the periodicity of the linear IR electric field.

To discuss the effect of these new excitation pathways, we repeat the numerical calculation from our example from Chapter 2. To reflect the lack of parity, the coupling between the ground state and the second excited state is now set to the same value as the coupling between the ground state and the first excited state ($d_{02} = d_{01}$). Repeating the calculation leads to the spectrogram shown in Fig. 7.1. In comparison with the previous spectrogram shown in Fig. 2.1, the same features are observed again, but a set of novel features can be seen, which oscillate as a function of XUV-IR delay-time with the periodicity of the IR field.

Two major new spectral features can be identified: The first is a pair of sidebands, similar to the ones discussed above, but appearing at energies corresponding to one IR photon above or below the field-free resonance energies of both excited states ($E_1 \pm \omega$ and $E_2 \pm \omega$ in Fig. 7.1). Analogous to the discussion of sidebands for the centrosymmetric case, these sidebands are assigned to excitation of a one-photon dressed state of either E_1 or E_2 by the absorption of an XUV photon accompanied by the absorption or emission of one IR photon. The fact that the E_1/E_2 state can be populated by a combination of both a one-color (XUV-only) and a two-color (XUV \pm IR) excitation process leads to the occurrence of an interference, which manifests in the form of a modulation of the sideband intensity as a function of XUV-IR time delay. Since only a single IR photon is now involved, this modulation occurs with the periodicity of the IR field, rather than twice its periodicity.

Similarly, the second novel feature that can be observed in Fig. 7.1 is a modification of the absorption strength directly at the resonance energies E_1 and E_2 . This is interpreted as an interference between two pathways leading to the excitation of the states, one directly from the ground-state with the absorption of a XUV photon and a second via an intermediate excitation of the other state in a two-photon (XUV \pm IR) process.

This assignment is not only supported by the modulation periodicity, but also by the same power-law analysis as in Chapter 2. In the non-centrosymmetric case, in contrast to the square-scaling in the symmetric case, the dominant features here scale linearly with the coupling matrix element and IR field strength.

This also explains the observed strength of the new features: Since in our choice of parameters the off-diagonal elements are much smaller than unity ($H_{12}(t, \tau) \ll 1$), features that depend linearly on the laser electric field strength and the coupling matrix element are much stronger than features that depend on the square of the laser electric field and the coupling matrix element.

7.2 Analytical Solution with Adiabatic Basis

To express the new features of non-centrosymmetric ATAS in approximate analytical form, the three-level time-dependent Schrödinger equation is analytically solved using an adiabatic basis. This is an extension of a similar approach reported by Rørstad *et al.* for the centrosymmetric case [51].

The analytical treatment uses the adiabatic basis:

$$|\Psi(t)\rangle = b_0(t)|\varphi_0\rangle + c_+(t)e^{i\theta_+}|\varphi_+(t)\rangle + c_-(t)e^{i\theta_-}|\varphi_-(t)\rangle, \quad (7.1)$$

with the dynamic phase $\theta_n = -\int_{\tau}^t E_n(t') dt'$.

7 The Time-Dependent Dipole of Non-Centrosymmetric Molecules

After the initial excitation from the ground-state by the XUV pulse, the IR-induced dynamics only involves the two excited states E_1 and E_2 , and we therefore consider the reduced two-level system:

$$H_r = \begin{bmatrix} E_R + \Delta & \Omega(t) \\ \Omega(t) & E_R - \Delta \end{bmatrix},$$

where $E_R = (E_1 + E_2)/2$, $\Delta = (E_1 - E_2)/2$ and $\Omega(t) = d_{12}\varepsilon_{IR}(t)$.

Upon diagonalization the time-dependent eigenenergies for the excited states are:

$$\begin{aligned} E_+ &= E_R + \sqrt{\Delta^2 + \Omega^2(t)}, \\ E_- &= E_R - \sqrt{\Delta^2 + \Omega^2(t)} \end{aligned}$$

with normalized adiabatic eigenstates:

$$\begin{aligned} |\varphi_+(t)\rangle &= \frac{\Delta + \sqrt{\Delta^2 + \Omega(t)^2}}{\sqrt{\Omega(t)^2 + (\Delta + \sqrt{\Delta^2 + \Omega(t)^2})^2}} |\Phi_1\rangle + \frac{\Omega(t)}{\sqrt{\Omega(t)^2 + (\Delta + \sqrt{\Delta^2 + \Omega(t)^2})^2}} |\Phi_2\rangle \\ &\doteq \cos \alpha(t) |\Phi_1\rangle + \sin \alpha(t) |\Phi_2\rangle \\ |\varphi_-(t)\rangle &= \frac{-\Omega(t)}{\sqrt{\Omega(t)^2 + (\Delta + \sqrt{\Delta^2 + \Omega(t)^2})^2}} |\Phi_1\rangle + \frac{\Delta + \sqrt{\Delta^2 + \Omega(t)^2}}{\sqrt{\Omega(t)^2 + (\Delta + \sqrt{\Delta^2 + \Omega(t)^2})^2}} |\Phi_2\rangle \\ &\doteq -\sin \alpha(t) |\Phi_1\rangle + \cos \alpha(t) |\Phi_2\rangle \end{aligned} \tag{7.2}$$

where Φ_n are the field-free excited states, and $\alpha(t)$ is a state mixing angle, given by:

$$\tan \alpha(t) = \frac{\Omega(t)}{\Delta + \sqrt{\Delta^2 + \Omega(t)^2}} \stackrel{\Omega \ll 1}{\approx} \frac{\Omega(t)}{2\Delta + \Omega(t)^2/(2\Delta)}. \tag{7.3}$$

Note that $\alpha(t)$ depends on the IR field strength and is thus a function of elapsed time t . For $\Omega(t) \rightarrow 0$ the mixing angle is 0 and $|\varphi_+\rangle$ and $|\varphi_-\rangle$ become $|\Phi_1\rangle$ and $|\Phi_2\rangle$, respectively.

To find the state-coefficients $c_+(t)$ and $c_-(t)$ of our adiabatic basis, the wavefunction is expressed in the field-free basis:

$$|\Psi(t)\rangle = b_0(t) |\Phi_0\rangle + b_1(t) |\Phi_1\rangle + b_2(t) |\Phi_2\rangle. \tag{7.4}$$

Combining Eq. 7.1 and Eq. 7.4 with Eq. 7.2 gives:

$$\begin{aligned} b_1(t) &= c_+(t)e^{i\theta_+} \cos \alpha(t) - c_-(t)e^{i\theta_-} \sin \alpha(t) \\ b_2(t) &= c_+(t)e^{i\theta_+} \sin \alpha(t) + c_-(t)e^{i\theta_-} \cos \alpha(t). \end{aligned} \quad (7.5)$$

To get the temporal dynamics of the excited state coefficients, the expression for the field-free wavefunction (Eq 7.4) is inserted into the time-dependent Schrödinger equation, leading to:

$$\begin{aligned} i\dot{b}_1 &= b_0 d_{01} \varepsilon_{XUV} + b_2 d_{12} \varepsilon_{IR} \\ i\dot{b}_2 &= b_0 d_{02} \varepsilon_{XUV} + b_1 d_{12} \varepsilon_{IR}. \end{aligned} \quad (7.6)$$

A perturbative approach is used to solve for the coefficients [149]: If the system remains unperturbed (zeroth-order), the entire population remains in the ground state: $b_0^{(0)}(t) = 1$, $b_1^{(0)}(t) = b_2^{(0)}(t) = 0$. To obtain the coefficients in first order, the zeroth-order wavefunction amplitudes are inserted into Eq. 7.6 and the set of equations is converted to a set of equations for the amplitudes in the adiabatic basis:

$$\begin{aligned} \dot{c}_+(t)e^{i\theta_+(t)} \cos \alpha(t) - \dot{c}_-(t)e^{i\theta_-(t)} \sin \alpha(t) &= -id_{01} \varepsilon_{XUV} \\ \dot{c}_+(t)e^{i\theta_+(t)} \sin \alpha(t) + \dot{c}_-(t)e^{i\theta_-(t)} \cos \alpha(t) &= -id_{02} \varepsilon_{XUV}, \end{aligned} \quad (7.7)$$

solving for $\dot{c}_\pm^{(1)}(t)$ gives:

$$\begin{aligned} \dot{c}_+^{(1)}(t) &= -i\varepsilon_{XUV}e^{-i\theta_+(t)} (d_{01} \cos \alpha(t) + d_{02} \sin \alpha(t)) \\ \dot{c}_-^{(1)}(t) &= +i\varepsilon_{XUV}e^{-i\theta_-(t)} (d_{01} \sin \alpha(t) - d_{02} \cos \alpha(t)). \end{aligned} \quad (7.8)$$

Assuming that the initial excitation of the XUV pulses is sufficiently short with respect to the IR-induced dynamics, it can be approximated by a Dirac δ function [23, 51]: $\varepsilon_{XUV}(t) \rightarrow I_0 \delta(t - \tau)$, and $c_\pm^{(1)}(t)$ can be obtained by direct integration:

$$\begin{aligned} c_+^{(1)}(t) &= \int_\tau^t \dot{c}_+^{(1)}(t') dt' \\ &= -i\vartheta(t - \tau) (d_{01} \cos \alpha(\tau) + d_{02} \sin \alpha(\tau)) \\ c_-^{(1)}(t) &= \int_\tau^t \dot{c}_-^{(1)}(t') dt' \\ &= i\vartheta(t - \tau) (d_{01} \sin \alpha(\tau) - d_{02} \cos \alpha(\tau)), \end{aligned} \quad (7.9)$$

where $\vartheta(t)$ is the Heaviside function. Note that in these expressions the state-mixing angle, which defines the relation between the adiabatic eigenstates and

7 The Time-Dependent Dipole of Non-Centrosymmetric Molecules

the field-free eigenstates, is no longer a function of t , but a function of the XUV-IR delay τ .

Ultimately, we are interested in the time-dependent dipole expressed in terms of the field-free basis, which can be written as:

$$\begin{aligned}\langle d(t) \rangle &= d_{01} b_1(t) + d_{02} b_2(t) + c.c. \\ &= d_{01} [c_+(t) e^{i\theta_+} \cos \alpha(t) - c_-(t) e^{i\theta_-} \sin \alpha(t)] \\ &\quad + d_{02} [c_+(t) e^{i\theta_+} \sin \alpha(t) + c_-(t) e^{i\theta_-} \cos \alpha(t)] + c.c.\end{aligned}\quad (7.10)$$

As it was the case for the TDSE, $\langle d(t) \rangle$ is real valued and therefore the Fourier transformation will be Hermitian. Since the spectral response has been defined for positive frequencies in Eq. 2.12, we make the choice, for ease of notation, to only keep terms that correspond to features at positive frequencies after the Fourier transformation, which, as it will be clear in a moment, are the complex conjugated terms.

In the present derivation, the time dependence of the dynamic phase term has so far been ignored. Inserting the time-dependent energy of the adiabatic states into Eq. 7.1 allows to rewrite the state-dependent exponential term as:

$$\begin{aligned}e^{i\theta_{\pm}} + c.c. &= e^{-i \int_{\tau}^t E_{0\pm} \sqrt{\Delta^2 + \Omega^2(t')} dt'} + c.c. \\ &\approx e^{-i(E_{0\pm} \Delta)(t-\tau)} e^{\mp i\varphi(t,\tau)} + c.c.,\end{aligned}\quad (7.11)$$

where the fast oscillating terms $e^{-i(E_{0\pm} \Delta)(t-\tau)} + c.c.$, i.e. the field-free resonant energies of the excited states, lead to a resonant frequency response at $E_0 \pm \Delta$ in the complex conjugate (in contrast to a frequency response at $-(E_0 \pm \Delta)$ in the non-conjugated term of Eq. 7.11). $\varphi(t, \tau)$ is the so called light-induced phase (LIP) caused by the AC Stark effect (see Chapter 2), which can be approximated for small IR intensities ($\Omega(t) \ll 1$):

$$\varphi(t, \tau) \approx \frac{1}{2\Delta} \int_{\tau}^t \Omega^2(t') dt'. \quad (7.12)$$

If the light-induced phase is assumed to be a constant function of time, one can easily transform the time-dependent dipole to the spectral domain, by adding an imaginary energy $i\Gamma/2$ to the energy eigenvalues to account for the decay of the excited states:

$$\begin{aligned}\mathcal{F}[d(t)_{\text{LIP}}](\omega) &\propto \mathcal{F}[i\theta(t-\tau) e^{-\frac{\Gamma}{2}(t-\tau)} e^{i(E_{0\pm} \Delta)(t-\tau)} e^{\pm i\varphi}] \\ &= e^{-i\pi(E_{0\pm} \Delta)} \frac{ie^{\pm i\varphi}}{\sqrt{2\pi}(\frac{\Gamma}{2} + i(\omega - (E_0 \pm \Delta)))}.\end{aligned}\quad (7.13)$$

The spectral response can then be obtained as the superposition of a symmetric (e.g. Lorentzian) and a dispersive (e.g. Fano-like) lineshape, as discussed by Ott *et al.* [29]:

$$\begin{aligned}
 S(\omega) &\propto \text{Im}[d(\omega)_{\text{LIP}} \varepsilon_{\text{XUV}}^*(\omega)] \propto \text{Re} \left[\frac{e^{\pm i\varphi}}{\sqrt{2\pi} \left(\frac{\Gamma}{2} + i(\omega - (E_0 \pm \Delta)) \right)} \right] \\
 &= \cos \pm \varphi \frac{\frac{\Gamma}{2}}{\sqrt{2\pi} \left[\frac{\Gamma^2}{4} + (\omega - (E_0 \pm \Delta))^2 \right]} \\
 &\quad - \sin \pm \varphi \frac{\omega - (E_0 \pm \Delta)}{\sqrt{2\pi} \left[\frac{\Gamma^2}{4} + (\omega - (E_0 \pm \Delta))^2 \right]}
 \end{aligned} \tag{7.14}$$

Note that we have ignored the fast oscillating $e^{-i\tau(E_0 \pm \Delta)}$ term in Eq. 7.14. It will lead to the hyperbolic converging lines $e^{i\tau(\omega - E_0 \pm \Delta)}$ due to the multiplication with $\varepsilon_{\text{XUV}}(\omega)^* \propto e^{i\omega\tau}$.

The approximation of the LIP as being independent of time delay, however, neglects effects due to the XUV-IR delay and the time-dependence of the integral in Eq. 7.12. For certain forms of the electric field an analytical solution to Eq. 7.12 can be found using special functions (e.g. the error function for Gaussian pulses). Alternatively the exponential integral in Eq. 7.11 can be approximated using a stationary phase approximation and a series expansion using the Jacobi-Anger identity [150], as it is often done in the similar problem of strong-field photoelectron streaking [151]. A discussion of a parametrized approximation to the LIP can be found in Appendix C.

Inserting Eq. 7.11 and Eq. 7.9 into Eq. 7.10 and keeping only the complex conjugated terms, the full time-dependent dipole can be written in a compact form using an index notation:

$$\begin{aligned}
 d(t) &= i\vartheta(t - \tau) e^{-\frac{\Gamma}{2}(t-\tau)} \sum_{n \neq m}^{1,2} e^{(-1)^n i\varphi(t,\tau)} \\
 &\quad \left[\begin{aligned}
 &-d_{0n}^2 e^{iE_n(t-\tau)} \cos \alpha(\tau) \cos \alpha(t) \\
 &-d_{0n}^2 e^{iE_m(t-\tau)} \sin \alpha(\tau) \sin \alpha(t) \\
 &+ (-1)^n d_{01} d_{02} e^{iE_n(t-\tau)} (\sin \alpha(\tau) \cos \alpha(t) + \sin \alpha(t) \cos \alpha(\tau))
 \end{aligned} \right].
 \end{aligned} \tag{7.15}$$

In Fig. 7.2(a), we show the ATAS spectrogram resulting from the analytical Eq. 7.15, for the centrosymmetric case (setting $d_{02} = 0$) and in Fig. 7.2(b) the

7 The Time-Dependent Dipole of Non-Centrosymmetric Molecules

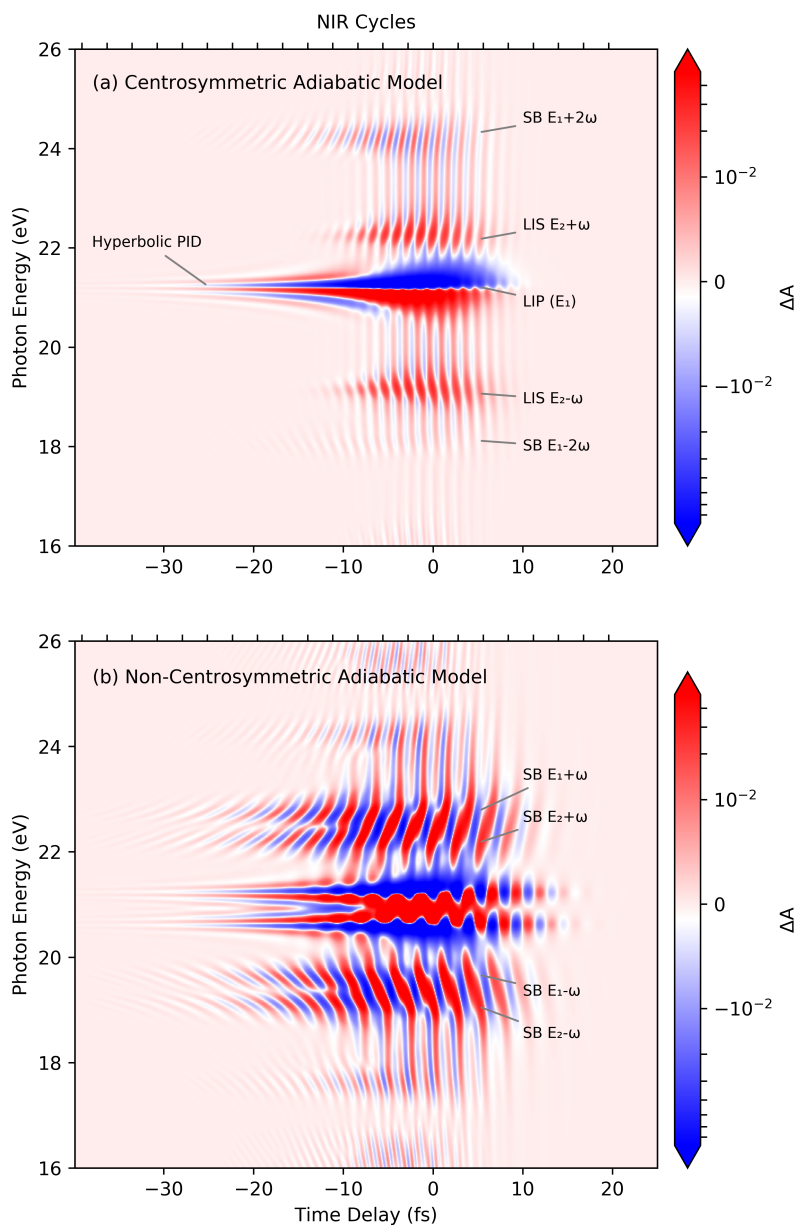


Figure 7.2: Analytical Solution of the Adiabatic Approximation to the a centrosymmetric and b non-centrosymmetric Helium three-level problem. The time-dependent dipole has been solved by numerical integration of the light-induced phase integral and transformed to the spectral domain using FFT. In comparison to the fully-numerical solutions (cf. Fig. 2.1 and Fig. 7.1), the adiabatic analytical solution shows stronger contributions at higher order sidebands and an increased effect of the light-induced phase.

non-symmetric case using the same parameters as in the previous section and numerically solving the light-induced phase integral and the Fourier transformation. The adiabatic system reproduces the numerical solution of the three-level TDSE to a good degree. However, by comparing the strength of the reshaping of the resonance lineshape during XUV-IR overlap in Fig. 2.1 and Fig. 7.2(a), the contribution of the light-induced phase seems to be too large in comparison with the full numerical solution, most likely due to our approximation of the adiabatic eigenenergy in Eq. 7.11.

The time-domain representation of the dipole moment allows for a physical interpretation of our result. Eq. 7.15 contains two sets of contributing terms: The first set is purely dependent on the transition dipole moment connecting the ground state to one of the excited states, while the second set depends on the product of the matrix elements $d_{01}d_{02}$. Both type of terms show a different time evolution depending on the IR induced state-mixing at the time of excitation by the XUV pulse (described by $\alpha(\tau)$) and during the subsequent evolution (described by $\alpha(t)$). Clearly, in the case of a system that follows the Laporte rule (i.e. a centrosymmetric system), the second set of terms vanishes ($d_{01}d_{02} = 0$).

It is very interesting to inspect the two terms more closely and evaluate their different time-evolution: Recalling that the mixing-angle terms originate from the projections of the adiabatic states onto the field-free states (cf. Eq 7.2), the leading term containing both $\alpha(t)$ and $\alpha(\tau)$ can be interpreted as an IR-dependent projection from the field-free onto the adiabatic evolving states at the time of the XUV excitation ($\cos \alpha(\tau)$), and then back to the field-free states after the interaction with the IR field ($\cos \alpha(t)$), while the term containing $\sin \alpha(\tau) \sin \alpha(t)$ describes a projection from each of the field-free states onto the other adiabatically evolving state and then back again to the original field-free state. It additionally becomes apparent, that this term can only contribute to the absorption signal, if there is overlap between the XUV and the IR pulse ($\alpha(\tau) \neq 0$). In contrast, in the second set of terms that depend on the product of the matrix elements $d_{01}d_{02}$, i.e. the coherent excitation of both excited states by the XUV possible in the non-centrosymmetric case, the mixing-angle terms can be interpreted as a transfer from one field-free state to the other via an intermediate adiabatic mixing state ($\sin \alpha(\tau) \cos \alpha(t)$ and $\cos \alpha(\tau) \sin \alpha(t)$).

To explore the effects of the discussed mixing-angle terms in the transient absorption spectrum (i.e. after transformation to the spectral domain, Eq. 2.12), they are expanded in the strength of the IR-induced coupling ($\Omega(t) = d_{12}\epsilon_{IR}(t)$),

7 The Time-Dependent Dipole of Non-Centrosymmetric Molecules

up to second-order:

$$\begin{aligned}\cos \alpha(t) &= 1 - \frac{\Omega^2(t)}{8\Delta^2} + O(\Omega^4) \\ \sin \alpha(t) &= \frac{\Omega(t)}{2\Delta} + O(\Omega^3)\end{aligned}\tag{7.16}$$

The time-dependent terms get transformed into the spectral domain by the Fourier transform, leading to the formation of sidebands, where the order of the sideband is given by the order of the dependence on Ω in the expression of $d(t)$ (upon application of Eq. 7.16). Assuming a monochromatic wave, the Fourier transform of $\Omega(t)$ is:

$$\begin{aligned}\mathcal{F}[\Omega(t)](\omega) &\propto \mathcal{F}[d_{12}\cos\omega_{IR}t](\omega) \\ &= \sqrt{\frac{\pi}{2}}d_{12}(\delta(\omega - \omega_{IR}) + \delta(\omega + \omega_{IR})).\end{aligned}\tag{7.17}$$

Since the IR pulse is generally not monochromatic, these side-bands will be broadened by a convolution of their pulse spectral envelope with the natural linewidth. The same series expansion can be done for the XUV-IR delay dependent terms $\cos \alpha(\tau)$ and $\sin \alpha(\tau)$ by substituting the time t with τ in Eq. 7.16. Since the τ -dependent terms are not affected by the Fourier transformation, they will lead to a modulation of the absorbance signals with the delay between IR and XUV pulse. An analytical solution to the Fourier transformation of the mixing-angle contributions can be found in Appendix B.

It is worth noting, that this shows, that the IR field is affecting the observed ATAS in two very distinct ways: On the one hand, the appearance of a sideband signal depends on the instantaneous, sub-cycle field strength of the IR field at the time of the excitation, on the other hand the spectral form of the sideband is dependent on the oscillating behavior of the IR field over multiple cycles.

As shown in Eq 7.15, the state-mixing terms contribute to $d(t)$ in four combinations and each contribution to the resulting spectrogram is shown in Fig. 7.3. As discussed by Rørstad *et al.* [51] and identified in the previous section, the $\cos \alpha(\tau) \cos \alpha(t)$ term will lead to fringes displaced by $\pm 2\omega_{IR}$ from the energies of the (bright-state-)resonance energies and a delay-dependent modulation at twice the IR-field frequency (Fig. 7.3(a)), while the leading constant in the series expansion of $\cos \alpha(t)$ (Eq. 7.16) leads to a strong LIP effect on the resonance absorption line. The $\sin \alpha(\tau) \sin \alpha(t)$ term on the other hand will lead to sidebands displaced by $\pm\omega_{IR}$ with respect to the resonance energies. These are the previously discussed light-induced structures and their dependence on $\sin \alpha(\tau)$ explains their observation only at delays where XUV and IR overlap (Fig. 7.3(b)).

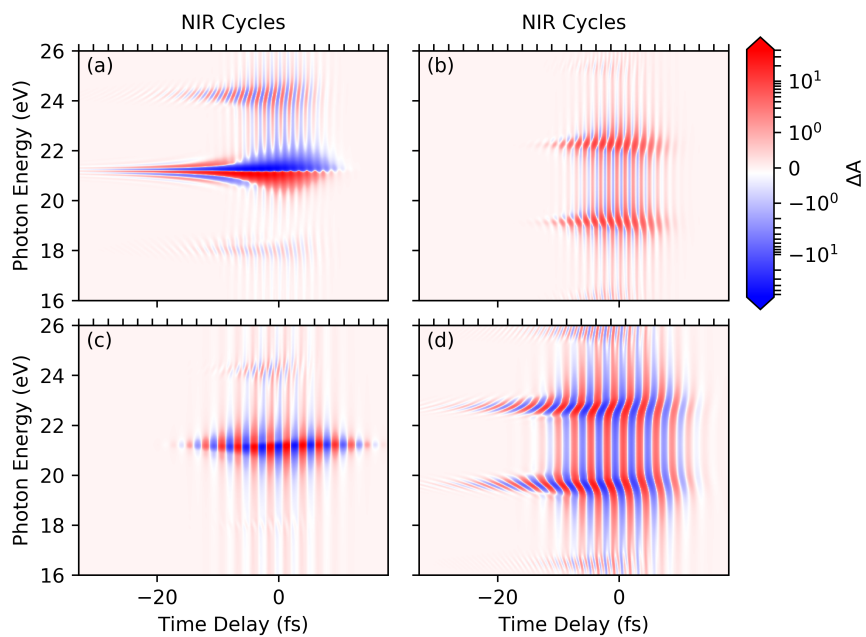


Figure 7.3: Separate Contributions of the Mixing Angle Terms from the adiabatic solution of the Helium-like three-level problem (only shown for the E_1 resonance): **a** Light-induced phase effect, with additional fringe side-bands at $\pm 2\omega$ energies, **b** light-induced structure, **c** modulation of the main absorption by the instantaneous electric field at the XUV excitation and **d** new light-induced fringe sidebands due to a one IR-photon-dressed absorption resonance.

While it appears that here the $\sin \alpha(\tau)$ term should lead to a linear ($1\omega_{IR}$) modulation of the LIS, the delay-dependent interference between the XUV field and the dipole moment leads to a hyperbolic term after Fourier transformation [23, 51], which at the observable side-band $|E_2 \pm \omega| \approx \omega_{IR}$ combines to the observed $2\omega_{IR}$ modulation (see Appendix B.3 for a detailed derivation).

In contrast, in the new non-centrosymmetric terms, due to the term $\sin \alpha(\tau) \cos \alpha(t)$, the linear modulation in delay by the sine term remains at the field-free resonance energy: While the $\Omega^2(t)$ term in the expansion of $\cos \alpha(t)$ leads to sidebands displaced by $2\omega_{IR}$ from the resonance energy, analogous to their formation in the symmetric case, the dominant leading constant in the expansion leads to absorption at the resonance, which is now modulated by $\varepsilon_{IR}(\tau)$ due to the expansion of $\sin \alpha(\tau)$ (shown in Fig. 7.3(c)). This means the IR electric field is sampled by the delay dependent modulation of the field-free resonance energies E_1 and E_2 , enabling the direct reconstruction of the IR pulse.

Lastly, the $\cos \alpha(\tau) \sin \alpha(t)$ term leads to the sidebands displaced by $\pm\omega_{IR}$. Here, a modulation of the sideband with delay by $\varepsilon_{IR}^2(\tau)$ would be expected, resulting in oscillations at the periodicity $2\omega_{IR}$, due to the expansion of $\cos \alpha(\tau)$. However, similarly to the previous argument for the light induced structure, the hyperbolic interference condition with the XUV field leads to a predominant modulation at $1\omega_{IR}$ periodicity (Fig. 7.3(d)).

7.3 Observability of Non-Centrosymmetric Features

As shown, additional coupling pathways in the non-centrosymmetric problem lead to new features in ATAS within the single molecule response. The discussion that has been presented so far is relevant within a frame of reference fixed to the molecule (molecular frame). However, to observe these features experimentally, the centrosymmetry also needs to be broken in the frame of reference where the experimental observation is made (i.e. in the laboratory frame). A discussion on how to calculate the effects of orientational averaging in the laboratory frame is presented in Appendix A as an extension to the numerical model from the beginning of this Chapter, but for now it is enough to consider the effect when, from the laboratory frame, we find an equal amount of molecules oriented in one direction and oriented in the inverse direction: Since in our model we can consider the transition dipole moment d_{12} as the projection of the three-dimensional dipole moment onto the IR laser polarization axis, such an inversion of the molecule will lead to an inversion of the sign of Ω . It is clear from Eq. 7.2 that the terms depending on $\sin \alpha$ will change sign when the sign of Ω changes, while the terms depending on $\cos \alpha$ will re-

7.3 Observability of Non-Centrosymmetric Features

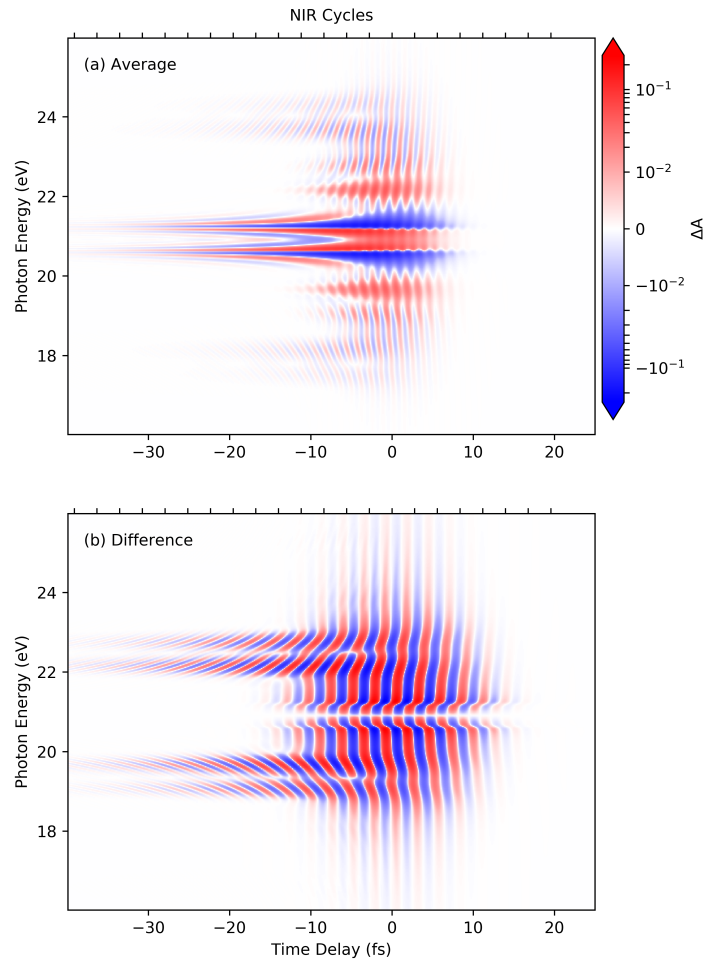


Figure 7.4: Effect of CEP control on non-centrosymmetric ATAS features: **a** shows the sum of two ATAS spectrograms calculated for opposite CEP (0 and π) of the IR pulse, exhibiting only the non-periodic- and hyperbolic-, as well as features that oscillate with an even multiple of the IR frequency, similar to the centrosymmetric case. **b** shows the difference between the two spectrograms, enhancing the novel features that oscillate at the frequency of the IR laser field. Note that the identical result is obtained, when the orientation is controlled instead of the CEP.

main unchanged under inversion of Ω . This means, that the contributions from the non-centrosymmetric terms will cancel out unless the probed ensemble is oriented along the IR laser polarization axis in the laboratory frame. Laser-induced orientation of neutral molecules is an active research topic [152–154], and is challenging at the gas pressures required by current experimental setups for ATAS. However, naturally oriented condensed media, such as thin-films or bulk crystalline samples could be used [155].

Similar aspects need to be considered for the sign of the electric field: Changing the CEP of the IR laser pulse by π leads to inversion of the linear electric field and therefore $\Omega(t)$. If the CEP is not stabilized, the contribution of the non-symmetric signal will quickly average out.

In Fig. 7.4 the effect of controlling the CEP is shown: In Fig. 7.4(a) the sum of two simulations solving the TDSE for the non-symmetric case at opposite CEP of the IR pulse (0 and π) is shown (at a fixed orientation). The averaged ATAS resembles the centrosymmetric case, however both excited states are coupled to the ground state and contribute without distinction between bright and dark state to the spectrogram. However, by controlling the CEP value, the non-symmetric signal contrast can be maximized: In Fig. 7.4(b) we show the difference of two spectrograms taken at the opposite CEP values. Since here the even-terms cancel out in the difference, and only the $1\omega_{IR}$ -oscillating features from the non-symmetric solutions remain. While we have calculated the presented cases in Fig. 7.4 by varying the CEP, the same analysis can be done for the orientation of the molecule. Assuming an even distribution of molecules oriented parallel and antiparallel to the laser polarization axis, the observed ATAS corresponds to Fig. 7.4(a). If however the difference is calculated of one measurement with all molecules oriented parallel and one with all molecules oriented antiparallel to the laser polarization axis, the resulting difference of ATAS corresponds to Fig. 7.4(b).

We have encountered the situation of such an averaged measurement already before: While CH_3I is a non-centrosymmetric polar molecule, no indication of the corresponding non-centrosymmetric features have been found in the experimental data in Chapter 4. This is not unexpected, since neither were the molecules oriented in the laboratory frame of the experiment, nor was the CEP of the laser pulses stabilized. However, those restrictions can be lifted in the numerical simulations based on the *ab-initio* results¹. If the calculation is performed for a fixed orientation and CEP, the spectra exhibit the non-centrosymmetric features, i.e. a modulation of lineshape in delay with the NIR electric field. Anal-

¹In fact and as noted in Chapter 4, the results shown in Fig. 4.2 had to be explicitly averaged in orientation and CEP to reproduce the experimental findings.

7.3 Observability of Non-Centrosymmetric Features

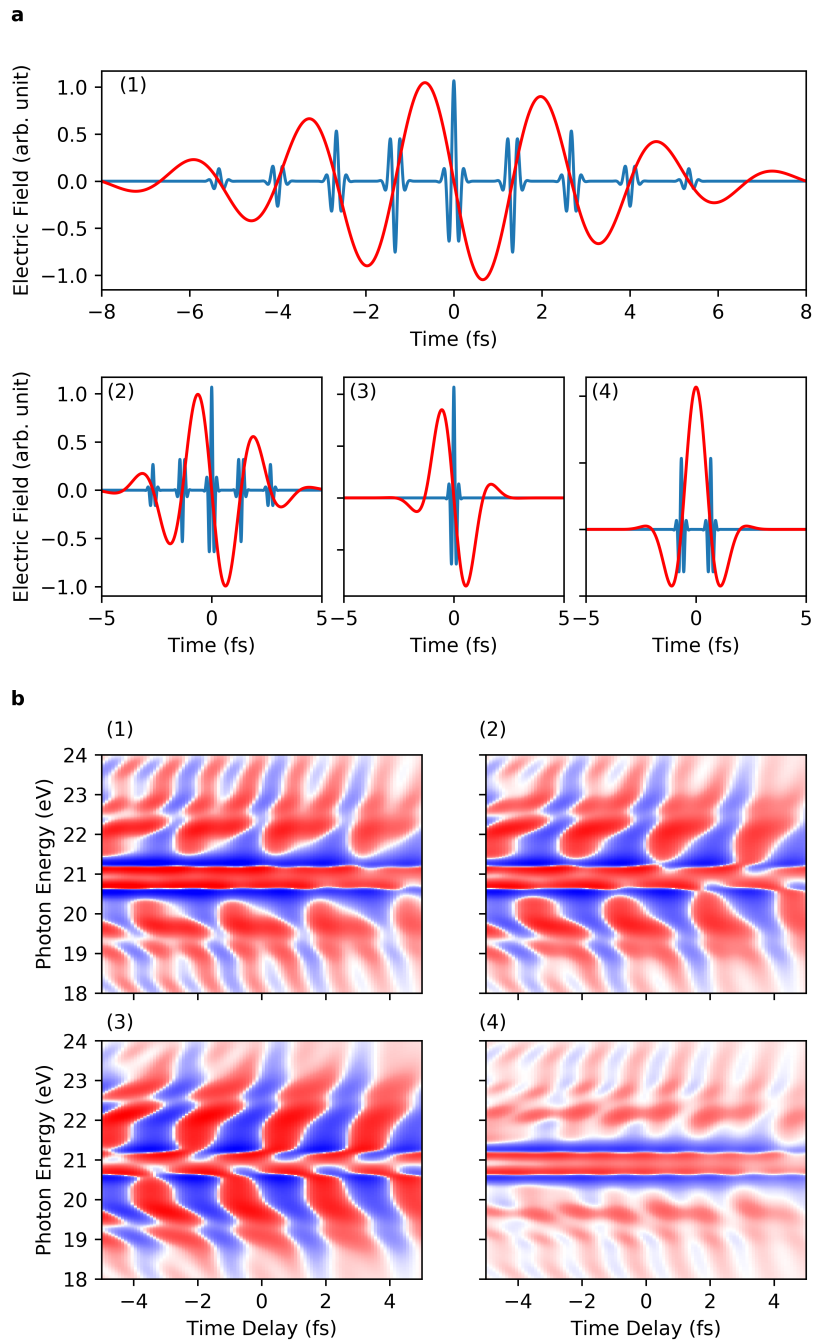


Figure 7.5: Sensitivity on Attosecond Pulse Structure on non-centrosymmetric ATAS features: **a**(1-4) sketch of the phase relation of driving field and consecutive attosecond bursts. **b**(1-4) ATAS from numerical simulation using the respective XUV attosecond pulse structure of a(1-4). Note that the same IR pulse is used for each ATAS.

ysis of the *ab-initio* transition dipole moments shows that one-photon transitions between *bright* states with I $4d_{5/2}^{-1}$ - and I $4d_{3/2}^{-1}$ -configuration exist, indicating a deformation of the iodine 4d-core orbitals due to the molecular environment. The transition dipole moments of these spin-orbit split transitions are two to three orders of magnitude smaller than the transitions between the Rydberg states belonging to the same spin-orbit configuration of the core-hole discussed in Chapter 4. This implies that they did not significantly contribute to the observed signals of the orientation-averaged experiment. However, due to the linear scaling of the non-centrosymmetric features, we anticipate that they should be reproducible in an ATAS experiment with oriented CH₃I molecules and CEP stabilized laser pulses.

The dependence of the observed signal on the CEP has implications for the dependence on the XUV pulse as well: In HHG, the emitted attosecond bursts are locked to the phase of the driving field and in an attosecond pulse train generated from HHG (in atoms) the individual pulses are spaced by half the driving field period and the CEP of consecutive attosecond pulses changes by π [8]. This is shown in Fig. 7.5a(1), where we sketch the APT of a few-cycle driving field. As can be seen, the (absolute) maximum of the XUV field (blue) changes from a positive to a negative peak and vice versa in consecutive pulses of the pulse train as a consequence of the CEP of the individual attosecond pulses. However, the ATAS is unaffected by this inversion of the XUV pulses: While the dipole spectrum $d(\omega)$ is odd under the inversion of the XUV excitation field, the observable spectral response is even because of the multiplication with the XUV spectrum (see Eq. 2.12). Since however the sign of the direct IR field is also inverted for every half cycle, this implies, that the non-centrosymmetric signal is highly sensitive to the structure of attosecond pulses used for the XUV excitation. In Fig. 7.5a(1-4) we show sketched attosecond pulse trains associated to different driving pulse lengths. In Fig. 7.5b(1-4) we show the ATAS that results from the respective APT (1,2,4) or IAP (3). Note that while we changed the XUV pulse structure, we used the same IR pulse for all spectrograms in Fig. 7.5b. As can be seen, the ATAS signal changes when the attosecond pulse becomes isolated. Therefore the observation of these signals could be used as an indicator of contrast for isolated attosecond pulses.

To conclude, we have shown that additional coupling pathways in non-centrosymmetric systems lead to new spectroscopic features in transient absorption spectroscopy due to breaking of the Laporte rule. Using an adiabatic basis set, we have derived an (approximate) analytical solution of the time-dependent dipole, which shows the origin of different features of ATAS due to the light-induced phase and adiabatic state-mixing. We have also shown, that

7.3 Observability of Non-Centrosymmetric Features

the observability of these signals depends on orientation of the molecular frame in the laboratory frame. This limitation gives the opportunity to characterize molecular orientation by all-optical means. The modification of the absorption line by the electric field during excitation allows for a characterization of the used IR pulses in-situ, by extracting the delay-dependence of the transient absorption at the resonance energy of the excited states. The periodic half-cycle dependence on the electric field gives an indication of the pulse-to-pulse contrast in short attosecond pulse trains. Since the non-symmetric features depend linearly on the transition dipole moment and the IR field, it not only can be a more sensitive probe than the symmetric ATAS signal in weakly coupled systems, but also at lower IR field intensities.

The linear dependence on the transition dipole moment of the excited states adds an important implication of the application of ATAS for chiral systems: Recently, the existence of a photo-excited circular dichroism (PXCD) has been described [156] by the existence of a pseudo-scalar triple product $[\vec{d}_{01} \times \vec{d}_{02}] \cdot \vec{d}_{12}$, where \vec{d}_{nm} are the transition dipole matrix elements in three dimensions. The enantiomers then differ by the inversion of their wavefunction $\Psi_L(r) = \Psi_R(-r)$, which leads to $\vec{d}_L = -\vec{d}_R$. Comparing Eq 7.15, we can see that $d(t)$ is indifferent to the inversion of the transition dipole moments from the ground state d_{01} and d_{02} , but the linear dependence on d_{12} leads to a change of sign of the non-symmetric contributions to the ATAS when changing from the L- to R-stereoisomer, enabling the determination of stereoisomeric excess from the contrast of the described linearly dependent features of the non-centrosymmetric ATAS.

Lastly the strict symmetry argument depending on the lack of centrosymmetry creates an intriguing opportunity to study ultrafast changes in the electronic symmetry. Centrosymmetry-sensitive transient absorption could hereby be used as a complementary probe to observe charge localization during dissociation [157] or photon-induced symmetry breaking [158].

8 Chapter 8

8 Summary

In this thesis, different methods to study the dipole interaction of atoms and molecules with ultrashort XUV pulses on attosecond timescales were presented. We have shown the theoretical methods to investigate the time-dependent dipole in a phase-controlled two-color NIR and XUV field, based on few-level numerical methods and an analytic adiabatic approximation. The resulting observable spectral signals have been discussed for attosecond transient absorption spectroscopy in a three-level system and their physical origin has been examined. Hereby we especially considered new coupling pathways that arise in non-centrosymmetric molecules. Although challenging to be observed experimentally, the new spectroscopic features that arise from the new coupling pathways allow deeper insight into the light-induced couplings of e.g. polar and chiral molecules than their centrosymmetric counterparts, since they potentially allow the reconstruction of the full transition dipole moment and NIR electric field instead of the squared dipole moment and NIR field that is contained in centrosymmetric ATAS.

ATAS has been used in an experimental study to probe the state-resolved polarizability of iodomethane. The different coupling strengths and polarizabilities of the core-to-valence and core-to-Rydberg states could thereby be revealed, demonstrating the viability of ATAS in polyatomic molecules and at core-level transitions, where it can act as a local probe with excellent temporal and spectral resolution. The gained knowledge of the bilinear dependence of the spectral features observed in ATAS allows to apply factorization algorithms such as the presented singular value decomposition to independently analyze the spectral and temporal components of different spectral features, while increasing the signal-to-noise ratio.

Furthermore, we have investigated the refraction of XUV light and developed an XUV prism through the interaction of XUV light with an inhomogeneous gas jet. This allows the measurement of the refractive index in the XUV spectral region. The combined measurement of refraction and absorption by the gas-phase prism allows for an attosecond transient dipole spectroscopy, using the same instrumentation typically used in an attosecond transient absorption spectroscopy setup. We have proposed a Kramers-Kronig relation that is derived from the solution to the time-dependent dipole that would allow the combined

8 Summary

measurement of refraction and absorption to provide redundant information for an increased fidelity of the measurement.

Together with a gas jet lens we have demonstrated the two most common refractive optical elements as a proof-of-principle of XUV refractive optics. The strong absorption of XUV light in many materials make it difficult to use the same optical elements that have been developed for light in different spectral regions. XUV gas-phase refractive optics provide a solution to this problem and we expect that they will emerge as an versatile tool to manipulate XUV light.

To spectrally manipulate XUV light, we have presented efficient XUV bandwidth compression using a novel phase-matching scheme to spectrally compress XUV light and increase spectral intensity by two to three orders of magnitude. The phase-matching scheme employs the rapidly varying refractive index between two closely spaced resonances to spectrally confine phase-matched four wave mixing in a spectrally narrow emission region, whereas a broad absorption region can be matched where the frequency-dependent refractive index is shallow. The efficient manipulation of XUV bandwidths to adapt the characteristic bandwidths of XUV lightsources to the demands of XUV applications promises greater versatility in the use of XUV light.

Revisiting the questions that were proposed in Chapter 1, we have shown that attosecond transient absorption spectroscopy reveals the sub-cycle light-induced modifications of the time-dependent dipole. We have seen, that the observed spectroscopic features depend on the squared value of the off-diagonal matrix elements of light-induced dynamics, i.e. the transition dipole moment and electric field. Within the dipole approximation, an initial electronic wavepacket of a photoexcitation is fully defined by the transition dipole moment and electric field, which shows the importance of knowing these properties for the understanding of purely electronic excitations. Applying Singular Value Decomposition to ATAS spectrograms allows to derive these values from the experimental data. The transition to core-excited states in molecular ATAS allows to view these light-induced couplings from the local point-of-view of reporter atoms, which will allow to study attosecond electronic dynamics in molecules with site-specificity. In the case of non-centrosymmetric molecules we have shown that the opportunity presents itself to even derive the full, complex-valued off-diagonal matrix element from ATAS.

The developed tools using the refraction of XUV light not only offers new possibilities in the design of XUV experiments, but the XUV prism furthermore in principle allows the reconstruction of the time-dependent dipole, giving new possibilities to study the electronic motion of molecules and the dynamic of the electronic degrees of freedom in the future.

A

Appendix A

Numerical Solution With Finite-Basis and Full Dimensionality

While the three-level numerical solution of the TDSE in one spatial dimension is a good model to understand the features that are observable in ATAS, it is often insufficient to describe real physical systems. Such systems might have multiple excited states that are closely spaced in the spectral region of interest and require an extension to a finite basis of states. A non-collinear polarization of laser pulses or a non-isotropic structure of the studied system (i.e. molecules) requires a three dimensional extension of the equations presented in Section 2.1. Both extensions are discussed together in this section.

For a three-dimensional molecule, the transition dipole moment is a tensor of rank three, which we can write in Cartesian coordinates (x, y, z) for the molecular fixed frame (MFF):

$$\vec{d}^{(\text{MFF})} = [d^x d^y d^z] \quad (\text{A.1})$$

To calculate the time-dependent dipole, the transition dipole moment is projected from the molecular fixed frame to the laboratory fixed frame (LFF) by the rotation matrix:

$$\begin{aligned} & \mathbf{R}(\alpha, \beta, \gamma) \\ &= \begin{pmatrix} \cos \alpha \cos \beta \cos \gamma - \sin \alpha \sin \gamma & -\cos \alpha \cos \beta \sin \gamma - \sin \alpha \cos \gamma & \cos \alpha \sin \beta \\ \sin \alpha \cos \beta \cos \gamma + \cos \alpha \sin \gamma & -\sin \alpha \cos \beta \sin \gamma + \cos \alpha \cos \gamma & \sin \alpha \sin \beta \\ \sin \alpha & \cos \beta & \sin \beta \sin \gamma \end{pmatrix}, \end{aligned} \quad (\text{A.2})$$

for a given orientation of the molecule with respect to the laboratory frame defined by the angles α, β, γ , so that:

$$d_{nm}^{\rightarrow (\text{LFF})} = \mathbf{R} \cdot d_{nm}^{\rightarrow (\text{MFF})}, \quad (\text{A.3})$$

Appendix A Numerical Solution With Finite-Basis and Full Dimensionality

where $d_{nm}^{\vec{}}$ is the three dimensional transition dipole matrix element from the transition dipole moment tensor.

The extension to a finite basis of states of Eq 2.8 and Eq 2.9 can simply be achieved by extending the Hamiltonian from Eq. 2.7 to the required finite set of n states and extending the corresponding indices. Eq. 2.9 can then be rewritten for each state amplitude c_n of the finite-basis:

$$i\dot{c}_n = \left[d_{0n}^{\vec{}} \text{ (LFF)} \cdot \vec{\epsilon}_{XUV}(t)e^{iE_n t} + \sum_{m \neq 0} d_{nm}^{\vec{}} \text{ (LFF)} \cdot \vec{\epsilon}_{IR}(t)e^{-i(E_n - E_m)t} \right] c_n, \quad (\text{A.4})$$

where $\vec{\epsilon}$ are the respective electric field vectors in the LFF. For example the IR pulse polarized along the X-axis (represented by unit vector \vec{e}_x) can be written as:

$$\vec{\epsilon}_{IR}(t) = \vec{e}_x \epsilon_{IR}(t). \quad (\text{A.5})$$

Subsequently, Eq. 2.10 is extended to

$$\langle \Psi(t) | \vec{d} | \Psi(t) \rangle = \sum_{n,m} c_n^*(t) c_m(t) d_{nm}^{\vec{}} \text{ (LFF)} e^{i(E_n - E_m)t}. \quad (\text{A.6})$$

and we can rewrite the response function (Eq 2.12) in terms of the scalar product of the vectorial spectral components:

$$S(\omega, \tau) = \text{Im} \left[\frac{\vec{d}(\omega) \cdot \vec{\epsilon}_{XUV}^*(\omega)}{|\epsilon_{XUV}|^2} \right], \quad \omega > 0. \quad (\text{A.7})$$

B

Appendix B

Spectral Solutions of the Adiabatic Approximation

To find the analytical solution of the Fourier transformation of the mixing-angle terms, the NIR electric field is approximated as monochromatic. As noted in Section 7.2, the solution can be extended to consider the spectrally broad NIR pulses by convolution the monochromatic solution with the NIR spectrum. The NIR electric field is approximated as:

$$\Omega(t) = d_{12}E_0 \cos(\omega_{IR}t), \quad (\text{B.1})$$

where E_0 is the field amplitude.

To find the Fourier transformation of the mixing-angle terms, the series expansion (Eq. 7.16) is used:

$$\begin{aligned} \sin \alpha(\tau) \sin \alpha(t) &\approx \frac{1}{4\Delta^2} \Omega(\tau)\Omega(t), \\ \sin \alpha(\tau) \cos \alpha(t) &\approx \frac{1}{2\Delta} \Omega(\tau) \left(1 - \frac{\Omega(t)^2}{8\Delta^2}\right), \\ \cos \alpha(\tau) \sin \alpha(t) &\approx \left(1 - \frac{\Omega(\tau)^2}{8\Delta^2}\right) \frac{1}{2\Delta} \Omega(t) \\ &= \frac{1}{2\Delta} \Omega(t) - \frac{1}{16\Delta^3} \Omega(t)\Omega(\tau)^2, \\ \cos \alpha(\tau) \cos \alpha(t) &\approx \left(1 - \frac{\Omega(\tau)^2}{8\Delta^2}\right) \left(1 - \frac{\Omega(t)^2}{8\Delta^2}\right) \\ &= 1 - \frac{\Omega(\tau)^2}{8\Delta^2} + \left(\frac{\Omega(\tau)^2}{8\Delta^2} - 1\right) \frac{\Omega(t)^2}{8\Delta^2}. \end{aligned} \quad (\text{B.2})$$

Appendix B Spectral Solutions of the Adiabatic Approximation

As discussed in Section 7.2, the time-dependent mixing-angle terms will lead to the generation of sidebands after Fourier-transformation:

$$\begin{aligned}
\mathcal{F}\left[\frac{1}{4\Delta^2}\Omega(\tau)\Omega(t)\right](\omega) &= \frac{1}{4\Delta^2}\mathcal{F}\left[d_{12}^2E_0^2\cos(\omega_{IR}\tau)\cos(\omega_{IR}t)\right](\omega) \\
&= \frac{1}{4\Delta^2}\cos(\omega_{IR}\tau)\sqrt{2\pi}d_{12}^2E_0^2\frac{\delta(\omega-\omega_{IR})+\delta(\omega+\omega_{IR})}{2} \\
\mathcal{F}\left[\Omega(t)^2\right](\omega) &= \mathcal{F}\left[d_{12}^2E_0^2\cos(\omega_{IR}t)^2\right](\omega) \\
&= \sqrt{2\pi}d_{12}^2E_0^2\left(\delta(\omega)+\frac{\delta(\omega-2\omega_{IR})+\delta(\omega+2\omega_{IR})}{2}\right)
\end{aligned} \tag{B.3}$$

The solution for the common terms of the full time-dependent dipole (Eq. 7.15) $\vartheta(t-\tau)e^{-\frac{\Gamma}{2}(t-\tau)}e^{iE_n(t-\tau)}e^{i\varphi}$ was already described in Eq. 7.13. To additionally include the effect of the mixing-angle terms, the convolution theorem is used [50]:

$$\mathcal{F}[f \cdot g](\omega) = \mathcal{F}[f](\omega) * \mathcal{F}[g](\omega), \tag{B.4}$$

where:

$$(f * g)(x) = \int_{-\infty}^{\infty} f(y)g(x-y) dy. \tag{B.5}$$

We will solve the mixing-angle components of the full time-dependent dipole separately as they appear in Fig. 7.3.

B.1 Centrosymmetric Terms

We consider the two terms contributing to the centrosymmetric signal, the sideband (SB) and light-induced structure (LIS) terms:

$$\begin{aligned}
d(t)_{\text{SYM-SB}} &= i\vartheta(t-\tau)e^{-\frac{\Gamma}{2}(t-\tau)}e^{i\varphi}d_{01}^2e^{i(E_n)(t-\tau)}\cos\alpha(\tau)\cos\alpha(t) \\
d(t)_{\text{SYM-LIS}} &= i\vartheta(t-\tau)e^{-\frac{\Gamma}{2}(t-\tau)}e^{i\varphi}d_{01}^2e^{i(E_n)(t-\tau)}\sin\alpha(\tau)\sin\alpha(t).
\end{aligned} \tag{B.6}$$

B.2 Non-Centrosymmetric Terms

Using the series expansion (Eq. 7.16) and sidebands (Eq. B.3), the spectral-domain representations of the centrosymmetric side-bands are:

$$\begin{aligned}
d(\omega)_{\text{SYM-SB}} &\approx \mathcal{F}[i\vartheta(t-\tau)e^{-\frac{\Gamma}{2}(t-\tau)}e^{iE_n(t-\tau)}e^{i\varphi}] * d_{01}^2 \mathcal{F}\left[\left(1 - \frac{\Omega(t)^2}{8\Delta^2}\right)\left(1 - \frac{\Omega(\tau)^2}{8\Delta^2}\right)\right] \\
&= \left[e^{-iE_n\tau} \frac{ie^{i\varphi}}{\sqrt{2\pi}\left(\frac{\Gamma}{2} + i(\omega - E_n)\right)} \right] \\
&\quad * d_{01}^2 \sqrt{\frac{\pi}{2}} \left[\left(\delta(\omega) - \frac{d_{12}^2 E_0^2}{16\Delta^2} (\delta(\omega) + \delta(\omega \pm 2\omega_{IR})) \right) \left(1 - \frac{d_{12}^2 E_0^2}{8\Delta^2} \cos(\omega_{IR}\tau)^2 \right) \right] \\
&= ie^{-iE_n\tau} e^{i\varphi} \left(1 - \frac{d_{12}^2 E_0^2}{8\Delta^2} \cos(\omega_{IR}\tau)^2 \right) \left[\frac{1}{2\left(\frac{\Gamma}{2} + i(\omega - E_n)\right)} \left(1 - \frac{d_{12}^2 E_0^2}{16\Delta^2} \right) \right. \\
&\quad \left. + \frac{d_{12}^2 E_0^2}{16\Delta^2} \frac{1}{2\left(\frac{\Gamma}{2} + i(\omega - E_n \pm 2\omega_{IR})\right)} \right]
\end{aligned} \tag{B.7}$$

where we have used the translational properties of the Dirac-delta function in convolutions.

Similar, the centrosymmetric light-induced structure is:

$$\begin{aligned}
d(\omega)_{\text{SYM-LIS}} &\approx \mathcal{F}[i\vartheta(t-\tau)e^{-\frac{\Gamma}{2}(t-\tau)}e^{iE_n(t-\tau)}e^{i\varphi}] * d_{01}^2 \mathcal{F}\left[\frac{1}{4\Delta^2}\Omega(\tau)\Omega(t)\right] \\
&= \left[e^{-iE_n\tau} \frac{ie^{i\varphi}}{\sqrt{2\pi}\left(\frac{\Gamma}{2} + i(\omega - E_n)\right)} \right] * \left[\frac{\sqrt{2\pi}d_{01}^2 d_{12}^2 E_0^2}{4\Delta^2} \cos(\omega_{IR}\tau) \frac{\delta(\omega - \omega_{IR}) + \delta(\omega + \omega_{IR})}{2} \right] \\
&= i \frac{d_{01}^2 d_{12}^2 E_0^2}{8\Delta^2} \cos(\omega_{IR}\tau) e^{-iE_n\tau} e^{i\varphi} \frac{1}{\left(\frac{\Gamma}{2} + i(\omega - E_n \pm \omega_{IR})\right)}.
\end{aligned} \tag{B.8}$$

B.2 Non-Centrosymmetric Terms

Next, the non-centrosymmetric terms are solved:

$$\begin{aligned}
d(t)_{\text{NSYM-SB}} &= i\vartheta(t-\tau)e^{-\frac{\Gamma}{2}(t-\tau)}e^{i\varphi} d_{01}^2 e^{i(E_n)(t-\tau)} \sin \alpha(\tau) \cos \alpha(t) \\
d(t)_{\text{NSYM-LIS}} &= i\vartheta(t-\tau)e^{-\frac{\Gamma}{2}(t-\tau)}e^{i\varphi} d_{01}^2 e^{i(E_n)(t-\tau)} \cos \alpha(\tau) \sin \alpha(t).
\end{aligned} \tag{B.9}$$

Appendix B Spectral Solutions of the Adiabatic Approximation

Approximating as before:

$$\begin{aligned}
d(\omega)_{\text{NSYM-SB}} &\approx \mathcal{F}[i\vartheta(t-\tau)e^{-\frac{\Gamma}{2}(t-\tau)}e^{iE_n(t-\tau)}e^{i\varphi}] * d_{01}d_{02}\mathcal{F}\left[\frac{1}{2\Delta}\Omega(\tau)\left(1 - \frac{\Omega(t)^2}{8\Delta^2}\right)\right] \\
&= \left[e^{-iE_n\tau} \frac{ie^{i\varphi}}{\sqrt{2\pi}\left(\frac{\Gamma}{2} + i(\omega - E_n)\right)} \right] \\
&\quad * d_{01}d_{02} \sqrt{\frac{\pi}{2}} \left[\left(\delta(\omega) - \frac{d_{12}^2 E_0^2}{16\Delta^2} (\delta(\omega) + \delta(\omega \pm 2\omega_{IR})) \right) \left(\frac{d_{12}E_0}{2\Delta} \cos(\omega_{IR}\tau) \right) \right] \\
&= ie^{-iE_n\tau} e^{i\varphi} \left(\frac{d_{12}E_0}{2\Delta} \cos(\omega_{IR}\tau) \right) \left[\frac{1}{2\left(\frac{\Gamma}{2} + i(\omega - E_n)\right)} \left(1 - \frac{d_{12}^2 E_0^2}{16\Delta^2} \right) \right. \\
&\quad \left. + \frac{d_{12}^2 E_0^2}{16\Delta^2} \frac{1}{2\left(\frac{\Gamma}{2} + i(\omega - E_n \pm 2\omega_{IR})\right)} \right]
\end{aligned} \tag{B.10}$$

and

$$\begin{aligned}
d(\omega)_{\text{NSYM-LIS}} &\approx \mathcal{F}[i\vartheta(t-\tau)e^{-\frac{\Gamma}{2}(t-\tau)}e^{iE_n(t-\tau)}e^{i\varphi}] * d_{01}d_{02}\mathcal{F}\left[\left(1 - \frac{\Omega(\tau)^2}{8\Delta^2}\right)\frac{1}{2\Delta}\Omega(t)\right] \\
&= \left[e^{-iE_n\tau} \frac{ie^{i\varphi}}{\sqrt{2\pi}\left(\frac{\Gamma}{2} + i(\omega - E_n)\right)} \right] \\
&\quad * d_{01}d_{02} \left[\frac{\sqrt{2\pi}E_0d_{12}}{2\Delta} \frac{\delta(\omega - \omega_{IR}) + \delta(\omega + \omega_{IR})}{2} \right] \left(1 - \frac{d_{12}^2 E_0^2}{8\Delta^2} \cos(\omega_{IR}\tau)^2 \right) \\
&= ie^{-iE_n\tau} \left(1 - \frac{d_{12}^2 E_0^2}{8\Delta^2} \cos(\omega_{IR}\tau)^2 \right) e^{i\varphi} \frac{E_0d_{12}}{2\Delta\left(\frac{\Gamma}{2} + i(\omega - E_n \pm \omega_{IR})\right)}.
\end{aligned} \tag{B.11}$$

B.3 Delay-Dependent Interference with XUV-Field

In the spectral solutions (see previous sections) we encounter the hyperbolic oscillation terms of the form $e^{-iE_n\tau}$ originating from the accumulated phase between excitation by the XUV pulse and the interaction with the NIR pulse. However, the observable signal is (cf. Eq. 2.12):

$$S(\omega, \tau) = \text{Im} \left[\frac{d(\omega)}{\varepsilon_{\text{XUV}}(\omega)} \right]. \tag{B.12}$$

B.3 Delay-Dependent Interference with XUV-Field

Since a Dirac-delta pulse was assumed in the deviation of the adiabatic solution $\epsilon_{XUV}(\omega) \propto e^{-i\omega\tau}$. The additional fast oscillating term $e^{i\omega\tau}$ will therefore need to be considered. This modifies the observable delay-dependent dynamic at the light-induced structures and sidebands. For the centrosymmetric light-induced structure, the temporal behavior at the sideband energy is:

$$\begin{aligned} S(E_n \pm \omega_{IR}, \tau) &\propto \text{Im} \left[\frac{i \cos(\omega_{IR}\tau) e^{-iE_n\tau}}{e^{-i(E_n \pm \omega_{IR})\tau}} \right] = \text{Re}[\cos(\omega_{IR}\tau) e^{\pm i\omega_{IR}\tau}] \\ &= \pm \cos(\omega_{IR}\tau)^2. \end{aligned} \quad (\text{B.13})$$

Therefore, at resonance, the symmetric light-induced structure will be modulated by $\cos(\omega_{IR}\tau)^2$. Likewise, we can apply this argument to the non-symmetric sideband, where $\pm\omega_{IR}$ energies will be modulated by $\cos(\omega_{IR}\tau)^3$.

C Appendix C

Delay-Dependent Solution of the Light-Induced Phase

As argued in Section 7.2, the light-induced phase can be approximated as a constant function in time, as it was also done in the previous section. This however neglects the delay-dependence of the light-induced phase effect, that was observed in Section 2.2 and Chapter 4. In this section, we apply several approximation to include the sub-cycle dependence close to the temporal overlap of the NIR pulse with the XUV pulse and will argue for a modeled inclusion of the decay of excited state. The equation we want to solve is (cf. 7.12):

$$\mathcal{F}[i\vartheta(t-\tau)e^{-\frac{\Gamma}{2}(t-\tau)}e^{jE_n(t-\tau)}e^{j\frac{1}{2\Delta}\int_{\tau}^t dt'\Omega^2(t')}] \quad (\text{C.1})$$

To solve the Fourier transform of the light-induced phase, we therefore need to find a solution to the improper integral of Eq. 7.12:

$$\mathcal{F}[e^{j\frac{1}{2\Delta}\int_{\tau}^t \Omega^2(t') dt'}](\omega). \quad (\text{C.2})$$

We will use the integration properties of the Fourier transform [50]:

$$\mathcal{F}\left[\int_{-\infty}^t g(t') dt'\right] = \sqrt{2\pi}G(0)\delta(\omega) + \frac{G(\omega)}{i\omega}, \quad (\text{C.3})$$

where $G(\omega) = \mathcal{F}[g(t)](\omega)$, and

$$G(0) = \int_{-\infty}^{\infty} g(t) dt. \quad (\text{C.4})$$

Approximating the exponential in Eq. C.2 we can write:

$$\begin{aligned} \mathcal{F}\left[1 + i\frac{1}{2\Delta}\int_{\tau}^t dt'\Omega^2(t')\right](\omega) \\ = \delta(\omega) + i\frac{\sqrt{2\pi}}{2\Delta}\left(\int_{-\infty}^{\infty} \vartheta(t-\tau)\Omega^2(t) dt \delta(\omega) + \frac{\mathcal{F}[\vartheta(t-\tau)\Omega^2(t)](\omega)}{i\omega}\right). \end{aligned}$$

(C.5)

To get the analytical expression of the spectral representation, we can again apply the convolution theorem, as before:

$$\begin{aligned} \mathcal{F}[i\vartheta(t-\tau)e^{-\frac{\Gamma}{2}(t-\tau)}e^{iE_n(t-\tau)}e^{j\frac{1}{2\Delta}\int_{\tau}^t\Omega^2(t')dt'}] &\approx e^{-i\tau\omega}\frac{i}{\sqrt{2\pi}(\frac{\Gamma}{2}+i(\omega-(E_n)))} \\ &* \left[\delta(\omega) + i\frac{\sqrt{2\pi}}{2\Delta} \left(\int_{-\infty}^{\infty} \vartheta(t-\tau)\Omega^2(t) dt \delta(\omega) + \frac{F[\vartheta(t-\tau)\Omega^2(t)](\omega)}{i\omega} \right) \right]. \end{aligned} \quad (\text{C.6})$$

We know from the previous section, that the Fourier transform of Ω^2 leads to two sidebands, for which we have found solutions in the previous parts assuming monochromatic waves. We will ignore it for now, and focus on the first parts. Since the Dirac-delta function acts as the identity of convolutions:

$$f * \delta = f, \quad (\text{C.7})$$

we can quickly find a solution:

$$\begin{aligned} &e^{-i\tau\omega}\frac{i}{\sqrt{2\pi}(\frac{\Gamma}{2}+i(\omega-(E_n)))} * \delta(\omega) \left(1 + i\frac{\sqrt{2\pi}}{2\Delta} \int_{-\infty}^{\infty} \vartheta(t-\tau)\Omega^2(t) dt \right) \\ &= e^{-i\tau(E_0\pm\Delta)}\frac{i}{\sqrt{2\pi}(\frac{\Gamma}{2}+i(\omega-(E_0\pm\Delta)))} \left[1 + i\frac{\sqrt{2\pi}}{2\Delta} \int_{-\infty}^{\infty} \vartheta(t-\tau)\Omega^2(t) dt \right] \\ &\approx e^{-i\tau(E_0\pm\Delta)}\frac{i}{\sqrt{2\pi}(\frac{\Gamma}{2}+i(\omega-(E_0\pm\Delta)))} e^{j\frac{\sqrt{2\pi}}{2\Delta} \int_{-\infty}^{\infty} \vartheta(t-\tau)\Omega^2(t) dt}. \end{aligned} \quad (\text{C.8})$$

This derivation of the light-induced phase sufficiently covers the sub-cycle dependence that has been observed in Section 2.2 and Chapter 4. However, it does not cover the dephasing of the excited states. This is a general limitation of the analytical spectral solutions presented here, but not of the analytical expression for the time-dependent dipole and its numerical spectral representation by a Fast Fourier Transform (FFT). In Eq. 4.1, the dephasing of the excited states is therefore explicitly included in the modeling of the LIP:

$$\varphi(\tau) = \frac{\sqrt{2\pi}}{2\Delta} \int_{-\infty}^{\infty} \vartheta(t-\tau)e^{-\frac{\Gamma}{2}(t-\tau)}\Omega(t)^2 dt. \quad (\text{C.9})$$

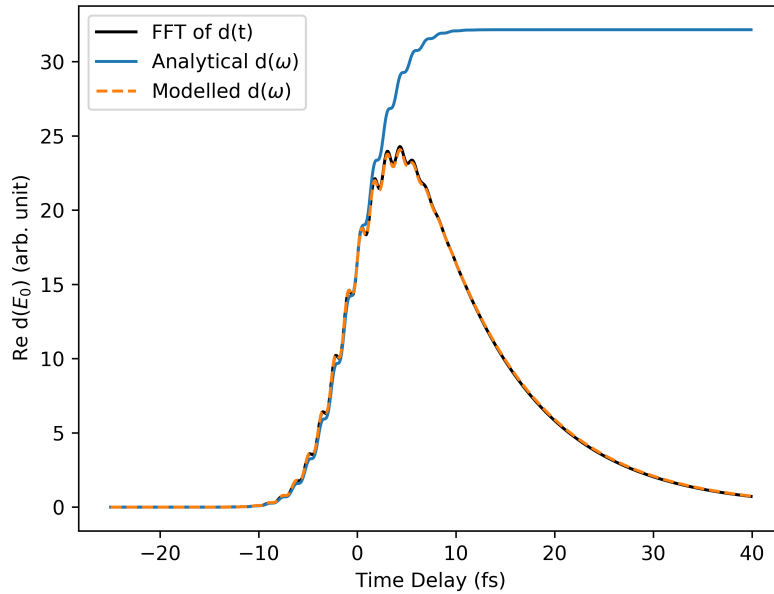


Figure C.1: Comparison of light induced phase models. The amplitude of the real part of the dipole spectrum caused by the light induced phase from various models. The FFT of the time-dependent dipole (black, Eq. C.1) shows the sub-cycle dependence during temporal overlap of the NIR and XUV pulse and the decay of the signal at larger time-delays. While the approximated analytical solution (blue, Eq. C.8) reproduces this sub-cycle behavior, it does not correctly reproduce the decay. However, the modelled solution of the LIP (dashed orange, Eq. C.9) does reproduce both behaviors and shows a very good agreement with the FFT solution.

To confirm the validity of the model, we compare the amplitude of the real part of the dipole spectrum caused by the light-induced phase from various models. The results are shown in Fig. C.1 using the same parameters as in Section 2.1. It shows a very good agreement of the FFT of the time-dependent dipole and the parametrized expression of Eq. C.9, warranting its use in Chapter 4.

List of Publications

Associated with this thesis

- L. Drescher, O. Kornilov, T. Witting, *et al.* “Extreme-Ultraviolet Refractive Optics.” In: *Nature* 564.7734 (2018), p. 91. DOI: 10.1038/s41586-018-0737-3
- L. Drescher, G. Reitsma, T. Witting, *et al.* “State-Resolved Probing of Attosecond Timescale Molecular Dipoles.” In: *The Journal of Physical Chemistry Letters* 10.2 (2019), pp. 265–269. DOI: 10.1021/acs.jpcllett.8b02878
- L. Drescher, V. Shokeen, T. Witting, *et al.* “XUV Spectral Compression by Four-Wave-Mixing.” In preparation.
- L. Drescher *et al.* “Carrier-to-Envelope Phase Control of Attosecond Transient Absorption.” In preparation.
- B. Schütte, L. Drescher, T. Witting, M. J. J. Vrakking, and O. Kornilov. “Time-Resolved Extreme-Ultraviolet Refraction.” In preparation.

Other

- L. Drescher, M. C. E. Galbraith, G. Reitsma, *et al.* “Communication: XUV Transient Absorption Spectroscopy of Iodomethane and Iodobenzene Photodissociation.” In: *The Journal of Chemical Physics* 145.1 (2016), p. 011101. DOI: 10.1063/1.4955212

Bibliography

- [1] R. E. Blankenship. *Molecular Mechanisms of Photosynthesis*. John Wiley & Sons, 2014. 312 pp.
- [2] O. Flender, M. Scholz, J. Hölzer, K. Oum, and T. Lenzer. “A Comprehensive Picture of the Ultrafast Excited-State Dynamics of Retinal.” In: *Physical Chemistry Chemical Physics* 18.22 (2016), pp. 14941–14948. doi: 10.1039/C6CP01335J.
- [3] A. H. Zewail. “Femtochemistry: Atomic-Scale Dynamics of the Chemical Bond.” In: *The Journal of Physical Chemistry A* 104.24 (2000), pp. 5660–5694. doi: 10.1021/jp001460h.
- [4] K. C. Kulander, K. J. Schafer, and J. L. Krause. “Dynamics of Short-Pulse Excitation, Ionization and Harmonic Conversion.” In: *Super-Intense Laser-Atom Physics*. Ed. by B. Piraux, A. L’Huillier, and K. Rzażewski. NATO ASI Series. Boston, MA: Springer US, 1993, pp. 95–110. doi: 10.1007/978-1-4615-7963-2_10.
- [5] P. B. Corkum. “Plasma Perspective on Strong Field Multiphoton Ionization.” In: *Physical Review Letters* 71.13 (1993), pp. 1994–1997. doi: 10.1103/PhysRevLett.71.1994.
- [6] M. Lewenstein, P. Balcou, M. Y. Ivanov, A. L’Huillier, and P. B. Corkum. “Theory of High-Harmonic Generation by Low-Frequency Laser Fields.” In: *Physical Review A* 49.3 (1994), pp. 2117–2132. doi: 10.1103/PhysRevA.49.2117.
- [7] Z. Chang. *Fundamentals of Attosecond Optics*. CRC Press, 2011. 536 pp.
- [8] P. M. Paul, E. S. Toma, P. Breger, *et al.* “Observation of a Train of Attosecond Pulses from High Harmonic Generation.” In: *Science* 292.5522 (2001), pp. 1689–1692. doi: 10.1126/science.1059413.
- [9] M. Hentschel, R. Kienberger, C. Spielmann, *et al.* “Attosecond Metrology.” In: *Nature* 414.6863 (2001), pp. 509–513. doi: 10.1038/35107000.
- [10] M. Drescher, M. Hentschel, R. Kienberger, *et al.* “Time-Resolved Atomic Inner-Shell Spectroscopy.” In: *Nature* 419.6909 (2002), pp. 803–807. doi: 10.1038/nature01143.

Bibliography

- [11] F. Krausz and M. Ivanov. “Attosecond Physics.” In: *Reviews of Modern Physics* 81.1 (2009), pp. 163–234. DOI: 10.1103/RevModPhys.81.163.
- [12] L. F. DiMauro. “Atomic Photography.” In: *Nature* 419.6909 (2002), pp. 789–790. DOI: 10.1038/419789a.
- [13] J. Baggott. “Chemistry In A New Light.” In: *New Chemistry*. Ed. by N. Hall. Cambridge University Press, 2000.
- [14] M. C. E. Galbraith, C. T. L. Smeenk, G. Reitsma, *et al.* “XUV-Induced Reactions in Benzene on Sub-10 Fs Timescale: Nonadiabatic Relaxation and Proton Migration.” In: *Physical Chemistry Chemical Physics* 19.30 (2017), pp. 19822–19828. DOI: 10.1039/C7CP02255G.
- [15] Y. Kobayashi, K. F. Chang, T. Zeng, D. M. Neumark, and S. R. Leone. “Direct Mapping of Curve-Crossing Dynamics in IBr by Attosecond Transient Absorption Spectroscopy.” In: *Science* 365.6448 (2019), pp. 79–83. DOI: 10.1126/science.aax0076.
- [16] F. Lépine, M. Y. Ivanov, and M. J. J. Vrakking. “Attosecond Molecular Dynamics: Fact or Fiction?” In: *Nature Photonics* 8.3 (2014), pp. 195–204. DOI: 10.1038/nphoton.2014.25.
- [17] G. Sansone, F. Kelkensberg, J. F. Pérez-Torres, *et al.* “Electron Localization Following Attosecond Molecular Photoionization.” In: *Nature* 465.7299 (2010), pp. 763–766. DOI: 10.1038/nature09084.
- [18] V. Despré, A. Marciniak, V. Loriot, *et al.* “Attosecond Hole Migration in Benzene Molecules Surviving Nuclear Motion.” In: *The Journal of Physical Chemistry Letters* 6.3 (2015), pp. 426–431. DOI: 10.1021/jz502493j.
- [19] M. A. Robb, A. J. Jenkins, and M. Vacher. “How Nuclear Motion Affects Coherent Electron Dynamics in Molecules.” In: *Attosecond Molecular Dynamics*. 2018, pp. 275–307. DOI: 10.1039/9781788012669-00275.
- [20] F. Bloch. “Nuclear Induction.” In: *Physical Review* 70.7-8 (1946), pp. 460–474. DOI: 10.1103/PhysRev.70.460.
- [21] E. L. Hahn. “Nuclear Induction Due to Free Larmor Precession.” In: *Physical Review* 77.2 (1950), pp. 297–298. DOI: 10.1103/PhysRev.77.297.2.
- [22] R. G. Brewer and R. L. Shoemaker. “Optical Free Induction Decay.” In: *Physical Review A* 6.6 (1972), pp. 2001–2007. DOI: 10.1103/PhysRevA.6.2001.

- [23] M. Wu, S. Chen, S. Camp, K. J. Schafer, and M. B. Gaarde. “Theory of Strong-Field Attosecond Transient Absorption.” In: *Journal of Physics B: Atomic, Molecular and Optical Physics* 49.6 (2016), p. 062003. DOI: 10.1088/0953-4075/49/6/062003.
- [24] S. Bengtsson, E. W. Larsen, D. Kroon, *et al.* “Space–Time Control of Free Induction Decay in the Extreme Ultraviolet.” In: *Nature Photonics* 11.4 (2017), pp. 252–258. DOI: 10.1038/nphoton.2017.30.
- [25] M. Holler, F. Schapper, L. Gallmann, and U. Keller. “Attosecond Electron Wave-Packet Interference Observed by Transient Absorption.” In: *Physical Review Letters* 106.12 (2011), p. 123601. DOI: 10.1103/PhysRevLett.106.123601.
- [26] M. Chini, X. Wang, Y. Cheng, *et al.* “Sub-Cycle Oscillations in Virtual States Brought to Light.” In: *Scientific Reports* 3 (2013), p. 1105. DOI: 10.1038/srep01105.
- [27] A. R. Beck, B. Bernhardt, E. R. Warrick, *et al.* “Attosecond Transient Absorption Probing of Electronic Superpositions of Bound States in Neon: Detection of Quantum Beats.” In: *New Journal of Physics* 16.11 (2014), p. 113016. DOI: 10.1088/1367-2630/16/11/113016.
- [28] M. Chini, B. Zhao, H. Wang, *et al.* “Subcycle Ac Stark Shift of Helium Excited States Probed with Isolated Attosecond Pulses.” In: *Physical Review Letters* 109.7 (2012), p. 073601. DOI: 10.1103/PhysRevLett.109.073601.
- [29] C. Ott, A. Kaldun, P. Raith, *et al.* “Lorentz Meets Fano in Spectral Line Shapes: A Universal Phase and Its Laser Control.” In: *Science* 340.6133 (2013), pp. 716–720. DOI: 10.1126/science.1234407.
- [30] C. Ott, A. Kaldun, L. Argenti, *et al.* “Reconstruction and Control of a Time-Dependent Two-Electron Wave Packet.” In: *Nature* 516.7531 (2014), pp. 374–378. DOI: 10.1038/nature14026.
- [31] E. Goulielmakis, Z.-H. Loh, A. Wirth, *et al.* “Real-Time Observation of Valence Electron Motion.” In: *Nature* 466.7307 (2010), pp. 739–743. DOI: 10.1038/nature09212.
- [32] A. Kaldun, A. Blättermann, V. Stooß, *et al.* “Observing the Ultrafast Buildup of a Fano Resonance in the Time Domain.” In: *Science* 354.6313 (2016), pp. 738–741. DOI: 10.1126/science.aah6972.

Bibliography

- [33] C.-T. Liao, X. Li, D. J. Haxton, *et al.* “Probing Autoionizing States of Molecular Oxygen with XUV Transient Absorption: Electronic-Symmetry-Dependent Line Shapes and Laser-Induced Modifications.” In: *Physical Review A* 95.4 (2017), p. 043427. DOI: 10.1103/PhysRevA.95.043427.
- [34] M. Reduzzi, J. Hummert, A. Dubrouil, *et al.* “Polarization Control of Absorption of Virtual Dressed States in Helium.” In: *Physical Review A* 92.3 (2015), p. 033408. DOI: 10.1103/PhysRevA.92.033408.
- [35] E. R. Warrick, W. Cao, D. M. Neumark, and S. R. Leone. “Probing the Dynamics of Rydberg and Valence States of Molecular Nitrogen with Attosecond Transient Absorption Spectroscopy.” In: *The Journal of Physical Chemistry A* (2016). DOI: 10.1021/acs.jpca.5b11570.
- [36] F. Calegari, D. Ayuso, A. Trabattoni, *et al.* “Ultrafast Electron Dynamics in Phenylalanine Initiated by Attosecond Pulses.” In: *Science* 346.6207 (2014), pp. 336–339. DOI: 10.1126/science.1254061.
- [37] P. M. Kraus, B. Mignolet, D. Baykusheva, *et al.* “Measurement and Laser Control of Attosecond Charge Migration in Ionized Iodoacetylene.” In: *Science* 350.6262 (2015), pp. 790–795. DOI: 10.1126/science.aab2160.
- [38] H. J. B. Marroux, A. Fidler, Y. Kobayashi, *et al.* “Attosecond Transient Absorption of Molecular Core-Excited States: Core-Hole Lifetime Dependence on Orbital Alignment Relative to Molecular Bond.” In: 7th International Conference on Attosecond Science and Technology. 2019.
- [39] L. Drescher, M. C. E. Galbraith, G. Reitsma, *et al.* “Communication: XUV Transient Absorption Spectroscopy of Iodomethane and Iodobenzene Photodissociation.” In: *The Journal of Chemical Physics* 145.1 (2016), p. 011101. DOI: 10.1063/1.4955212.
- [40] L. Drescher. “XUV Transient Absorption Spectroscopy of Photochemical Reactions.” Master Thesis. Freie Universität Berlin, 2016.
- [41] R. L. Sandberg, A. Paul, D. A. Raymondson, *et al.* “Lensless Diffractive Imaging Using Tabletop Coherent High-Harmonic Soft-X-Ray Beams.” In: *Physical Review Letters* 99.9 (2007), p. 098103. DOI: 10.1103/PhysRevLett.99.098103.
- [42] R. Neutze, R. Wouts, D. van der Spoel, E. Weckert, and J. Hajdu. “Potential for Biomolecular Imaging with Femtosecond X-Ray Pulses.” In: *Nature* 406.6797 (2000), p. 752. DOI: 10.1038/35021099.
- [43] J. J. Rocca. “Table-Top Soft x-Ray Lasers.” In: *Review of Scientific Instruments* 70.10 (1999), pp. 3799–3827. DOI: 10.1063/1.1150041.

- [44] E. Allaria, R. Appio, L. Badano, *et al.* “Highly Coherent and Stable Pulses from the FERMI Seeded Free-Electron Laser in the Extreme Ultraviolet.” In: *Nature Photonics* 6.10 (2012), pp. 699–704. DOI: 10.1038/nphoton.2012.233.
- [45] Marangos J. P. “The Measurement of Ultrafast Electronic and Structural Dynamics with X-Rays.” In: *Philosophical Transactions of the Royal Society A: Mathematical, Physical and Engineering Sciences* 377.2145 (2019), p. 20170481. DOI: 10.1098/rsta.2017.0481.
- [46] T. Brabec and F. Krausz. “Intense Few-Cycle Laser Fields: Frontiers of Nonlinear Optics.” In: *Reviews of Modern Physics* 72.2 (2000), pp. 545–591. DOI: 10.1103/RevModPhys.72.545.
- [47] M. B. Gaarde, C. Buth, J. L. Tate, and K. J. Schafer. “Transient Absorption and Reshaping of Ultrafast XUV Light by Laser-Dressed Helium.” In: *Physical Review A* 83.1 (2011), p. 013419. DOI: 10.1103/PhysRevA.83.013419.
- [48] R. W. Boyd. *Nonlinear Optics*. Academic Press, 2013. 454 pp.
- [49] E. P. Wigner. *Gruppentheorie und ihre Anwendung auf die Quantenmechanik der Atomspektren*. Vieweg+Teubner Verlag, 1931.
- [50] N. Morrison. *Introduction to Fourier Analysis*. Wiley, 1994. 600 pp.
- [51] J. J. Rørstad, J. E. Bækhoj, and L. B. Madsen. “Analytic Modeling of Structures in Attosecond Transient-Absorption Spectra.” In: *Physical Review A* 96.1 (2017), p. 013430. DOI: 10.1103/PhysRevA.96.013430.
- [52] S. Chen, M. Wu, M. B. Gaarde, and K. J. Schafer. “Quantum Interference in Attosecond Transient Absorption of Laser-Dressed Helium Atoms.” In: *Physical Review A* 87.3 (2013), p. 033408. DOI: 10.1103/PhysRevA.87.033408.
- [53] W. L. Wiese and J. R. Fuhr. “Accurate Atomic Transition Probabilities for Hydrogen, Helium, and Lithium.” In: *Journal of Physical and Chemical Reference Data* 38.3 (2009), pp. 565–720. DOI: 10.1063/1.3077727.
- [54] S. Chen, M. Wu, M. B. Gaarde, and K. J. Schafer. “Laser-Imposed Phase in Resonant Absorption of an Isolated Attosecond Pulse.” In: *Physical Review A* 88.3 (2013), p. 033409. DOI: 10.1103/PhysRevA.88.033409.
- [55] C. Neidel, J. Klei, C.-H. Yang, *et al.* “Probing Time-Dependent Molecular Dipoles on the Attosecond Time Scale.” In: *Physical Review Letters* 111.3 (2013), p. 033001. DOI: 10.1103/PhysRevLett.111.033001.

Bibliography

- [56] M. C. E. Galbraith, S. Scheit, N. V. Golubev, *et al.* “Few-Femtosecond Passage of Conical Intersections in the Benzene Cation.” In: *Nature Communications* 8.1 (2017), p. 1018. DOI: 10.1038/s41467-017-01133-y.
- [57] Siu, W.K. and Radboud University Nijmegen. “Probing molecular dynamics using novel light sources.” [S.l. : s.n.], 2011.
- [58] Gademann, G. and Radboud University Nijmegen. “Expanding the attosecond toolbox: demonstration of novel experiments, new light sources and detectors.” [S.l. : s.n.], 2011.
- [59] G. Gademann, F. Kelkensberg, W. K. Siu, *et al.* “Attosecond Control of Electron–Ion Recollision in High Harmonic Generation.” In: *New Journal of Physics* 13.3 (2011), p. 033002. DOI: 10.1088/1367-2630/13/3/033002.
- [60] A. Rouzée, F. Kelkensberg, W. K. Siu, *et al.* “Photoelectron Kinetic and Angular Distributions for the Ionization of Aligned Molecules Using a HHG Source.” In: *Journal of Physics B: Atomic, Molecular and Optical Physics* 45.7 (2012), p. 074016. DOI: 10.1088/0953-4075/45/7/074016.
- [61] A. Marciniak, V. Despré, T. Barillot, *et al.* “XUV Excitation Followed by Ultrafast Non-Adiabatic Relaxation in PAH Molecules as a Femto-Astrochemistry Experiment.” In: *Nature Communications* 6.1 (2015), pp. 1–6. DOI: 10.1038/ncomms8909.
- [62] M. C. E. Galbraith. “Time-Resolved Spectroscopy with Attosecond Pulses and Pulse Trains: Ultrafast Relaxation in Benzene Cations.” Freie Universität Berlin, Freie Universität Berlin, Germany, 2017.
- [63] P. F. Moulton. “Spectroscopic and Laser Characteristics of Ti:Al₂O₃.” In: *Journal of the Optical Society of America B Optical Physics* 3 (1986), pp. 125–133. DOI: 10.1364/JOSAB.3.000125.
- [64] D. Strickland and G. Mourou. “Compression of Amplified Chirped Optical Pulses.” In: *Optics Communications* 56.3 (1985), pp. 219–221. DOI: 10.1016/0030-4018(85)90120-8.
- [65] F. Verluise, V. Laude, Z. Cheng, C. Spielmann, and P. Tournois. “Amplitude and Phase Control of Ultrashort Pulses by Use of an Acousto-Optic Programmable Dispersive Filter: Pulse Compression and Shaping.” In: *Optics Letters* 25.8 (2000), pp. 575–577. DOI: 10.1364/OL.25.000575.

- [66] T. Oksenhendler, D. Kaplan, P. Tournois, G. Greetham, and F. Estable. “Intracavity Acousto-Optic Programmable Gain Control for Ultra-Wide-Band Regenerative Amplifiers.” In: *Applied Physics B* 83.4 (2006), p. 491. DOI: 10.1007/s00340-006-2231-0.
- [67] G. Sansone, E. Benedetti, F. Calegari, *et al.* “Isolated Single-Cycle Attosecond Pulses.” In: *Science* 314.5798 (2006), pp. 443–446. DOI: 10.1126/science.1132838.
- [68] T. Witting, F. Frank, C. A. Arrell, *et al.* “Characterization of High-Intensity Sub-4-Fs Laser Pulses Using Spatially Encoded Spectral Shearing Interferometry.” In: *Optics Letters* 36.9 (2011), pp. 1680–1682. DOI: 10.1364/OL.36.001680.
- [69] M. B. Gaarde, J. L. Tate, and K. J. Schafer. “Macroscopic Aspects of Attosecond Pulse Generation.” In: *Journal of Physics B: Atomic, Molecular and Optical Physics* 41.13 (2008), p. 132001. DOI: 10.1088/0953-4075/41/13/132001.
- [70] P. Antoine, A. L’Huillier, and M. Lewenstein. “Attosecond Pulse Trains Using High-Order Harmonics.” In: *Physical Review Letters* 77.7 (1996), pp. 1234–1237. DOI: 10.1103/PhysRevLett.77.1234.
- [71] Y. Mairesse, A. de Bohan, L. J. Frasinski, *et al.* “Attosecond Synchronization of High-Harmonic Soft X-Rays.” In: *Science* 302.5650 (2003), pp. 1540–1543. DOI: 10.1126/science.1090277.
- [72] R. López-Martens, K. Varjú, P. Johnsson, *et al.* “Amplitude and Phase Control of Attosecond Light Pulses.” In: *Physical Review Letters* 94.3 (2005), p. 033001. DOI: 10.1103/PhysRevLett.94.033001.
- [73] P. Bédot, B. E. Schmidt, J. Kasparian, J.-P. Wolf, and F. Legaré. “Mechanism of Hollow-Core-Fiber Infrared-Supercontinuum Compression with Bulk Material.” In: *Physical Review A* 81.6 (2010), p. 063828. DOI: 10.1103/PhysRevA.81.063828.
- [74] G. Tempea and T. Brabec. “Theory of Self-Focusing in a Hollow Waveguide.” In: *Optics Letters* 23.10 (1998), pp. 762–764. DOI: 10.1364/OL.23.000762.
- [75] M. Nurhuda, A. Suda, K. Midorikawa, M. Hatayama, and K. Nagasaka. “Propagation Dynamics of Femtosecond Laser Pulses in a Hollow Fiber Filled with Argon: Constant Gas Pressure versus Differential Gas Pressure.” In: *JOSA B* 20.9 (2003), pp. 2002–2011. DOI: 10.1364/JOSAB.20.002002.

Bibliography

- [76] M. Nurhuda, A. Suda, M. Kaku, and K. Midorikawa. "Optimization of Hollow Fiber Pulse Compression Using Pressure Gradients." In: *Applied Physics B* 89.2 (2007), pp. 209–215. doi: 10.1007/s00340-007-2792-6.
- [77] H. Timmers, Y. Kobayashi, K. F. Chang, *et al.* "Generating High-Contrast, near Single-Cycle Waveforms with Third-Order Dispersion Compensation." In: *Optics Letters* 42.4 (2017), pp. 811–814. doi: 10.1364/OL.42.000811.
- [78] G. Ghosh and G. Bhar. "Temperature Dispersion in ADP, KDP, and KD*P for Nonlinear Devices." In: *IEEE Journal of Quantum Electronics* 18.2 (1982), pp. 143–145. doi: 10.1109/JQE.1982.1071501.
- [79] M. Miranda, J. Penedones, C. Guo, *et al.* "Generalized Projection Retrieval of Dispersion Scans for Ultrashort Pulse Characterization." In: (2016).
- [80] F. Silva, M. Miranda, B. Alonso, *et al.* "Simultaneous Compression, Characterization and Phase Stabilization of GW-Level 1.4 Cycle VIS-NIR Femtosecond Pulses Using a Single Dispersion-Scan Setup." In: *Optics Express* 22.9 (2014), pp. 10181–10191. doi: 10.1364/OE.22.010181.
- [81] L. Drescher, G. Reitsma, T. Witting, *et al.* "State-Resolved Probing of Attosecond Timescale Molecular Dipoles." In: *The Journal of Physical Chemistry Letters* 10.2 (2019), pp. 265–269. doi: 10.1021/acs.jpcclett.8b02878.
- [82] T. N. Olney, G. Cooper, and C. E. Brion. "Quantitative Studies of the Photoabsorption (4.5–488 eV) and Photoionization (9–59.5 eV) of Methyl Iodide Using Dipole Electron Impact Techniques." In: *Chemical Physics* 232.1–2 (1998), pp. 211–237. doi: 10.1016/S0301-0104(97)00368-6.
- [83] A. P. Hitchcock and C. E. Brion. "Inner Shell Excitation of CH 3F, CH 3Cl, CH 3Br and CH 3I by 2.5 keV Electron Impact." In: *Journal of Electron Spectroscopy and Related Phenomena* 13.3 (1978), pp. 193–218. doi: 10.1016/0368-2048(78)85027-0.
- [84] J. N. Cutler, G. M. Bancroft, and K. H. Tan. "Ligand-field Splittings and Core-level Linewidths in I 4d Photoelectron Spectra of Iodine Molecules." In: *The Journal of Chemical Physics* 97.11 (1992), pp. 7932–7943. doi: 10.1063/1.463468.
- [85] S. Chen, M. J. Bell, A. R. Beck, *et al.* "Light-Induced States in Attosecond Transient Absorption Spectra of Laser-Dressed Helium." In: *Physical Review A* 86.6 (2012), p. 063408. doi: 10.1103/PhysRevA.86.063408.

- [86] W. H. Press, S. A. Teukolsky, W. T. Vetterling, and B. P. Flannery. *Numerical Recipes 3rd Edition: The Art of Scientific Computing*. 3 edition. Cambridge, UK ; New York: Cambridge University Press, 2007. 1256 pp.
- [87] A. S. Johnson, D. R. Austin, D. A. Wood, *et al.* “High-Flux Soft x-Ray Harmonic Generation from Ionization-Shaped Few-Cycle Laser Pulses.” In: *Science Advances* 4.5 (2018), eaar3761. DOI: 10.1126/sciadv.aar3761.
- [88] L. Young, K. Ueda, M. Gühr, *et al.* “Roadmap of Ultrafast X-Ray Atomic and Molecular Physics.” In: *Journal of Physics B: Atomic, Molecular and Optical Physics* 51.3 (2018), p. 032003. DOI: 10.1088/1361-6455/aa9735.
- [89] L. Drescher, O. Kornilov, T. Witting, *et al.* “Extreme-Ultraviolet Refractive Optics.” In: *Nature* 564.7734 (2018), p. 91. DOI: 10.1038/s41586-018-0737-3.
- [90] A. Snigirev, V. Kohn, I. Snigireva, and B. Lengeler. “A Compound Refractive Lens for Focusing High-Energy X-Rays.” In: *Nature* 384.6604 (1996), pp. 49–51. DOI: 10.1038/384049a0.
- [91] W. C. Röntgen. “Ueber Eine Neue Art von Strahlen (Vorläufige Mittheilung).” In: *Sonderabdruck aus den Sitzungsberichten der Würzburger Physik.-medic. Gesellschaft* (1895).
- [92] P. Elleaume. “Two-Plane Focusing of 30 keV Undulator Radiation.” In: *Journal of Synchrotron Radiation* 5.1 (1998), pp. 1–5. DOI: 10.1107/S0909049597012818.
- [93] G. Santoro, A. Buffet, R. Döhrmann, *et al.* “Use of Intermediate Focus for Grazing Incidence Small and Wide Angle X-Ray Scattering Experiments at the Beamline P03 of PETRA III, DESY.” In: *Review of Scientific Instruments* 85.4 (2014), p. 043901. DOI: 10.1063/1.4869784.
- [94] M. Chollet, R. Alonso-Mori, M. Cammarata, *et al.* “The X-Ray Pump-Probe Instrument at the Linac Coherent Light Source.” In: *Journal of Synchrotron Radiation* 22.3 (2015), pp. 503–507. DOI: 10.1107/S1600577515005135.
- [95] P. Heimann, M. MacDonald, B. Nagler, *et al.* “Compound Refractive Lenses as Prefocusing Optics for X-Ray FEL Radiation.” In: *Journal of Synchrotron Radiation* 23 (Pt 2 2016), pp. 425–429. DOI: 10.1107/S1600577516001636.
- [96] B. Lengeler, C. G. Schroer, M. Richwin, *et al.* “A Microscope for Hard x Rays Based on Parabolic Compound Refractive Lenses.” In: *Applied Physics Letters* 74.26 (1999), pp. 3924–3926. DOI: 10.1063/1.124225.

Bibliography

- [97] C. G. Schroer, O. Kurapova, J. Patommel, *et al.* “Hard X-Ray Nanoprobe Based on Refractive x-Ray Lenses.” In: *Applied Physics Letters* 87.12 (2005), p. 124103. DOI: 10.1063/1.2053350.
- [98] J.-M. Meijer, A. Pal, S. Ouhajji, *et al.* “Observation of Solid–Solid Transitions in 3D Crystals of Colloidal Superballs.” In: *Nature Communications* 8 (2017), p. 14352. DOI: 10.1038/ncomms14352.
- [99] C. G. Schroer, P. Boye, J. M. Feldkamp, *et al.* “Coherent X-Ray Diffraction Imaging with Nanofocused Illumination.” In: *Physical Review Letters* 101.9 (2008), p. 090801. DOI: 10.1103/PhysRevLett.101.090801.
- [100] Y. Wang, W. Yun, and C. Jacobsen. “Achromatic Fresnel Optics for Wideband Extreme-Ultraviolet and X-Ray Imaging.” In: *Nature* 424.6944 (2003), pp. 50–53. DOI: 10.1038/nature01756.
- [101] H. Pan, C. Späth, A. Guggenmos, *et al.* “Low Chromatic Fresnel Lens for Broadband Attosecond XUV Pulse Applications.” In: *Optics Express* 24.15 (2016), pp. 16788–16798. DOI: 10.1364/OE.24.016788.
- [102] A. V. Baez. “A Self-Supporting Metal Fresnel Zone-Plate to Focus Extreme Ultra-Violet and Soft X-Rays.” In: *Nature* 186.4729 (1960), pp. 958–958. DOI: 10.1038/186958a0.
- [103] D. Roschdestwensky. “Anomale Dispersion Im Natriumdampf.” In: *Annalen der Physik* 344.12 (1912), pp. 307–345. DOI: 10.1002/andp.19123441203.
- [104] S. A. Korff and G. Breit. “Optical Dispersion.” In: *Reviews of Modern Physics* 4.3 (1932), pp. 471–503. DOI: 10.1103/RevModPhys.4.471.
- [105] M. Born and E. Wolf. “Principles of Optics.” In: *Principles of Optics, by Max Born and Emil Wolf and With contributions by AB Bhatia and PC Clemmow and D. Gabor and AR Stokes and AM Taylor and PA Wayman and WL Wilcock, pp. 986. ISBN 0521642221. Cambridge, UK: Cambridge University Press, October 1999. (1999), p. 986.*
- [106] W. L. Wiese, M. W. Smith, and B. M. Glennon. *Atomic Transition Probabilities. Vol.: Hydrogen through Neon. A Critical Data Compilation.* 1966.
- [107] W. L. Wiese, M. W. Smith, and B. M. Miles. *Atomic Transition Probabilities. Vol. 2: Sodium through Calcium. A Critical Data Compilation.* 1969.
- [108] B. Schütte, M. Arbeiter, T. Fennel, M. J. J. Vrakking, and A. Rouzée. “Rare-Gas Clusters in Intense Extreme-Ultraviolet Pulses from a High-Order Harmonic Source.” In: *Physical Review Letters* 112.7 (2014), p. 073003. DOI: 10.1103/PhysRevLett.112.073003.

- [109] G. Gademann. “Expanding the Attosecond Toolbox: Demonstration of Novel Experiments, New Light Sources and Detectors.” Radboud Universiteit Nijmegen, 2011.
- [110] S. Semushin and V. Malka. “High Density Gas Jet Nozzle Design for Laser Target Production.” In: *Review of Scientific Instruments* 72.7 (2001), pp. 2961–2965. DOI: 10.1063/1.1380393.
- [111] P. Tzallas, D. Charalambidis, N. A. Papadogiannis, K. Witte, and G. D. Tsakiris. “Direct Observation of Attosecond Light Bunching.” In: *Nature* 426.6964 (2003), pp. 267–271. DOI: 10.1038/nature02091.
- [112] E. J. Takahashi, P. Lan, O. D. Mücke, Y. Nabekawa, and K. Midorikawa. “Attosecond Nonlinear Optics Using Gigawatt-Scale Isolated Attosecond Pulses.” In: *Nature Communications* 4 (2013), p. 2691. DOI: 10.1038/ncomms3691.
- [113] B. Manschwetus, L. Rading, F. Campi, *et al.* “Two-Photon Double Ionization of Neon Using an Intense Attosecond Pulse Train.” In: *Physical Review A* 93.6 (2016), p. 061402. DOI: 10.1103/PhysRevA.93.061402.
- [114] T. R. Barillot, P. Matia-Hernando, D. Greening, *et al.* “Towards XUV Pump-Probe Experiments in the Femtosecond to Sub-Femtosecond Regime: New Measurement of the Helium Two-Photon Ionization Cross-Section.” In: *Chemical Physics Letters*. Ahmed Zewail (1946-2016) Commemoration Issue of Chemical Physics Letters 683 (2017), pp. 38–42. DOI: 10.1016/j.cplett.2017.05.026.
- [115] D. Rupp, N. Monserud, B. Langbehn, *et al.* “Coherent Diffractive Imaging of Single Helium Nanodroplets with a High Harmonic Generation Source.” In: *Nature Communications* 8.1 (2017), pp. 1–7. DOI: 10.1038/s41467-017-00287-z.
- [116] M. Flögel, J. Durá, B. Schütte, *et al.* “Rabi Oscillations in Extreme Ultraviolet Ionization of Atomic Argon.” In: *Physical Review A* 95.2 (2017), p. 021401. DOI: 10.1103/PhysRevA.95.021401.
- [117] K. J. Schafer and K. C. Kulander. “High Harmonic Generation from Ultrafast Pump Lasers.” In: *Physical Review Letters* 78.4 (1997), pp. 638–641. DOI: 10.1103/PhysRevLett.78.638.
- [118] U. Fröhling, M. Wieland, M. Gensch, *et al.* “Single-Shot Terahertz-Field-Driven X-Ray Streak Camera.” In: *Nature Photonics* 3.9 (2009), pp. 523–528. DOI: 10.1038/nphoton.2009.160.

Bibliography

- [119] J. Mauritsson, P. Johnsson, R. López-Martens, *et al.* “Measurement and Control of the Frequency Chirp Rate of High-Order Harmonic Pulses.” In: *Physical Review A* 70.2 (2004), p. 021801. DOI: 10.1103/PhysRevA.70.021801.
- [120] G. Wendin. “Collective Effects in Atomic Photoabsorption Spectra. III. Collective Resonance in the 4d10shell in Xe.” In: *Journal of Physics B: Atomic and Molecular Physics* 6.1 (1973), pp. 42–61. DOI: 10.1088/0022-3700/6/1/007.
- [121] H. J. Levinson and T. A. Brunner. “Current Challenges and Opportunities for EUV Lithography.” In: *International Conference on Extreme Ultraviolet Lithography 2018*. International Conference on Extreme Ultraviolet Lithography 2018. Vol. 10809. International Society for Optics and Photonics, 2018, p. 1080903. DOI: 10.1117/12.2502791.
- [122] V. Stooß, S. M. Cavaletto, S. Donsa, *et al.* “Real-Time Reconstruction of the Strong-Field-Driven Dipole Response.” In: *Physical Review Letters* 121.17 (2018), p. 173005. DOI: 10.1103/PhysRevLett.121.173005.
- [123] Y. Mairesse and F. Quéré. “Frequency-Resolved Optical Gating for Complete Reconstruction of Attosecond Bursts.” In: *Physical Review A* 71.1 (2005), p. 011401. DOI: 10.1103/PhysRevA.71.011401.
- [124] C. J. Kaplan, P. M. Kraus, A. D. Ross, *et al.* “Femtosecond Tracking of Carrier Relaxation in Germanium with Extreme Ultraviolet Transient Reflectivity.” In: *Physical Review B* 97.20 (2018), p. 205202. DOI: 10.1103/PhysRevB.97.205202.
- [125] C. J. Kaplan, P. M. Kraus, E. M. Gullikson, *et al.* “Retrieval of the Complex-Valued Refractive Index of Germanium near the $M_{4,5}$ Absorption Edge.” In: *JOSA B* 36.6 (2019), pp. 1716–1720. DOI: 10.1364/JOSAB.36.001716.
- [126] A. Barty, S. Boutet, M. J. Bogan, *et al.* “Ultrafast Single-Shot Diffraction Imaging of Nanoscale Dynamics.” In: *Nature Photonics* 2.7 (2008), pp. 415–419. DOI: 10.1038/nphoton.2008.128.
- [127] C. Wagner and N. Harned. “EUV Lithography: Lithography Gets Extreme.” In: *Nature Photonics* 4 (2010), pp. 24–26. DOI: 10.1038/nphoton.2009.251.
- [128] E. J. Sie, T. Rohwer, C. Lee, and N. Gedik. “Time-Resolved XUV ARPES with Tunable 24–33 eV Laser Pulses at 30 meV Resolution.” In: *Nature Communications* 10.1 (2019), p. 3535. DOI: 10.1038/s41467-019-11492-3.

- [129] B. Frietsch, R. Carley, K. Döbrich, *et al.* “A High-Order Harmonic Generation Apparatus for Time- and Angle-Resolved Photoelectron Spectroscopy.” In: *Review of Scientific Instruments* 84.7 (2013), p. 075106. doi: 10.1063/1.4812992.
- [130] S. Eich, A. Stange, A. Carr, *et al.* “Time- and Angle-Resolved Photoemission Spectroscopy with Optimized High-Harmonic Pulses Using Frequency-Doubled Ti:Sapphire Lasers.” In: *Journal of Electron Spectroscopy and Related Phenomena* 195 (2014), pp. 231–236. doi: <https://doi.org/10.1016/j.elspec.2014.04.013>.
- [131] L. Poletto, P. Villoresi, F. Frassetto, *et al.* “Time-Delay Compensated Monochromator for the Spectral Selection of Extreme-Ultraviolet High-Order Laser Harmonics.” In: *Review of Scientific Instruments* 80.12 (2009), p. 123109. doi: 10.1063/1.3273964.
- [132] M. Hatayama, S. Ichimaru, T. Ohcni, *et al.* “Wide-Range Narrowband Multilayer Mirror for Selecting a Single-Order Harmonic in the Photon Energy Range of 40–70 eV.” In: *Optics Express* 24.13 (2016), pp. 14546–14551. doi: 10.1364/OE.24.014546.
- [133] G. Hilber, A. Lago, and R. Wallenstein. “Broadly Tunable Vacuum-Ultraviolet/Extreme-Ultraviolet Radiation Generated by Resonant Third-Order Frequency Conversion in Krypton.” In: *JOSA B* 4.11 (1987), pp. 1753–1764. doi: 10.1364/JOSAB.4.001753.
- [134] C. Dorman, I. Kucukkara, and J. P. Marangos. “Measurement of High Conversion Efficiency to 123.6-Nm Radiation in a Four-Wave-Mixing Scheme Enhanced by Electromagnetically Induced Transparency.” In: *Physical Review A* 61.1 (1999), p. 013802. doi: 10.1103/PhysRevA.61.013802.
- [135] W. Cao, E. R. Warrick, A. Fidler, S. R. Leone, and D. M. Neumark. “Near-Resonant Four-Wave Mixing of Attosecond Extreme-Ultraviolet Pulses with near-Infrared Pulses in Neon: Detection of Electronic Coherences.” In: *Physical Review A* 94.2 (2016), p. 021802. doi: 10.1103/PhysRevA.94.021802.
- [136] W. Cao, E. R. Warrick, A. Fidler, D. M. Neumark, and S. R. Leone. “Noncollinear Wave Mixing of Attosecond XUV and Few-Cycle Optical Laser Pulses in Gas-Phase Atoms: Toward Multidimensional Spectroscopy Involving XUV Excitations.” In: *Physical Review A* 94.5 (2016), p. 053846. doi: 10.1103/PhysRevA.94.053846.

Bibliography

- [137] T. Ding, C. Ott, A. Kaldun, *et al.* “Time-Resolved Four-Wave-Mixing Spectroscopy for Inner-Valence Transitions.” In: *Optics Letters* 41.4 (2016), pp. 709–712. DOI: 10.1364/OL.41.000709.
- [138] N. Harkema, J. E. Bækholm, K. J. Schafer, *et al.* “Attosecond Transient Absorption and Four-Wave Mixing with Tunable IR Pulses.” In: *2018 Conference on Lasers and Electro-Optics (CLEO)*. 2018 Conference on Lasers and Electro-Optics (CLEO). 2018, pp. 1–2.
- [139] A. P. Fidler, S. J. Camp, E. R. Warrick, *et al.* “Nonlinear XUV Signal Generation Probed by Transient Grating Spectroscopy with Attosecond Pulses.” In: *Nature Communications* 10.1 (2019), p. 1384. DOI: 10.1038/s41467-019-09317-4.
- [140] A. Bideau-Mehu, Y. Guern, R. Abjean, and A. Johannin-Gilles. “Measurement of Refractive Indices of Neon, Argon, Krypton and Xenon in the 253.7–140.4 Nm Wavelength Range. Dispersion Relations and Estimated Oscillator Strengths of the Resonance Lines.” In: *Journal of Quantitative Spectroscopy and Radiative Transfer* 25.5 (1981), pp. 395–402. DOI: 10.1016/0022-4073(81)90057-1.
- [141] E. B. Saloman. “Energy Levels and Observed Spectral Lines of Krypton, Kr I through Kr XXXVI.” In: *Journal of Physical and Chemical Reference Data* 36.1 (2007), pp. 215–386. DOI: 10.1063/1.2227036.
- [142] B. Schütte, L. Drescher, T. Witting, M. J. J. Vrakking, and O. Kornilov. “Time-Resolved Extreme-Ultraviolet Refraction.” In preparation.
- [143] R. Miles and S. Harris. “Optical Third-Harmonic Generation in Alkali Metal Vapors.” In: *IEEE Journal of Quantum Electronics* 9 (1973), pp. 470–484. DOI: 10.1109/JQE.1973.1077492.
- [144] A. Kramida, Yu. Ralchenko, J. Reader, and NIST ASD Team. In: (2019).
- [145] S. Klarsfeld. “A Modified Bates-Damgaard Method.” In: *Journal of Physics B: Atomic, Molecular and Optical Physics* 21.24 (1988), pp. L717–L721. DOI: 10.1088/0953-4075/21/24/002.
- [146] H. Muller. “An Efficient Propagation Scheme for the Time-Dependent Schrodinger Equation in the Velocity Gauge.” In: *Laser Physics* 9.1 (1999), pp. 138–148.
- [147] H.-h. Chu and J. Wang. “Efficient Extreme-UV-to-Extreme-UV Conversion by Four-Wave Mixing with Intense near-IR Pulses in Highly Charged Ion Plasmas.” In: *Physical Review A* 97.5 (2018), p. 053840. DOI: 10.1103/PhysRevA.97.053840.

- [148] J. J. Rørstad, N. S. W. Ravn, L. Yue, and L. B. Madsen. “Attosecond Transient-Absorption Spectroscopy of Polar Molecules.” In: *Physical Review A* 98.5 (2018), p. 053401. DOI: 10.1103/PhysRevA.98.053401.
- [149] Griffiths. *Introduction to Quantum Mechanics*. Prentice Hall, 1995. 173 pp.
- [150] G. Dattoli, C. Chiccoli, S. Lorenzutta, *et al.* “Fourier Expansions and Multivariable Bessel Functions Concerning Radiation Problems.” In: *Radiation Physics and Chemistry* 47.2 (1996), pp. 183–189. DOI: 10.1016/0969-806X(95)00036-W.
- [151] M. Kitzler, N. Milosevic, A. Scrinzi, F. Krausz, and T. Brabec. “Quantum Theory of Attosecond XUV Pulse Measurement by Laser Dressed Photoionization.” In: *Physical Review Letters* 88.17 (2002), p. 173904. DOI: 10.1103/PhysRevLett.88.173904.
- [152] O. Ghafur, A. Rouzée, A. Gijsbertsen, *et al.* “Impulsive Orientation and Alignment of Quantum-State-Selected NO Molecules.” In: *Nature Physics* 5.4 (2009), pp. 289–293. DOI: 10.1038/nphys1225.
- [153] A. S. Chatterley, C. Schouder, L. Christiansen, *et al.* “Long-Lasting Field-Free Alignment of Large Molecules inside Helium Nanodroplets.” In: *Nature Communications* 10.1 (2019), p. 133. DOI: 10.1038/s41467-018-07995-0.
- [154] A. A. Milner, J. A. M. Fordyce, I. MacPhail-Bartley, *et al.* “Controlled Enantioselective Orientation of Chiral Molecules with an Optical Centrifuge.” In: *Physical Review Letters* 122.22 (2019), p. 223201. DOI: 10.1103/PhysRevLett.122.223201.
- [155] Geneaux, Romain, Marroux Hugo J. B., Guggenmos Alexander, Neumark Daniel M., and Leone Stephen R. “Transient Absorption Spectroscopy Using High Harmonic Generation: A Review of Ultrafast X-Ray Dynamics in Molecules and Solids.” In: *Philosophical Transactions of the Royal Society A: Mathematical, Physical and Engineering Sciences* 377.2145 (2019), p. 20170463. DOI: 10.1098/rsta.2017.0463.
- [156] S. Beaulieu, A. Comby, D. Descamps, *et al.* “Photoexcitation Circular Dichroism in Chiral Molecules.” In: *Nature Physics* 14.5 (2018), p. 484. DOI: 10.1038/s41567-017-0038-z.
- [157] M. F. Kling, C. Siedschlag, A. J. Verhoef, *et al.* “Control of Electron Localization in Molecular Dissociation.” In: *Science* 312.5771 (2006), pp. 246–248. DOI: 10.1126/science.1126259.

Bibliography

- [158] F. Martín, J. Fernández, T. Havermeier, *et al.* “Single Photon-Induced Symmetry Breaking of H₂ Dissociation.” In: *Science* 315.5812 (2007), pp. 629–633. doi: 10.1126/science.1136598.

Acknowledgments

The work presented in this thesis would not have been possible without the help and support of several persons, to whom I would like to express my thanks and gratitude here.

To Marc Vrakking for supervising and supporting my PhD at the Max-Born-Institute.

Also to Thomas Pfeifer for agreeing to co-refereeing my PhD thesis.

My special thanks I would like to express to Oleg Kornilov for guidance, advice and support in scientific questions and others during my time at MBI. Thanks also to Tobias Witting for his expertise in few-cycle pulse generation and HHG, as well as good times when working in the lab. Thanks to Jochen Mikosch for supervision and support in article writing.

Many thanks also to Bernd Schütte for what I can only describe as a very fruitful collaboration.

I would like to thank Serguei Patchkovskii for his quantum chemical input, especially on attosecond transient absorption spectroscopy of CH₃I.

For help in the lab and experiments I would like to thank a few people, first and foremost Martin Galbraith for the highly appreciated work he has done on the attosecond beamline before me and for showing me the ropes. Also thanks to Geert Reitsma for helping and spending a few elongated evenings in the lab. Special thanks to Ahmet Akin Ünal for keeping the laser running and Roman Peslin for technical support.

Thanks to all the staff at MBI for supporting my work. Thanks to C.-P. Schulz for an offhand mention of mixing-angles that really helped me tying together the analytical work. Thanks to many current and former PhDs at MBI for good times at work and outside of it, including Martin, Felix B., Katrin, Nicola, Johan, Peter, Jenja, Janina, Thomas, Mikhail, Felix S. and Ulrich.

Lastly, my biggest thanks to my friends and family for their loving support in the last years. I could not have done it without you.

Selbstständigkeitserklärung

Hiermit erkläre ich, dass ich die vorliegende Dissertation selbständig und nur unter Verwendung der angegebenen Literatur und Hilfsmittel verfasst habe. Diese Arbeit ist weder in einem früheren Promotionsverfahren angenommen noch als ungenügend beurteilt worden.

Lorenz Drescher

Berlin, den 12. November 2019